Design, fabrication and characterisation of a 20 GHz low phase noise oscillator

Research Report
ISSN 0929-8533

Eindhoven
University of Technology
Netherlands

Faculty of Electrical Engineering

Design, Fabrication and Characterisation of a 20 GHz Low Phase Noise Oscillator

By
J.M.C.P. van Meer
W. De Readt
L.M.F. Kaufmann

EUT Report 98-E-310
ISBN 90-6144-310-5
December 1998

Eindhoven University of Technology Research Report

EINDHOVEN UNIVERSITY OF TECHNOLOGY

Faculty of Electrical Engineering
Eindhoven, The Netherlands

ISSN 0929-8533

Design, fabrication and characterisation of a 20 GHz low phase noise oscillator

by

J.M.C.P. van Meer
W. De Raedt
L.M.F. Kaufmann

EUT Report 98-E-310
ISBN 90-6144-310-5

Eindhoven
December 1998

CIP-DATA LIBRARY TECHNISCHE UNIVERSITEIT EINDHOVEN

Meer, J.M.C.P. van

Design, fabrication and characterisation of a 20 GHz low phase noise oscillator / by J.M.C.P. van Meer, W. De Raedt and L.M.F. Kaufmann. – Eindhoven : Eindhoven University of Technology, 1998.
Eindhoven University of Technology research reports ; 98-E-310. – ISBN 90-6144-310-5
NUGI 832
Trefw.: halfgeleiders ; ruis / faseruis / 1/f ruis / analoge geïntegreerde schakelingen.
Subject headings: high electron mobility transistors / phase noise / III-V semiconductors / monolithic integrated circuits.

Design, fabrication and characterisation of a 20 GHz low phase noise oscillator

Abstract

The design, fabrication and characterisation of a 20 GHz low phase noise oscillator was the subject of a Master Thesis carried out at the Interuniversity Micro-Electronics Center (IMEC), Leuven. A measurement-based, bias-dependent, low-frequency noise model is implemented in the non-linear HEMT model, which is related to IMEC's in-house technology. The noise model and the non-linear model have been implemented in the simulator section of HP Microwave Design System. In order to verify the applicability of this noise model for the design of low phase noise Monolithic Microwave Integrated Circuits (MMICs), a 20 GHz oscillator has been designed. In order to verify every single component of the total design afterwards, the layout of the ultimate oscillator circuit as well as its sub-circuits have been accomplished. From these layouts, the optical masks have been fabricated which are mandatory for the start of the oscillator processing. The phase noise spectrum of the realised basic oscillator has been measured and compared to the simulated noise spectrum. Comparing these phase noise spectra yields a measured phase noise value of –77.1 dBc/Hz versus a simulated noise value of –83.6 dBc/Hz at f = 100 kHz from the carrier. The acquired results on phase noise performance demonstrate the correct modelling and implementation of the low-frequency phase noise model. Using this model one is able to predict the phase noise behaviour of any non-linear circuit fabricated in the technology applied.

Keywords:

Meer, J.M.C.P. van* and W. De Raedt*, L.M.F. Kaufmann
Design, fabrication and characterisation of a 20 GHz low phase noise oscillator.
Eindhoven: Faculty of Electrical Engineering, Eindhoven University of Technology, 1998.
EUT Report 98-E-310

Addresses of the authors:

Faculty of Electrical Engineering
Telecommunication Technology and
Electromagnetism Electronic Devices Group
Eindhoven University of Technology
P.O. Box 513
5600 MB Eindhoven, The Netherlands

E-mail: J.M.C.P. van Meer@imec.be

* IMEC
Kapeldreef 75
B-3001 Leuven
Belgium

Samenvatting

Toekomstige mobiele telecommunicatie systemen vereisen receivers en transmitters die kunnen functioneren op micro-golf of zelfs op millimeter-golf frequenties. Dergelijke systemen kunnen worden gerealiseerd door gebruik te maken van bijvoorbeeld III-V halfgeleiders zoals GaAs en InP. Snelle transistoren zoals de High Electron Mobility Transistor (HEMT) kunnen worden gefabriceerd op een dergelijk substraat en geïntegreerd met passieve componenten, resulterend in een Monolithic Microwave Integrated Circuit (MMIC).

De laag-frequente ruis in deze HEMTs vormt echter een belangrijke beperking voor de toepassing van deze actieve devices in niet-lineaire circuits zoals mixers en oscillatoren. De laag-frequente ruis in de HEMT wordt gemoduleerd door het 'informatie bevattende' hoog-frequente signaal. Dit resulteert in ongewenste amplitude en frequentie modulatie of fase-ruis.

Dit afstudeerwerk beschrijft de modellering van de laag-frequente ruis in InP gebaseerde HEMTs, die gefabriceerd zijn in de MMIC technology van IMEC. Deze ruis-modellering maakt het ontwerpen van niet-lineaire circuits mogelijk waarbij een hoge signaal-ruis verhouding vereist is, zoals bijvoorbeeld in receivers en transmitters. Een op metingen gebaseerd, spanningsafhankelijk, laag-frequent ruis-model is geïmplementeerd in het reeds aanwezige niet-lineaire model dat is gerelateerd aan de 'in-house' InP gebaseerde HEMT technologie. Het ruis-model en het niet-lineaire model zijn beide geïmplementeerd in de simulator sectie van HP Microwave Design System.

Vervolgens, om de toepasbaarheid van dit ruis-model te verifiëren, is een 20 GHz MMIC oscillator ontworpen. Bij elke stap in het ontwerp is voortdurend rekening gehouden met het niveau van de fase-ruis om zo tot een ontwerp te komen met een minimaal ruis niveau. Behalve de layout van het uiteindelijke oscillator circuit, zijn ook de afzonderlijke sub-circuits op de zogenaamde 'masker-layout' geplaatst om op die manier het karakteriseren van elk onderdeel van het volledige circuit achteraf mogelijk te maken. Deze masker-layout vormt het start-punt voor de fabrikatie van de optische maskers welke vereist zijn voor de fabrikatie van de oscillator.

Het fase-ruis spectrum van de gerealiseerde elementaire oscillator is gemeten en vergeleken met het ruis spectrum verkregen uit de simulaties. Dit leverde een gemeten fase-ruis niveau op van –77.1 dBc/Hz versus een gesimuleerd fase-ruis niveau van –83.6 dBc/Hz op een frequentie van $f = 100$ kHz van de carrier.

De bereikte resultaten tonen aan dat de modellering en implementatie van het laag-frequente ruis-model correct is uitgevoerd. Door gebruik te maken van dit model is men in staat om het fase-ruis gedrag van elk niet-lineair circuit te voorspellen, dat gefabriceerd is in de MMIC technologie van IMEC.

Acknowledgements

The success of this research work I owe to the co-operation and interaction of many persons.

First of all, I would like to thank Professor L.M.F. Kaufmann for creating the possibility to perform my graduation project at the Interuniversity Micro-Electronics Center (IMEC) on behalf of the Department of Electrical Engineering at the Eindhoven University of Technology. I wish to acknowledge the financial support of the EC-ERASMUS student exchange programme.

Moreover, I would like to thank Professor M. Van Rossum of IMEC for accepting me in his group, Compound Semiconductor Processing (CSP). I especially would like to thank W. De Raedt for coaching me during the time of my graduation project. His guidance and insight has helped me several times. Further, I am very grateful to K. van der Zanden and Dr. D. Schreurs for their help and support in respect of the InP HEMT based MMIC processing and modelling. I would also like to thank Dr. Simoen for his knowledge and his external contacts concerning low-frequency noise measurements. I also would like to express my appreciation to J. Feyaerts and S. Peeters for their indispensable technical support.

I thank ESAT/TELEMIC and in particular W. Philibert and S. Vandenberghe for their support on design and characterisation of the microwave oscillator.

I am sincerely grateful to Dr. M. Valenza and Professor D. Rigaud of the 'Centre d'Electronique et de Microoptoelectronique de Montpellier' for giving me the opportunity to perform my low-frequency noise measurements. Finally, I would also like to thank W. Poppelreuter of the 'Institut für Mobil- und Satellitenfunktechnik' (IMST) for enabling me to measure the output power and phase noise spectra of the realised oscillator.

Hans van Meer
September 1997

Contents

List of Symbols

Symbol	unit	description
a_i	V	incident travelling voltage wave at port *i*
b_i	V	scattered travelling voltage wave at port *i*
C_{GS}fF	intrinsic gate-source capacitance	
d	μm	coplanar ground-to-ground spacing
f	Hz	frequency
f_T	Hz	cut-off frequency
f_0	Hz	fundamental frequency
g_m	S	transconductance
g_{DS}	S	conductance
I_{DS}	A	drain source current
I_G	A	gate current
k	J/K	Bolzmann's constant
K	-	inverse Linville stability factor
n_s	$1/\text{cm}^{-2}$	carrier density in the 2-DEG
P_{out}	dBm	output power
q	C	electron charge
Q	-	quality factor
R_D	Ω	drain series resistance
R_S	Ω	source series resistance
S_{ij}	-	scattering parameter at port *i* from port *j*
T	K	absolute temperature
t	s	time
V_{DS}	V	drain-source voltage
V_{GS}	V	gate-source voltage
V_i	V	voltage at port *i*
V_T	V	threshold voltage
W	μm	gate width
Z_{in}	Ω	input impedance
Z_L	Ω	load impedance
Z_0	Ω	characteristic impedance
β	1/m	propagation constant
Γ_L	-	load reflection coefficient
Γ_S	-	source reflection coefficient
$\Gamma_{x(t),y(t)}$	-	correlation between $x(t)$ and $y(t)$
δR_{2D}	Ω	elemental resistance of the 2-DEG
δC_{2D}	fF	elemental capacitance of the 2-DEG
δC_G	fF	elemental dielectric capacitance of the barrier layer
θ	-	phase
μ	$\text{cm}^2/\text{V}\cdot\text{s}$	mobility
τ	s	relaxation time constant
ω	Hz	circular frequency

List of Acronyms

2-DEG	2-Dimensional Electron Gas
CAD	Computer Aided Design
CPW	CoPlanar Waveguide
DC	Direct Current
GaAs	Gallium Arsenide
GR	Generation-Recombination
HEMT	High Electron Mobility Transistor
HF	High Frequency
InP	Indium Phosphide
LM	Lattice Matched
LNA	Low-Noise Amplifier
LO	Local Oscillator
MAG	Maximum Available Gain
MBE	Molecular Beam Epitaxy
MESFET	Metal-Semiconductor Field-Effect Transistor
MIC	Microwave Integrated Circuit
MIM	Metal-Insulator-Metal
MMIC	Monolithic Microwave Integrated Circuit
PECVD	Plasma Enhanced Chemical Vapour Deposition
PHEMT	Pseudomorphic HEMT
SI	Semi-Insulating

Chapter 1

Introduction

1.1 Modern telecommunication systems

During the past several decades, there has been a continuous trend to move to higher frequencies in system applications. Telecommunication systems of tomorrow aim at providing the future user with information at any time and at any place. Wireless mobile communication systems are developed in order to fulfil this need. However, the radio frequency spectrum is a limited resource and there is considerable competition in its use. As the lower frequency bands, i.e. 900 and 1800 MHz, become more and more congested, additional capacity can only be made available at higher frequencies.

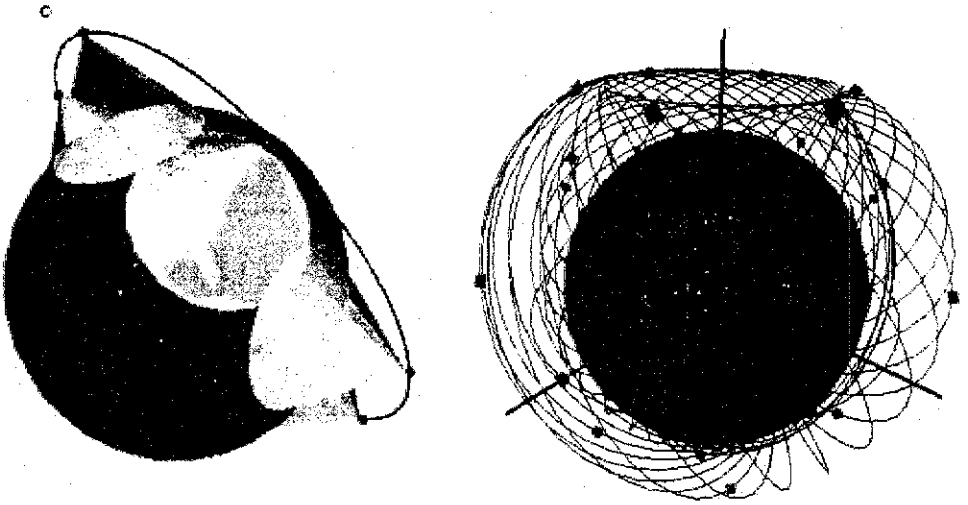

Figure 1.1. Visualisation of a satellite based network as application of a telecommunication system using microwave frequencies.

At these frequencies, the designed analogue circuits applied in such communication systems require a solid-state technology which has far more performance than the silicon-based technologies which are currently mainstream in industry. A material that is very well suitable for the fabrication of high-speed devices is for example the compound semiconductor GaAs or InP. Compared to Si, electrons in these materials have higher low-field mobilities and peak velocities. Using III-V semiconductors, high-speed transistors like the High Electron Mobility Transistor[1] (HEMT) can be fabricated and integrated on the

[1] In literature, the HEMT is referred to by various acronyms, like Modulation Doped FET (MODFET), Heterostructure FET (HFET), Two-dimensional Electron Gas FET (TEGFET) and Selectively Doped Heterostructure Transistor (SDHT).

same semi-insulating substrate with passive components, resulting in a Monolithic Microwave Integrated Circuit (MMIC).

The GaAs and InP based HEMTs have, amongst others, already become the basic components in microwave and millimetre-wave front-ends of high-performance telecommunication systems. In the near future, for example, several HEMT based satellite networks are planned to be operational at an orbit altitude of approximately 700 km using up- and down-link frequencies of 20 to 30 GHz. A visualisation of a satellite based network for mobile units is shown in Figure 1.1.

Modern telecommunication systems have basically a receiver and/or transmitter topology as shown in Figure 1.2.

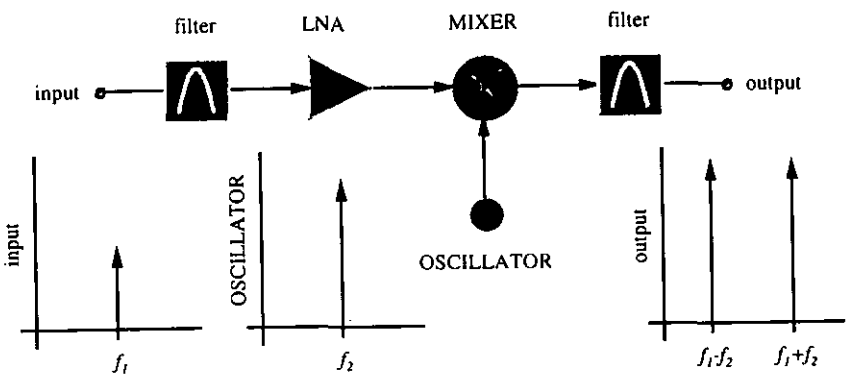

Figure 1.2. Schematic overview of a transceiver.

In case of a receiver, the incoming microwave signal is filtered and amplified by a low-noise amplifier (LNA). Consequently, the signal is down-converted in the frequency domain by a mixer. The second input signal of the mixer is generated by a local oscillator (LO) as illustrated in Figure 1.2. Since the microwave signal is down-converted to the frequency band of interest, the filter connected to the mixer provides transmission to this band indicated in Figure 1.2 by $f_1 - f_2$. Finally, the obtained output signal is directly fed to the data processing unit connected to the receiver.

In case of a transmitter, the second filter shown in Figure 1.2 provides transmission to the frequency band indicated by $f_1 + f_2$.

1.2 Up-converted noise in telecommunication systems

1.2.1 Noise in non-linear circuits

Although the InP based HEMT has proved to be very well suitable for high-frequency and high-performance applications, the low-frequency noise in these HEMTs has shown to be an important limitation of the device performance in non-linear applications such as mixers and oscillators that suffer from noise up-conversion [1]-[3].

In order to obtain an impression of the relative noise level in HEMTs compared to other active devices, the spectral low-frequency noise current power densities of different active devices are shown in Figure 1.3 [4]. From the spectra presented in this Figure, it can be concluded that the HEMT contains a relatively high low-frequency noise level in comparison with the other active devices.

Figure 1.3 indicates that the low-frequency noise behaviour of a HEMT, when up-converted in non-linear circuits, needs to be taken into account in the design of such circuits. Besides, the up-converted noise in HEMTs is proportional to the squared circular frequency ω^2 [5] which will have disadvantageous effects upon the noise performance of non-linear applications operating at microwave frequencies.

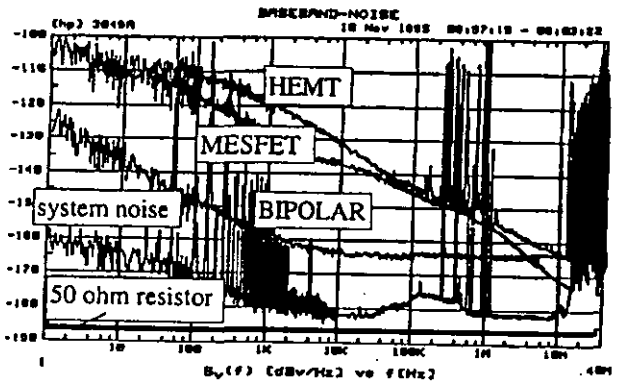

Figure 1.3 Low-frequency noise power spectra of different active devices, like a bipolar transistor, MESFET, GaAs based HEMT [4].

Hence, the output power spectrum of, for example, HEMT based oscillators contains noise originated from the HEMT's low-frequency noise behaviour. Figure 1.4 shows an ideal power spectrum of a microwave oscillator and a spectrum modulated by the low-frequency noise.

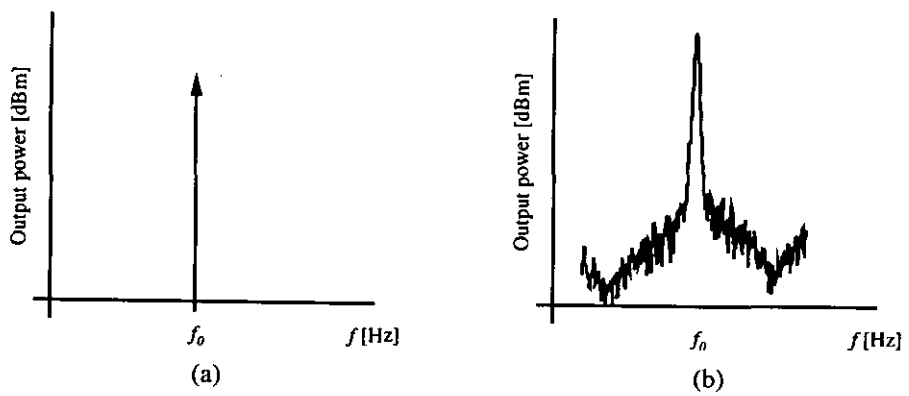

Figure 1.4 (a) Ideal oscillator output power spectrum.
(b) Real oscillator output power spectrum.

The noise can be classified as amplitude modulated (AM) noise and frequency modulated (FM) noise, or phase noise. AM noise causes amplitude variations in the microwave output signal. Phase noise is indicated in Figure 1.4b by the spreading of the frequency spectrum. The oscillator power is not concentrated at a single frequency but is distributed around it. In transistor oscillators AM noise is much lower than phase noise [6].

The spectral distributions on the opposite sides of the carrier are known as noise sidebands. The ratio of the single-sideband (SSB) noise power normalised in a 1 Hz bandwidth to the carrier power is defined as

$$\pounds(f_m) = \frac{\text{noise power in a 1 Hz bandwidth at } f_m \text{ offset from the carrier}}{\text{signal power of the carrier}} = \frac{N}{C} \qquad (1.1)$$

As shown in Figure 1.5a, $\pounds(f_m)$ is the difference in power between the carrier at the resonant frequency f_0 and noise at frequency $f_0 + f_m$. The unit of $\pounds(f_m)$ is dBc/Hz (dBc ≡ "dB below the carrier power").

There are two main sources of phase noise in an oscillator, namely thermal and $1/f$ noise. The thermal noise in the active device has a flat spectrum and is responsible for the $1/f_m^2$ spectral characteristic of the oscillator which is illustrated in Figure 1.5b. $1/f$ Noise is a baseband noise, being up-converted by non-linearities in the active devices to the carrier

frequency. Next, the loop transfer characteristic of the oscillator filters the output voltage, producing a $1/f_m^3$ characteristic [3].

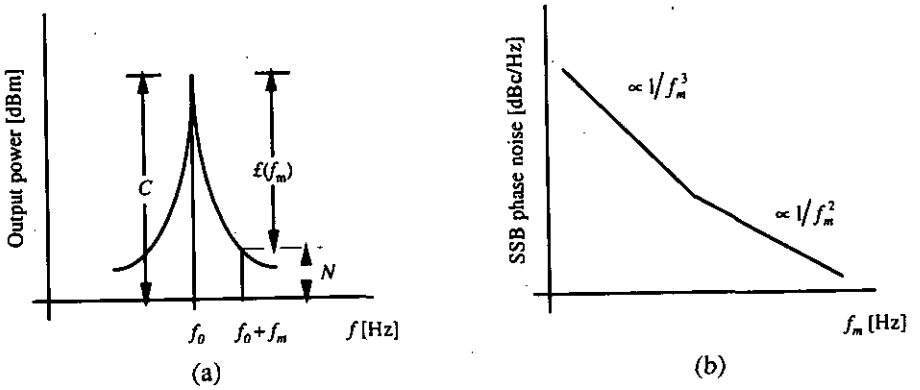

Figure 1.5. (a) Definition of $\pounds(f_m)$ from the oscillator output power spectrum.
(b) Typical phase noise spectrum.

1.2.2 Influence of phase noise

Oscillator phase noise in telecommunication systems degrades both the demodulation and modulation processes. There are three major sources of system performance degradation due to LO phase noise, namely

- Coherence or correlation error. Coherence error applies to coherent demodulation only. Noise in the demodulator phase estimation loop causes a phase error which results in a loss in performance. Coherent demodulation is performed by correlating the received signal with a phase reference derived by the phase estimation loop.
- Signal power loss due to the spreading of the frequency spectrum. The oscillator power is not concentrated at a single frequency but rather, is distributed around it.
- Additive noise effect

The system designer has to consider the effects of local oscillator phase noise when planning a communication system. It is clear that, in order to design a circuit that meets the drawn noise specifications, a low-frequency noise model is primarily needed to enable phase noise simulations and, consequently, also phase noise optimisation.

1.3 Outline of this study

First, the operation properties and the fabrication process of InP based HEMTs as well as the fabrication process of complete MMICs will be discussed in chapter 2. A better understanding of the in-house technology will consequentially yield more insight in the design of MMICs.

Second, the measurement based modelling of low-frequency noise is discussed in chapter 3. The measurement results of low-frequency noise in both the drain and gate current of InP based HEMTs are shown and compared with results reported in literature. Hence, it is shown how a non-linear noiseless HEMT model can be extended by including the bias-dependent low-frequency noise behaviour, which results in a non-linear model that can be used for phase noise simulations.

Consequently, in chapter 4, we will discuss the properties of a microwave oscillator and after that explain and illustrate the design and layout of a complete oscillator. From the presented oscillator layout the optical masks can be fabricated in order to realise the designed circuit. The realised oscillator serves ultimately as verification of the low-frequency noise model which has been implemented in the HP Microwave Design System.

After the realisation of the oscillator circuit has been completed, the obtained measurement and simulation results are compared in chapter 5. Finally, the main conclusions of this research work are also presented in this final chapter.

Chapter 2

IMEC's MMIC pilot line

2.1 Introduction

Since its introduction in 1978 [7] the High Electron Mobility Transistor (HEMT) has made an important contribution to the field of ultra-high-speed microwave electronics [8]. The HEMT has for example proven to have superior properties to the Metal Semiconductor Field Effect Transistor (MESFET). The electron mobility in the conducting channel of the HEMT is enhanced considerably because the electrons in these regions are separated from their parent donors resulting in lower ionised impurity scattering rates. This feature makes the HEMT an excellent active device for low-noise Monolithic Microwave Integrated Circuits (MMICs).

This chapter is intended to briefly introduce the operation and the fabrication process of HEMTs as well as the fabrication process of complete MMICs. At IMEC, this process is continuously under development and therefore it has a pilot function.

2.2 Basic HEMT operation

In the past a variety of HEMT epitaxial structures fabricated on both GaAs and InP substrates have been proposed. A HEMT basically consists of a large-bandgap doped material which is grown epitaxially on a lower-bandgap undoped material. The HEMT

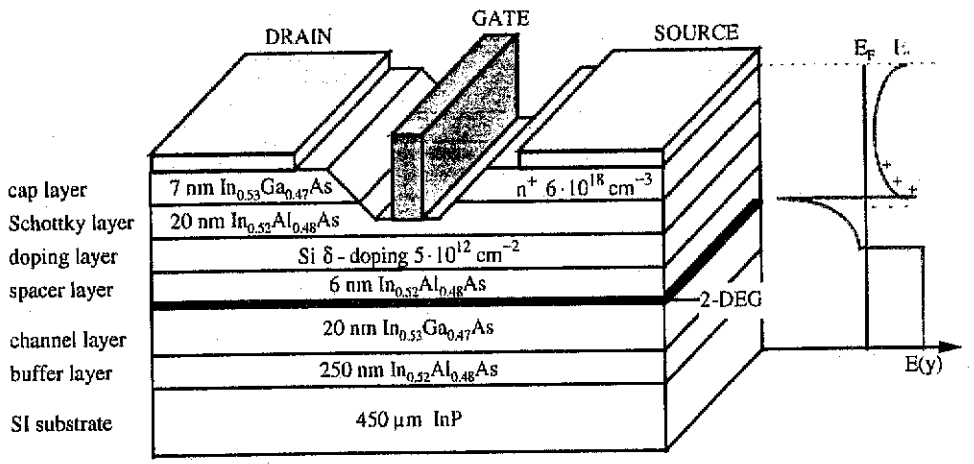

Figure 2.1 Epitaxial layer structure and conduction band diagram illustrating the operating principle of a LM InP HEMT.

structure under study is the lattice-matched (LM) $In_{0.52}Al_{0.48}As/In_{0.53}Ga_{0.47}As$ HEMT grown on an InP substrate. The additional term 'lattice-matched' implies that the grown layers

have the same lattice constant as the InP substrate. If there is a lattice mismatch we speak of 'pseudomorphic' HEMTs or PHEMTs. A cross-section of the studied HEMT is presented in Figure 2.1.

At the interface between the large-bandgap material and the lower-bandgap material, i.e. between the spacer and channel layer, a potential well is formed. The carriers, provided by the large-bandgap doped material, flow into the well where they are captured. In this way, a separation is created between the carriers and the impurities. The number of carriers can be increased by adding a Si δ-doping layer. The carriers are separated from the donor layers by the intermediate undoped spacer layer. This separation results in a significant increase in carrier mobility. The carriers flow to the narrow potential well and form a two-dimensional electron gas (2-DEG) in the plane of the heterojunction.

The cap layer on top of the structure reduces the contact resistance of the alloyed ohmic metal and the series resistance of the access regions between gate and source and gate and drain. Further, it prevents the oxidation of the underlying Al containing Schottky layer.

The 250 nm buffer layer is grown on the semi-insulating (SI) substrate both to smoothen the surface and to improve the electron confinement preventing carrier injection in the buffer or substrate by forming a second barrier underneath the channel.

2.3 HEMT characteristics

The measured drain current I_{DS}-V_{GS}, transconductance g_m-V_{GS} and drain current I_{DS}-V_{DS} characteristics of an InP based HEMT featuring a gate length and width of 0.2 respectively 50 µm, are shown in figure 2.2.

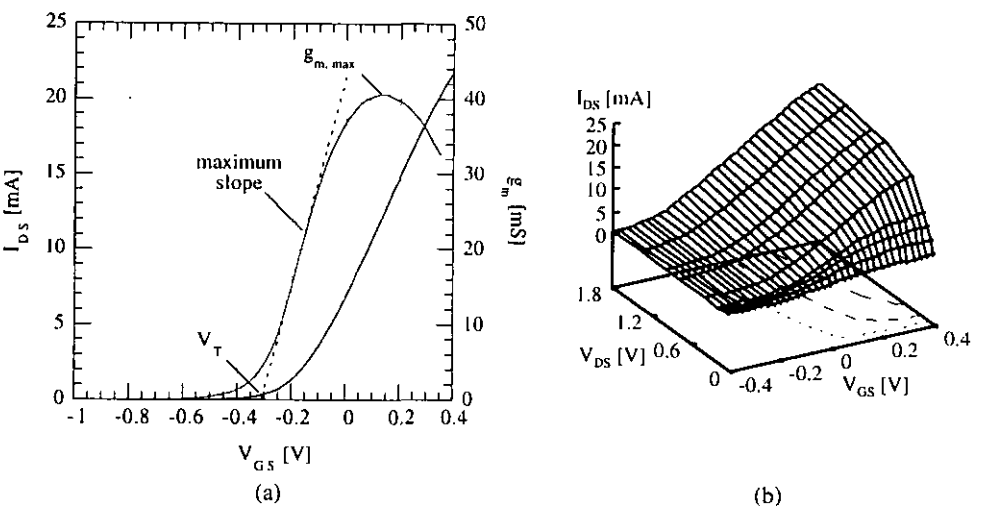

Figure 2.2 Measured DC characteristics of a LM InP HEMT featuring a gate length and width of 0.2 respectively 50 µm: (a) I_{DS}-V_{GS} and g_m-V_{GS} characteristics (V_{DS} = 1.0 V); (b) I_{DS}-(V_{GS}, V_{DS}) characteristics.

From a measured I_{DS}-V_{GS} characteristic the threshold voltage V_T can be extracted. This voltage is determined as the V_{GS} for which the linear extrapolation of the g_m-V_{GS} characteristic at the point of the maximum slope reaches zero. For the InP LM HEMT shown in figure 2.2a, the threshold voltage is -0.32 V and the maximum transconductance of 40.5 mS is reached at a gate voltage of 0.15 V and a current of 12.8 mA.

A summary of typical DC and HF characteristic values of both a GaAs PHEMT and an InP LM HEMT is presented in Table 2.1.

The cut-off frequency f_T of a transistor is defined as the frequency at which the current gain becomes unity if the gate and drain terminals are considered as the current input and output respectively. MAG is the Maximum Available Gain, in this case at f = 10 GHz. The electron density and mobility in the channel at T = 300 K are represented by n_s and µ.

From Table 2.1 it is obvious that InP based HEMTs outperform the conventional GaAs based HEMTs not only in the DC but also in the high-frequency regime.

Table 2.1. Summary of the performance of 0.2 µm GaAs based PHEMTS and InP based LM HEMTs.

	dimension	GaAs	InP
max. DC g_m	mS/mm	650	800
Extrinsic f_T	GHz	110	140
MAG (f = 10 GHz)	dB	17.5	22.5
n_s (T = 300 K)	10^{12} at/cm^2	1.59	2.11
µ (T = 300 K)	cm^2/Vs	5830	10400

2.4 HEMT MMIC process technology

A Monolithic Microwave Integrated Circuit (MMIC) is a microwave circuit in which both active and passive components are fabricated on the same semiconductor substrate. The additional term 'Monolithic' is necessary to distinguish them from the conventional Microwave Integrated Circuit (MIC), which is a hybrid microwave circuit in which a number of discrete active devices and passive components are integrated onto a common substrate using solder or conductive epoxy. An additional advantage of a MMIC is, amongst others, the smaller influence of parasitics since dimensions of a MMIC are generally smaller than of its MIC equivalent.

The passive elements used in MMICs can either be lumped (e.g. spiral inductors) or distributed (e.g. transmission lines). To define both the passive and active components in a MMIC, 7 optical mask levels are required [9]. The complete HEMT fabrication process involves the following processing steps:

- Epilayer growth
- Mesa etching
- Ohmic contact evaporation and alloy
- Interconnection metal evaporation
- NiCr resistors
- E-beam T-gate definition, gate recess etching and metal evaporation
- Nitride passivation
- Top level interconnection metal evaporation and airbridge forming

Epitaxial growth

The initial material for MMIC fabrication is the HEMT epitaxial layer structure which is shown in Figure 2.3. The layer structure is grown using molecular beam epitaxy (MBE), an ultra-high-vacuum technique capable of growing the hyper-abrupt layer profiles needed to successfully fabricate a HEMT. The epitaxial layers are grown on a 2" semi-insulating InP substrate with a thickness of approximately 450 µm and a resistivity of typically 10^7 - 10^8 Ω·cm.

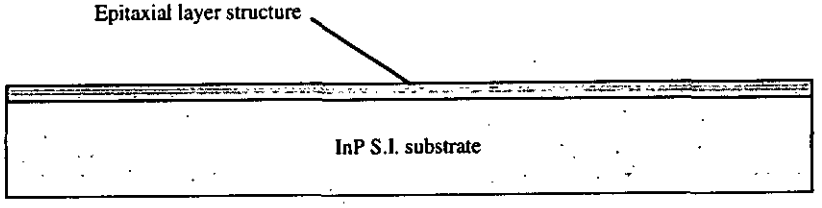

Figure 2.3 MMIC basic material: MBE-grown layer on an InP wafer.

Mesa etching

As a first processing step, the active areas are defined by mesa etching. After optical lithography a phosphoric acid based etchant is used to isolate the different active areas, directly followed by an etch step in a succinic acid based mixture. This selectively etches the $In_{0.52}Al_{0.48}As$ channel material, resulting in a reduction of the sidewall leakage from gate to channel. The active mesas which are left are then used to fabricate the HEMTs and the active layer resistors. Typical sheet resistances for these active layer resistors are 150 Ω/□. The mesa etch step is illustrated in Figure 2.4.

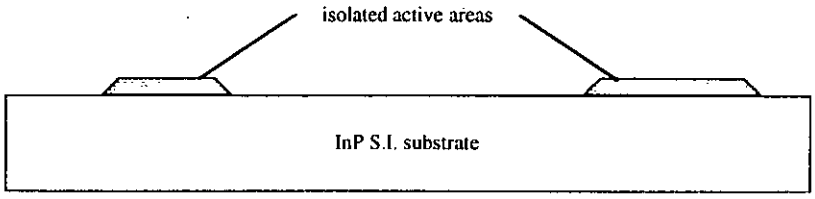

Figure 2.4 Step 1: mesa etch leaving isolated active areas.

Ohmic contact evaporation and alloy

As a second processing step, shown in Figure 2.5, the ohmic regions contacting the HEMT channel are defined, evaporated and alloyed. Ohmic contacts with very smooth morphology and low specific transfer resistance (0.1-0.25 Ω·mm) are obtained by the lift-off of a Ni/Au/Ge/Ni/Au sequence, 2.5/80/40/5/60 nm respectively, followed by an alloy step at 280 °C for 1 min.

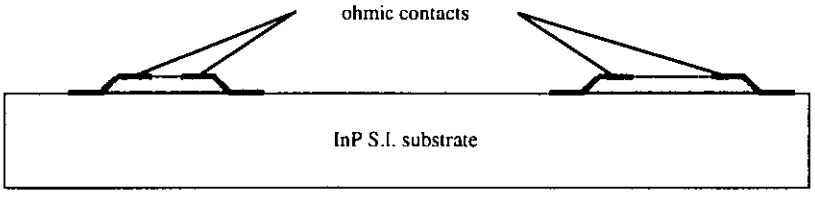

Figure 2.5 Step 2: definition and alloy of the ohmic contacts.

Interconnection metal evaporation

Consequently, to improve the adhesion to the InAlAs buffer layer, a sputtered 10 nm Cr layer, covered by evaporated Au (190 nm), is used as interconnection metal. This first metallisation level which is illustrated in Figure 2.6 also forms the bottom layer of the transmission lines.

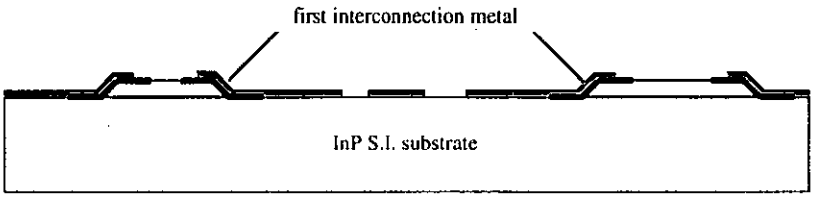

Figure 2.6 Step 3: definition of the first interconnection metal.

NiCr resistors

After the first interconnection level, a resistive NiCr layer is sputtered and lifted off in order to fabricate the thin-film resistors. The thin-film resistor as illustrated in Figure 2.7 is

added as a standard element in MMIC processing because they have a number of advantages in comparison with active layer resistors:

- a 10 times lower sheet resistance can be obtained improving both the accuracy and the size of small resistors (values from 5 to 50 Ω);
- the resistance value can still be tuned after mask fabrication while the resistance value of HEMT layers is dependent on the layer structure and can not be changed independently;
- thin-film resistors have a much lower temperature sensitivity.

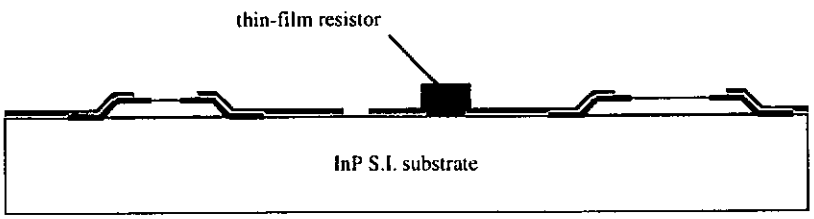

Figure 2.7 Step 4: sputtering and lift-off of the thin-film resistor layer.

E-beam T-gate definition and gate recess etching

T-gates with footprints between 150 nm and 1 μm are written by electron beam lithography with an acceleration voltage of 40 kV in a bilayer resist scheme (PMMA/copolymer). The resist profile after e-beam definition is shown in figure 2.8. The gate is defined using three exposures: one single centre scan with a dose high enough to open the top and the bottom resist layer and two side scans with a lower dose which only open the top resist. After gate metallisation and lift-off this profile results in a T-shaped gate with a footprint between 0.15 and 0.25 μm and a 0.7 μm top.

(a) (b)

Figure 2.8 (a) Two-level resist profile after e-beam definition and development;
(b) Resulting gate metal profile with a footprint of 0.15 μm and a top of 0.7 μm.

After adjusting the threshold voltage V_T by wet recess etching in a phosphoric acid/hydrogen peroxide/water solution, a Pt/Ti/Pt/Au sequence (5/50/50/250 nm) gate metallisation is evaporated and lifted off. The bottom 5 nm Pt is essential to ensure a high Schottky barrier with low leakage on the InAlAs. A picture of the typical T-shaped gate is shown in Figure 2.8b.

Nitride passivation

This step is performed to passivate the active and NiCr areas and to form the dielectric of the parallel-plate MIM capacitor. The different silicon nitride (Si_3N_4) areas are defined by optical lithography and after growth of a 200 nm thick layer by Plasma-Enhanced Chemical Vapour Deposition (PECVD) at 250 °C in 25 min. The residual silicon nitride is etched in a CF_4 plasma. This deposition process is crucial to get reliable and high performance passivated devices and is illustrated in Figure 2.9.

After this step the HEMT fabrication process is completed. However, the MMIC fabrication is not finished until the electroplating which is mandatory for the realisation of airbridges, coplanar transmission lines and the ground plane on the chip.

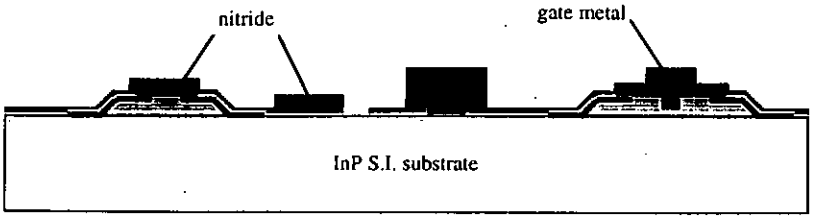

Figure 2.9 Step 5: gate definition and metallisation, nitride deposition and etch.

Top level interconnection metal evaporation and airbridge forming

Because the first metallisation is rather thin, the associated sheet resistance of 0.3 to 0.6 Ω/□ is too high for low-noise MMIC applications. Therefore, the metallisation is complemented with a 1.5 µm thick electrolytic plated gold layer.

By using two different optical mask levels, the VIAS and the METAL level, it is possible to form airbridges, a technological step mandatory in the fabrication of coplanar circuits. The first mask level is used to define the vias between the plating and the first metallisation and to define the top plate of the capacitor. Consequently, an interlayer metal TiW/Au/TiW, with 10/60/10 nm thickness respectively, is evaporated to carry the plating current and to make an electrical contact to the areas which have to be plated. Next, the second lithography step using the METAL level is performed.

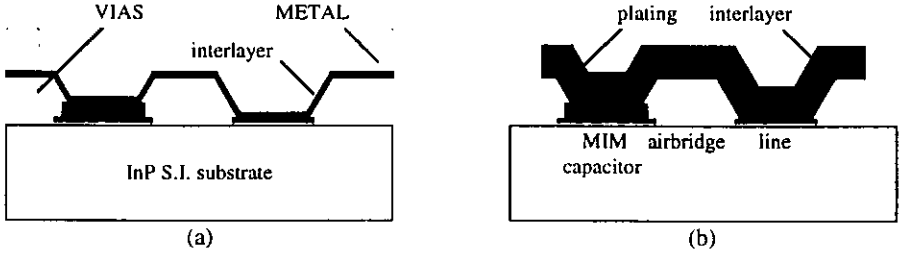

Figure 2.10 Technology for the formation of airbridges: (a) 2-level optical lithography before electrolytic plating; (b) final result of the plating operation.

As shown in Figure 2.10, this results in an airbridge technology: where both the VIAS and METAL level are opened, the interlayer metal is on top of the first metallisation or the capacitor silicon nitride. Where only the METAL level is used, the interlayer metal is on top of the bottom resist and an airbridge is formed after plating and stripping of respectively the top resist, the interlayer metal and the bottom resist. A cross-section after plating is shown in Figure 2.11. A demonstration of the airbridge technology is shown in Figure 2.12.

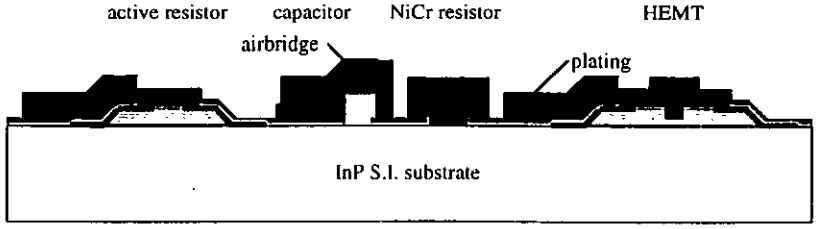

Figure 2.11 Step 6: definition of plating metal.

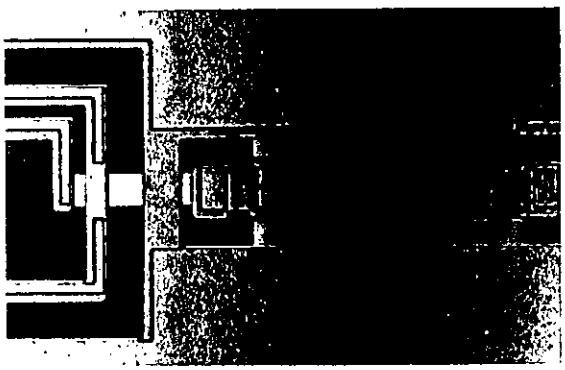

Figure 2.12 Demonstration of the coplanar airbridge technology. The light-coloured gold planes are beneath the darker planes forming the lower part of the bridge.

Library based design

In order to facilitate the design and layout of complete MMICs, a library containing a model and a scaleable layout of a number of commonly used MMIC elements is implemented in the HP Microwave Design System (HP MDS). Corresponding models consist of lumped model equivalents or even of measured scattering parameters put in building-blocks provided by the HP MDS. As a result, the auto-layout facility of the HP MDS enables the designer to generate in a repeatable way the layout of both active and passive components using the 7 mask levels needed in the MMIC process. Elements in this library automatically comply with a number of design rules such as minimal distances and overlaps between different layers. An example of this auto-layout facility is shown in Figure 2.13. From a layout as shown in Figure 2.13b, the digital data needed for the fabrication of the 7 optical mask levels can be generated.

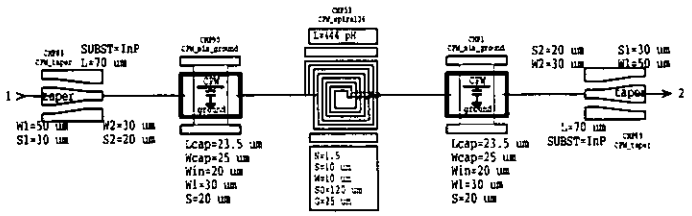

(a)

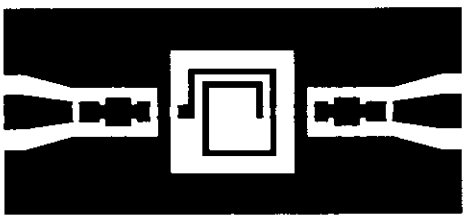

(b)

Figure 2.13 (a) Schematic design entry and (b) resulting automatic layout of a series connection of two MIM-capacitors and a spiral inductor using the library implemented in HP MDS.

2.5 Coplanar circuits

For monolithic circuits operating at millimetre-wave frequencies, coplanar waveguide (CPW) transmission lines are an interesting alternative for the commonly used microstrip lines. As shown in Figure 2.14, the coplanar waveguide consists of three conductors: one signal strip and two ground conductors.

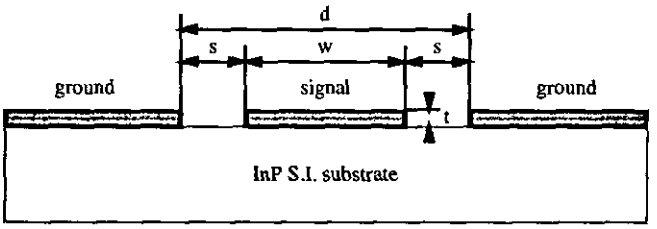

Figure 2.14 Cross section of a coplanar transmission line indicating the different dimensions: the width w, the gap s, the ground-to-ground spacing d and the metallisation thickness t.

The circuit shown in for example Figure 2.12 is realised using the coplanar technology. Typical values of the different dimensions w, s, d and t are respectively 30, 20, 70 and 2.5 μm for a 50 Ω transmission line. The use of coplanar lines in MMICs has several advantages in comparison with the conventional microstrip technology:

- Since both signal and ground conductors are placed at the same side of the wafer, typical processing steps for microstrip circuits, i.e. wafer thinning, via hole etching and backside metallisation, can be avoided which reduces cost, fabrication time and enhances the process yield;
- The ground plane is accessible at the front side of the wafer, allowing an easy parallel and series implementation of active elements. This is especially advantageous at very high frequencies where a higher gain can be obtained due to the absence of a via-hole inductance at the source;
- Coplanar waveguides suffer less from dispersion than microstrip transmission lines, which is important for broad band applications;
- The presence of the ground plane results in a reduced coupling between adjacent lines which enables a further miniaturisation of the MMIC circuits resulting in more compact circuits.

The described technology steps of HEMT and MMIC fabrication form the InP pilot line of IMEC. In combination with additional CAD tools it is possible to design and fabricate circuits which operate at frequencies up to 100 GHz and above.

Chapter 3

Modelling of low-frequency noise in InP based HEMTs

3.1 Introduction

Although the InP based HEMT has shown to be the best performing three terminal devices in terms of noise figures and gain at frequencies up to 100 GHz and above, low-frequency noise has shown to be an important limitation of the device performance in non-linear applications such as mixers and oscillators that suffer from noise up-conversion [1]. This results in an undesired amplitude and frequency modulation. Therefore, for the design of non-linear MMICs, it is of importance to model the HEMT's low-frequency noise behaviour.

In this chapter, the measurement based modelling of low-frequency noise is discussed. After a short introduction of noise in semiconductors and the origin of $1/f$ noise in InP based HEMTs, the measurement results of low-frequency noise in both the drain and gate current are shown and compared with results reported in literature. Consequently, it is shown how a non-linear noiseless HEMT model can be extended by including the bias-dependent noise behaviour acquired from these measurements. This results in a model which can be used for, amongst others, phase noise simulations.

3.2 Noise in semiconductors

Noise in semiconductor devices can be divided into four kinds, i.e. thermal noise, shot noise, generation-recombination noise and $1/f$ or flicker noise. Thermal noise, also called Nyquist or Johnson noise, finds its origin in the Brownian movement of the charge carriers and can be approximated at low frequencies ($f << 10^{12}$ Hz) by a white noise spectral density given by [10]

$$S_v = 4kTR \tag{3.1}$$

where k is Boltzmann's constant, T the temperature and R the resistance of the sample.

Shot noise is generated when charge carriers encounter a potential barrier and cross it independently of each other at random and is given by [10]

$$S_I = 2qI \tag{3.2}$$

where q is the elementary charge and I the current through the sample. The power spectral density of (3.2) is also an approximation and for low frequencies ($f << 10^{11}$ Hz) shot noise is sometimes called white noise.

Generation-recombination noise or g-r noise is caused by the random trapping and de-trapping of carriers; fluctuations of the number of free charge carriers N result in

fluctuations in the conductance. The power spectral density of the fluctuations in N is given by [10]

$$S_N = \frac{4\tau \cdot \langle \Delta N^2 \rangle}{1+\omega^2\tau^2} \tag{3.3}$$

where τ is the relaxation time of the trapping process, $\langle \Delta N^2 \rangle$ the variance of the fluctuations ΔN and ω the circular frequency. Equation (3.3) holds for a two level system, i.e. a conduction or valence band and a trap level.

$1/f$ Noise owes its name to its spectral density that is almost inversely proportional to the frequency over a wide frequency range down to very low frequencies (10^{-6} Hz) [11]. $1/f$ Noise is caused by fluctuations in the conductivity; in semiconductors the conductivity is given by

$$\sigma = q(\mu_n n + \mu_p p) \tag{3.4}$$

where q is the elementary charge, μ_n and μ_p are the mobility of electrons and holes and n and p are the concentration of free electrons and holes, respectively. From (3.4) it is clear that conductivity fluctuations can be caused by fluctuations of the number of free carriers, by fluctuations of the mobility or by their correlated contributions. Although, to this day, there is no generally accepted theory for the $1/f$ noise in semiconductors, two models based on number respectively mobility fluctuations have been proposed that attempt to explain this kind of noise.

The model based on number fluctuations of free carriers is the McWhorter model [12]; this model ascribes the number fluctuations of free carriers to the spontaneous trapping and de-trapping of electrons in interface states or traps located at some distance from the semiconductor interface. The trapping and de-trapping in these traps produce g-r spectra with distributed relaxation times τ. The $1/f$ spectrum is a result of a weighted superposition of these g-r spectra. A demonstration of such a superposition is illustrated in Figure 3.1.

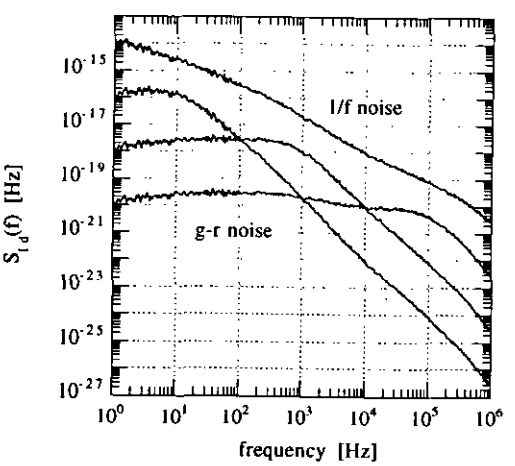

Figure 3.1. $1/f$ Noise spectrum as the result of a weighted superposition of g-r noise spectra.

The other model, the Hooge model, considers carrier scattering at lattice vibrations to be the cause of $1/f$ fluctuations. Hooge presented an empirical relation for the $1/f$ noise in homogeneous samples of semiconductors and metals [13]

$$\frac{S_G(f)}{G^2} = \frac{\alpha_H}{Nf} \tag{3.5}$$

where $S_G(f)$ is the noise power spectral density of the fluctuations in the conductance G, N is the total number of free charge carriers and α_H is a parameter, the Hooge parameter.

3.3 Origin of 1/*f* noise in InP based HEMTs

The low-frequency noise in an InP based HEMT is the result of the presence of various noise sources distributed within the different layers, surfaces and interfaces of the active device. The low-frequency noise can be interpreted in terms of fluctuations of the number of free carriers like is suggested in McWhorter's model [14]. The analysis presented in this paragraph applies for structures biased in the linear regime, with negligible drain and source ohmic contact noise.

If the channel of the HEMT is assumed to be uniform, the conductance G relates to the total number of carriers N in the channel through

$$G = Nq\mu_n / L^2 \tag{3.6}$$

where q and μ_n are the charge and the mobility of the channel electrons, L the drain to source distance and $N = n_s Z \cdot L$, where Z is the channel width and n_s the channel electron density (cm^{-2}). Consequently, the spectral drain current noise density can be written as

$$S_I(f) = \left(q^2\mu_n^2 V_{DS}^2 / L^4\right) \cdot S_N(f) \tag{3.7}$$

where $S_N(f)$ is the noise spectral density of the total number of carriers N. Note that $S_I(f)$ does not include the contributions of the drain and source ohmic contacts and of the gate current. The number fluctuations of free carriers $S_N(f)$ is related to the occupancy spectrum of the traps $S_t(f)$ which are distributed within the layers, surfaces and interfaces which constitute the HEMT structure.

In order to calculate the low-frequency noise spectrum in the InP based HEMT we use equivalent electrical networks which are formed by distributed capacitive and resistive elements. The capacitive elements are associated to elemental dielectric capacitances within the different regions of the structure and to elemental local charge variations in traps or conductive channels; the resistive elements are related to carrier transport and to trap kinetics. The equivalent distributed electrical network of the ideal trap-free HEMT is shown in Figure 3.2a; the channel is divided into slices of length δy which are represented by elemental equivalent electrical circuits. δR_{2D} and δC_{2D} are the elemental resistance and capacitance of the 2-DEG in the channel, δC_G is the elemental dielectric capacitance of the barrier layer.

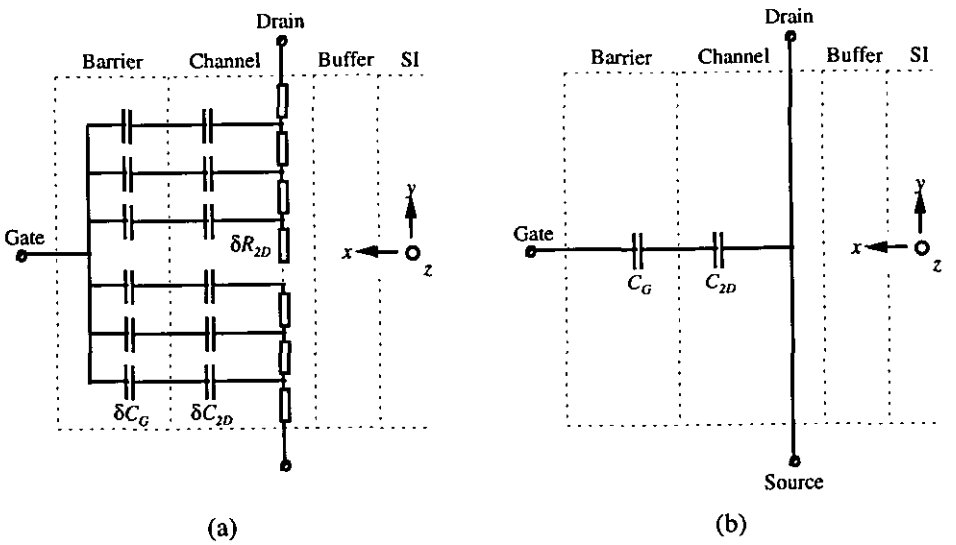

Figure 3.2. (a) Equivalent distributed electrical network of the ideal trap-free HEMT.
(b) Simplified electrical equivalent circuit of the ideal trap-free HEMT.

Since the resistive elements are very small compared to the capacitive elements [14], the equivalent circuit of 3.3a can be considerably simplified. The distributed capacitive elements of the equivalent circuit can then be lumped into single elements, which results in the simplified network of Figure 3.2b.

In order to account for the contribution of traps within the HEMT structure distributed electrical networks are introduced. The equivalent circuit of a real HEMT including the networks of the traps is shown in Figure 3.3a. The distribution of traps is assumed uniform along the (y, z) co-ordinates parallel to the channel plane, while it is considered arbitrary along the x direction perpendicular to the layers and interfaces. The number of traps is divided into different classes which are identified by their location within the various regions of the structure, their charge exchange kinetics and their electronic energy level.

The contribution to the $1/f$ noise of defect levels located within the channel layer is negligible, since they cannot provide the distribution of trapping time constants which is required to account for $1/f$-like noise.

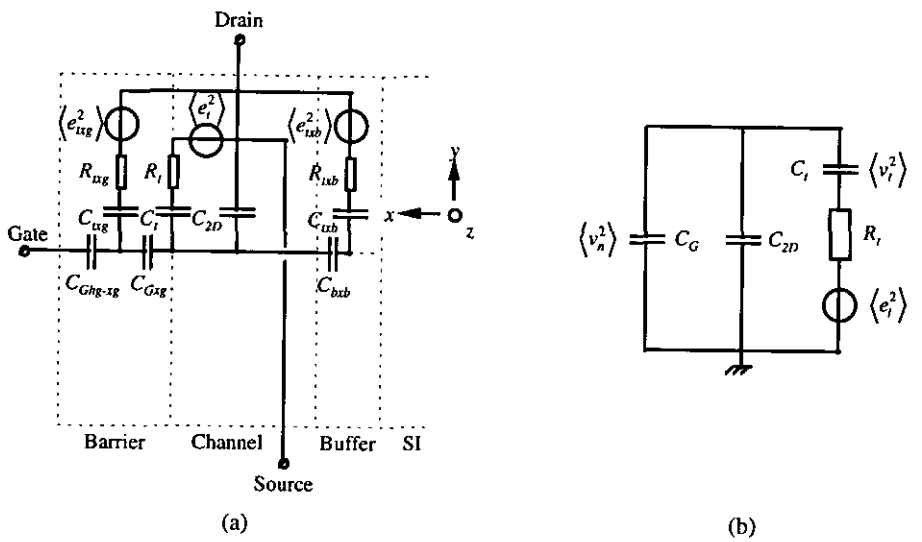

Figure 3.3. (a) Equivalent electrical noise circuit of a real HEMT including the elemental networks the traps.
(b) Simplified equivalent electrical noise circuit of the HEMT for traps located at the barrier/channel interface.

From each noise source shown in Figure 3.3a we can derive its contribution to the channel noise. Here we will derive the contribution of only one source just to demonstrate the basic principle; our example concerns the contribution of the barrier/buffer channel interface. Figure 3.3b shows the simplified equivalent electrical noise circuit of the HEMT with traps at this interface. C_t is the capacitance associated to a class of traps at the interface between the channel layer and the adjacent buffer or barrier layers; R_t accounts for the carrier exchange kinetics between these traps and the channel. The interface trap occupancy fluctuations are accounted for by the equivalent noise voltage source $\langle e_t^2 \rangle$. Since traps and the channel can be considered in equilibrium, the Nyquist formula applies, giving

$$\langle e_t^2 \rangle = 4kTR_t\Delta f \tag{3.8}$$

The noise spectral density of the trap occupancy $S_t(f)$ and that of the channel number of carriers $S_N(f)$ relate to the noise voltage $\langle v_t^2 \rangle$ and $\langle v_n^2 \rangle$ across C_t and $C_{2D} // C_G$ through the relation

$$S_N(f) = \left(\frac{C_t}{q}\right)^2 \cdot \frac{\langle v_t^2 \rangle}{\Delta f} = \left(\frac{C_G + C_{2D}}{q}\right)^2 \cdot \frac{\langle v_n^2 \rangle}{\Delta f} \tag{3.9}$$

From Figure 3.3b the relation between the noise voltage $\langle e_t^2 \rangle$, given by (3.8), and $\langle v_t^2 \rangle$ can be derived resulting in the following transfer function

$$\frac{\langle v_t^2 \rangle}{\langle e_t^2 \rangle} = \frac{1}{\left(1 + \frac{C_t}{C_G + C_{2D}}\right)^2 + (2\pi f R_t C_t)^2} \tag{3.10}$$

Since C_t is small compared to $C_{2D}+C_G$ [14], which corresponds to a density of traps small compared to the number of carriers N in the channel, combining equations (3.8), (3.9) and (3.10) yields

$$S_N(f) = \left(\frac{4kTC_t}{q^2}\right) \cdot \frac{\tau}{1 + (2\pi f \tau)^2} \tag{3.11}$$

where $\tau = R_t C_t$ is the trap time constant; capacitance C_t is function of the trap energy E_t.

The distribution of trapping constants, which is required to account for the $1/f$-like noise spectrum, is assumed to be provided by a distribution of tunnelling probabilities originating from the traps located at the channel-buffer and channel-barrier interfaces. These traps fluctuate independently from each other and are distributed in space and energy range within the HEMT structure. The required range of time constants can be provided by the available distribution of tunnelling probabilities of channel electrons in traps. $S_N(f)$ can be derived by an integration of equation (3.11) in the energy range and in real space along the direction normal to the interface [14], yielding

$$S_N(f) = ZL \cdot \left(\frac{kT}{q}\right) \cdot \left(\frac{C_{2D}}{C_G + C_{2D}}\right)^2 \cdot \left(\frac{N_{it}}{f}\right) \tag{3.12}$$

where N_{it} is the density of the interface traps ($cm^{-2} \cdot eV^{-1}$). Finally combining (3.7) and (3.12) yields the contribution of the barrier/buffer channel interface to the channel noise

$$S_I(f) = \left(qkT\mu_n^2 V_{DS}^2\right) \cdot \left(\frac{Z}{L^3}\right) \cdot \left(\frac{N_{t,eff}}{f}\right) \tag{3.13}$$

where $N_{t,eff}$ is an effective density of traps ($cm^{-2} \cdot eV^{-1}$). Note that (3.13) implies that in the ohmic regime the dependence of the low-frequency noise in the channel is quadratic with V_{DS}; the dependence of V_{GS} is enclosed in equation (3.13) by the mobility μ_n. This dependence can be introduced in equation (3.13) if the relation between μ_n, I_{DS} and V_{GS} is known. From literature [15] it can be stated that

$$I_{DS} \propto \mu_n \cdot (V_{GS} - V_T)^{\alpha} \tag{3.14}$$

where α equals 2 for an approximation of the drain current near threshold. α Equals 1 for an approximation above threshold. Combining equations (3.13) and (3.14) gives an impression of the gate bias dependence on the spectral drain current power density.

Equation (3.13) yields a qualitative impression of the *1/f noise* in InP based HEMTs. It is clear that before (3.13) can be applied, measurements have to be carried out in order to obtain values for the mobility μ_n which is bias dependent and the effective density of traps $N_{t,eff}$.

Analogously to the method described above, we can derive the contributions of the barrier layer, buffer layer and buffer substrate interface to the channel noise, which yields similar equations.

3.4 Low-frequency noise measurements[1]

To obtain an accurate bias dependent noise model that can be used in commercial simulators, noise measurements have been performed on InAlAs/InGaAs InP based HEMTs. In this section we present the results of the low-frequency drain and gate current noise measurements of a representative HEMT with a gate length and width of 0.2 respectively 50 μm. Successively, set-up, measurement results and results reported in literature are discussed. Since these reported results have been acquired from conventional AlGaAs/GaAs HEMTs, we can compare them with our obtained measurement results for verification and to get an impression of the noise level in InP based HEMTs. Finally, in section 3.4.3 the results of coherence measurements between drain and gate noise sources are discussed.

3.4.1 Drain current noise

Set-up

To obtain spectral drain current power densities an EG&G Brookdeal 5003 low-noise voltage amplifier in combination with an HP 89410A Vector Signalling Analyzer has been used. The set-up for the drain current noise measurements with the voltage amplifier is shown in Figure 3.4a. The grey boxes V_{DD} and V_G are symbol for battery voltage supplies with built-in low-pass filters to minimise external influences.

In the measurement set-up the drain current can be extracted by measuring the voltage drop across the series resistor R. Since R is a metal resistor it generates no significant $1/f$ noise. The additional capacitance C between gate and source is needed to keep the HEMT from unwanted oscillations. The output of the voltage amplifier $\langle v_{out}^2 \rangle$ is directly connected to the FFT analyser.

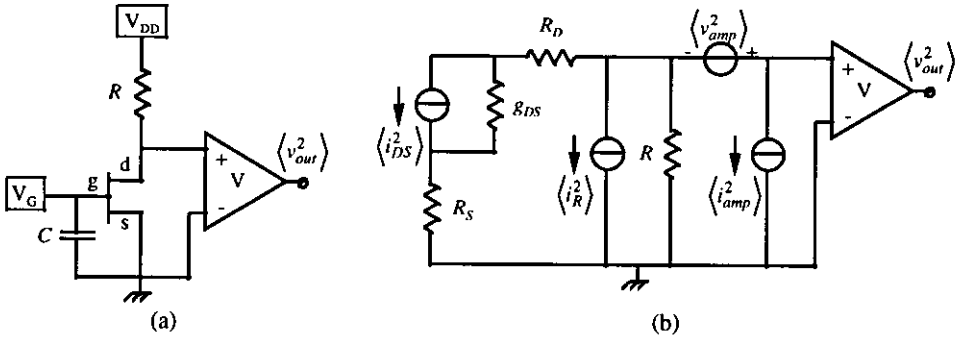

Figure 3.4. (a) Set-up for drain current noise measurements with the voltage amplifier EG&G Brookdeal 5003. The grey boxes V_{DD} and V_G are symbol for voltage supplies with built-in low-pass filters.
(b) Low-frequency noise equivalent circuit of the measurement set-up.

The low-frequency noise equivalent circuit of the measurement set-up is shown in Figure 3.4b. It is obvious that the total noise at the input of the amplifier is a superposition of the influences of

- the voltage and current noise of the amplifier $\langle i_{amp}^2 \rangle$ and $\langle v_{amp}^2 \rangle$;
- the thermal noise of resistor R represented by the Nyquist formula

$$\langle i_R^2 \rangle = \frac{4kT\Delta f}{R} \tag{3.15}$$

[1] The low-frequency noise measurements have been carried out at the 'Centre d'Electronique et de Microoptoelectronique de Montpellier'.

where k is Boltzmann's constant, T the absolute temperature, Δf the bandwidth and R the resistance of the resistor (397 Ω);

- the current noise caused by the HEMT

$$\left\langle i_{DS}^2 \right\rangle = \left\langle \left(g_m \cdot v_{GS} \right)^2 \right\rangle + \left\langle i_N^2 \right\rangle \tag{3.16}$$

where g_m is the transconductance and i_N the intrinsic current noise source of the HEMT.

From DC measurements we extract the intrinsic output conductance g_{DS} to calculate the spectral drain current power density $S_{I_{DS}}$. Since the channel resistance $1/g_{DS}$ and the resistance of R are small compared to the input impedance of the amplifier (5 MΩ), the effect of the amplifier current noise $\left\langle i_{amp}^2 \right\rangle$ on the output voltage noise $\left\langle v_{out}^2 \right\rangle$ is negligible compared to the effect of the voltage noise $\left\langle v_{amp}^2 \right\rangle$. Under this condition the spectral drain current power density $S_{I_{DS}}(f)$ can be calculated from $\left\langle v_{out}^2 \right\rangle$ yielding

$$S_{I_{DS}}(f) = \left(\frac{1 + g_m R_s + \left(R_d + R_s + R \right) \cdot g_{DS}}{R} \right)^2 \cdot \left(\frac{\left\langle v_{out}^2 \right\rangle}{G^2 \Delta f} - \frac{\left\langle v_{amp}^2 \right\rangle}{\Delta f} \right) - \frac{4kT}{R} \tag{3.17}$$

where G is the gain of the voltage amplifier (60 dB). The last term in equation (3.17) represents the thermal noise of the series resistor in the measurement set-up. This thermal noise level is situated at $S_I(f) = 4.1 \cdot 10^{-23}$ A²/Hz and restrains the lower limit at which valid measurements can be performed. The amplifier voltage noise $\left\langle v_{amp}^2 \right\rangle$ is obtained from a noise measurement with the input of the amplifier short-circuited to ground.

Results reported in literature [13]

Here we present reported measurement results that have been obtained for the drain current noise of AlGaAs/GaAs HEMTs, while the HEMT is merely biased in the ohmic regime. In Figure 3.5 the relative $1/f$ noise in the drain current S_I/I^2 at f = 20 Hz of 4 HEMTs is shown versus the effective gate voltage $V_G = V_{GS} - V_T$. The details of these HEMTs are shown in Table 3.1.

Table 3.1 HEMT parameters

Supplier	Fujitsu	NEC	NEC	Sony
Model number	FHX01FA	202-83A	202-83A	2SK878-1
Device code	F3	N3	N20	S6
Gate length [μm]	0.4	0.3	0.3	0.5
Gate width [μm]	250	200	200	200
Source-drain distance [μm]	2.0	1.3	1.3	1.9
Series resistance [Ω]	6	10	9	7

From figure 3.5 we can distinguish three different regions: $S_I/I^2 \propto (V_G)^i$ with i = -1, -3 and 0. From plain calculations with Hooge's relation (3.5) one can calculate that in the first region, where $S_I/I^2 \propto (V_G)^{-1}$, S_I/I^2 is dominated by the channel resistance $1/g_{DS}$ and the current noise in the channel. In the second region the series resistances R_d and R_s and the current noise in the channel dominate, while in the third region the series resistances as well as the current noise in these series resistances dominate, resulting in the dependencies $S_I/I^2 \propto (V_G)^{-3}$ respectively $S_I/I^2 \propto (V_G)^0$.

Measurement results

With the described set-up noise measurements have been carried out in the ohmic as well as in the saturation regime for various values of V_{GS}. As shown in Figure 3.6a for one

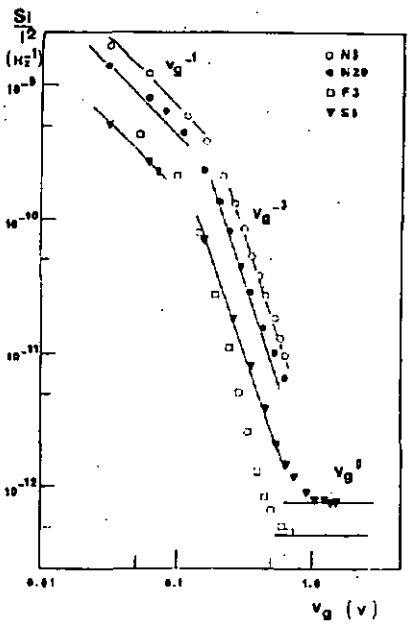

Figure 3.5. The relative $1/f$ noise in the drain current $S_{I_{DS}}/I_{DS}^2$ at $f = 20$ Hz versus the effective gate voltage $V_G = V_{GS} - V_T$ [13]. The HEMT is biased in the ohmic regime with V_{DS} at most equal to 50 mV.

operating-point, all drain current noise measurements produced merely $1/f$-like spectra in the accessible frequency range. The thermal noise will start to dominate beyond this frequency, which follows from the theoretical value of $S_{I_{DS}}(f) \approx 3.3 \cdot 10^{-22}$ A^2/Hz for the case of Figure 3.6a. An overview of the noise measurements is given in Figure 3.6b which shows the $1/f$ noise in the drain current $S_I(f)$ at $f = 1$ Hz versus V_{GS} and V_{DS}.

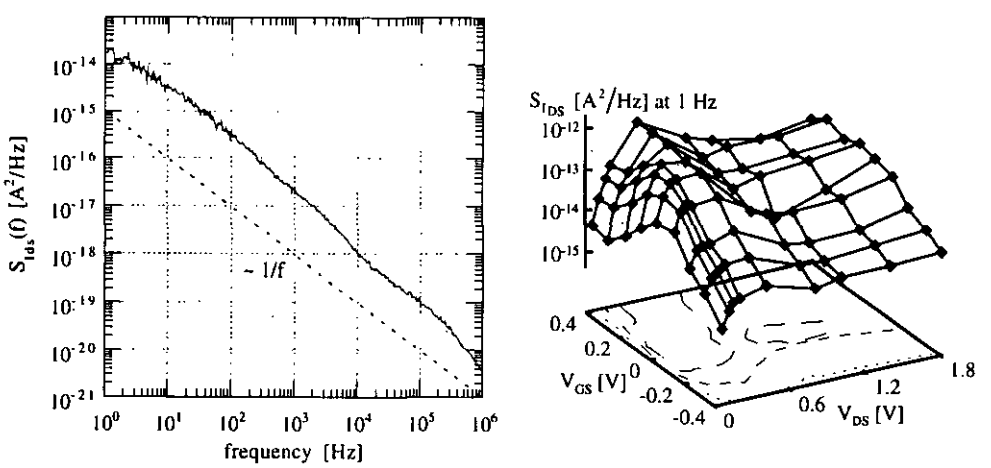

(a) (b)

Figure 3.6. (a) Spectral drain current power density of the 0.2 µm, 50 µm InP LM HEMT used for the low-frequency drain current noise measurements. $V_{DS} = 50$ mV and $I_{DS} = 1$ mA.
(b) $1/f$ Noise in the drain current $S_I(f)$ at $f = 1$ Hz versus V_{GS} and V_{DS}.

The $1/f$ noise in the drain current, depicted in Figure 3.6b, shows a quadratic behaviour for low drain bias, i.e. in the ohmic regime, which is in agreement with the derived $1/f$ noise relation represented by equation (3.13). To compare the measurements with the reported

results, the relative $1/f$ noise in the drain current S_I/I^2 at $f = 20$ Hz is presented in Figure 3.7. The measurement results have been scaled to a HEMT with a gate width of 200 µm by using Hooge's relation (3.5).

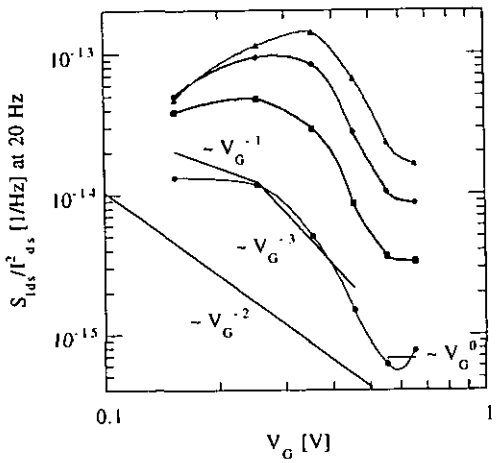

Figure 3.7. Relative $1/f$ noise in the drain current S_I/I^2 at $f = 20$ Hz versus the effective gate voltage $V_G = V_{GS} - V_T$. $V_{DS} = 50$, 100, 150 and 200 mV. The measurement results have been scaled down to a HEMT with a gate width of 200 µm.

From Figure 3.7 it is clear that only the noise characteristic with $V_{DS} = 50$ mV has a similar shape as predicted by Figure 3.5. This can be attributed to the fact that the other measurements have been performed at $V_{DS} = 100$ mV or above, i.e. outside the pure ohmic region and therefore they can not be used for a valid comparison.

For the characteristic with $V_{DS} = 50$ mV it can be concluded that the relative $1/f$ noise in the drain current of an InP based HEMT lies about 3 decades lower than in the case of a GaAs based HEMT. Further, the range of the relative $1/f$ noise is in the order of 3 decades in case of the GaAs based HEMT while it is only one decade in case of the InP based equivalent. Note that although in literature [13] the V_G^0 dependence is ascribed to the series resistance, this noise level is not constant for different values of V_{DS} as can be concluded from Figure 3.7.

From the presented McWhorter based analysis in section 3.3, it follows that a lower level of the relative $1/f$ noise in the drain current noise can be explained by less trapping and de-trapping of electrons in the layers around the channel. Consequently, it can be stated that the electron confinement of the InP based HEMT yields better low-frequency noise performance than the GaAs based HEMT. If Hooge's relation (3.5) is considered the lower noise level can be explained due to a smaller Hooge parameter α_H which is also an indication of a better technology.

From the analysis presented in section 3.3 we can apply equations (3.13) and (3.14) in order to compare the measured and predicted gate bias dependence. Combining (3.13) and (3.14) yields

$$\frac{S_I(f)}{I^2} \propto \left(\frac{V_{DS}}{V_{GS} - V_T}\right)^2 \tag{3.18}$$

where $V_{GS} - V_T > 0$. From equation (3.18) it follows that the relative $1/f$ noise is proportional to V_G^{-2}, where $V_G = V_{GS} - V_T$, as illustrated in Figure 3.7. Since the gate bias dependence obtained from the analysis follows the measured dependence only roughly, it is obvious that the analysis of section 3.3 has only limited validity. At this point, it can be concluded that the most accurate noise model can be acquired if the measurement results are implemented directly in a low-frequency noise model.

3.4.2 Gate current noise

Set-up

An EG&G Brookdeal 5002 low-noise current amplifier in combination with an HP 3562A Dynamic Signal Analyzer has been used for the gate current noise measurements. In this way, the spectral gate current power density S_{I_G} is measured directly. The set-up for the measurements with the current amplifier is shown in Figure 3.8a. The gate current can be extracted from the corresponding gate voltage by means of a preceding I-V characterisation.

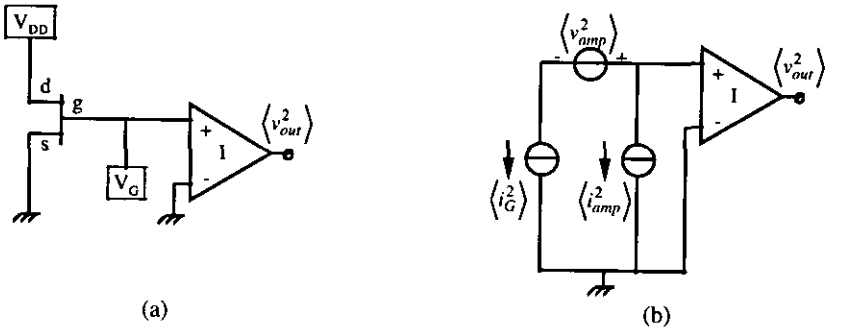

Figure 3.8. (a) Set-up for gate current noise measurements with the current amplifier EG&G Brookdeal 5002. The grey boxes V_{DD} and V_G point to voltage supplies with built-in low-pass filters
(b) Noise equivalent circuit at the input of the voltage amplifier.

The low-frequency noise equivalent circuit of the measurement set-up is shown in Figure 3.8b. Under the stated condition that the effect of the amplifier voltage noise $\langle v_{amp}^2 \rangle$ on the output voltage noise $\langle v_{out}^2 \rangle$ is negligible compared to the effect of the current noise $\langle i_{amp}^2 \rangle$, the spectral gate current power density S_{I_G} can be calculated from $\langle v_{out}^2 \rangle$ resulting in

$$S_{I_G}(f) = A^2 \cdot \frac{\langle v_{out}^2 \rangle}{\Delta f} - \frac{\langle i_{amp}^2 \rangle}{\Delta f} \tag{3.19}$$

where A is the sensitivity of the current amplifier (10^{-7} A/V). The amplifier current noise $\langle i_{amp}^2 \rangle$ is obtained from a noise measurement with the input of the amplifier short-circuited to ground.

Results reported in literature [11]

The measurements of the reported results on the gate current noise have been carried out on conventional AlGaAs/GaAs HEMTs with source and drain in short-circuit. In Figure 3.9 the results of S_{I_G} versus I_G are shown. The details of these HEMTs are summarised in Table 3.2.

Table 3.2 HEMT parameters

Supplier	Fujitsu	IMEC	IMEC
Model number	FHX31FA	2T4	7T4
Device code	A	B	C
Gate length [μm]	0.25	0.3	0.3
Gate width [μm]	280	50	50
Kind of gate recess etch	-*	wet	plasma

* not mentioned in reference [11]

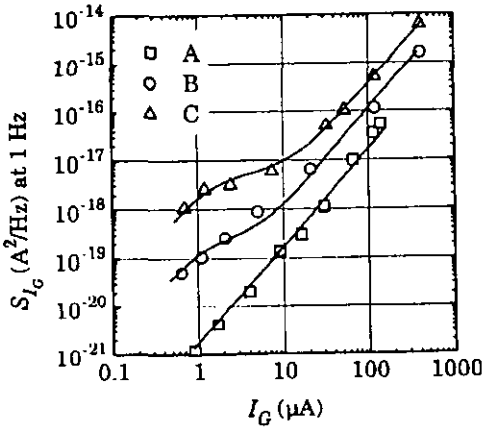

Figure 3.9. Gate current noise S_{I_G} at $f = 1$ Hz versus gate current I_G, $V_{DS} = 0$ V, [11].

At high currents S_{I_G} is proportional to I_G^2. At low currents the HEMTs 2T4 and 7T4 show deviations from the quadratic behaviour which can be attributed to the influence of the ohmic leakage current on the gate current noise.

Measurement results

With the described set-up noise measurements have been performed for various values of V_{DS} and V_{GS}. As shown in Figure 3.10a for one operating point, again, all gate current noise measurements produced merely $1/f$-like spectra in the accessible frequency range. The shot noise will start to dominate beyond this frequency, which follows from the theoretical value of $S_{I_G}(f) = 2qI \approx 1.2 \cdot 10^{-24}$ A²/Hz for the case of Figure 3.10a. An overview of the noise measurements is given in Figure 3.10b which shows the $1/f$ noise in the gate current S_{I_G} at $f = 1$ Hz versus V_{GS} and V_{DS}.

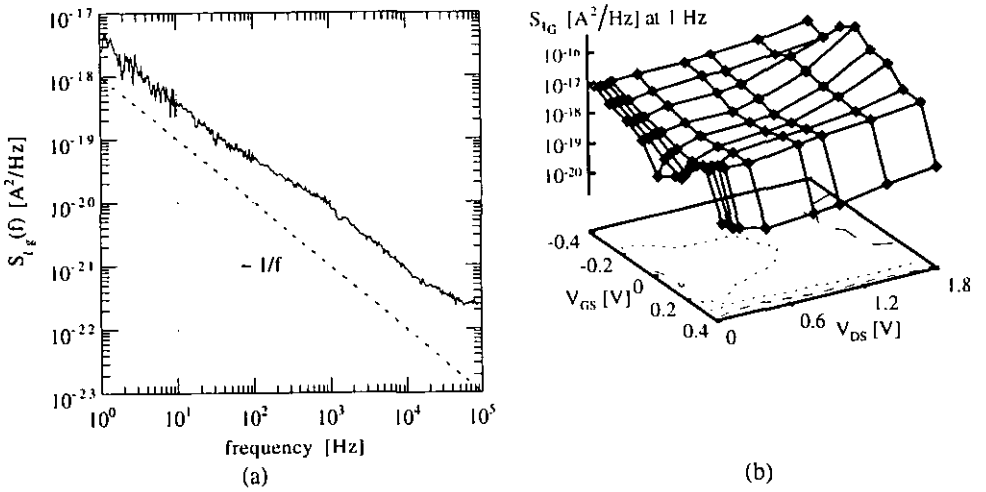

Figure 3.10. (a) Spectral gate current power density of the 0.2 μm, 50 μm InP LM HEMT used for the low-frequency gate current noise measurements. V_{DS} = 1.0 V, V_{GS} = 0 V, I_{DS} = 6.8 mA and I_G = 3.7 μA.
(b) Gate current noise S_{I_G} at $f = 1$ Hz versus V_{GS} and V_{DS}.

In order to compare the reported results presented in Figure 3.9, measurements have been carried out while drain and source contacts were short-circuited giving $V_{DS} = 0$ V. The applied gate voltages lie in the range of 10 mV to 0.27 V. The measurement results are shown in Figure 3.11.

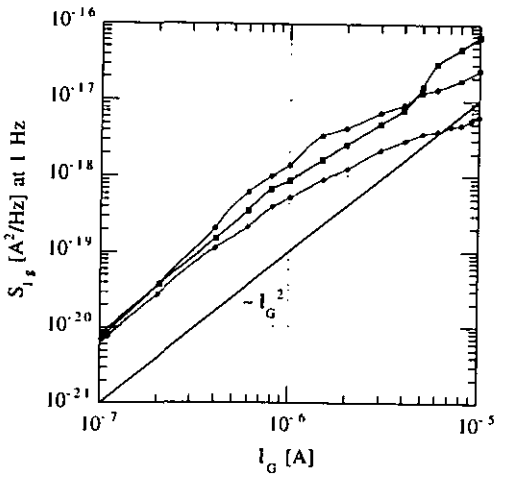

Figure 3.11. Gate current noise S_{I_G} at f = 1 Hz versus I_G, V_{DS} = 0 V. The measurement results have been scaled down to a HEMT with a gate width of 200 μm.

If we compare the noise characteristics of Figure 3.9 and 3.11 it can be concluded that the gate current noise level of the InP based HEMT lies approximately in the same range as the noise level of the GaAs based HEMT. It is clear that the measured gate current noise S_{I_G} is also proportional to I_G^2. At higher currents, however, a deviation of the I_G^2 dependence is observed.

The origin of the I_G^2 dependence is ascribed to the presence of an interface oxide between the gate metal contact and the semiconductor layer underneath [11]. Models have been proposed [16]-[18] to predict the fluctuations in the transparency of the oxide for electrons which tunnel through the interface oxide. These transparency fluctuations are explained by the Nyquist noise in the oxide layer. However, since in the processing the gate metallisation is performed directly after the gate recess, the presence of a significant interface oxide is not very likely. Besides, none of the mentioned models explain the deviation of the I_G^2 dependence of the gate current noise at higher values.

Another study [19] attributes the I_G^2 dependence to the modulation of the Schottky barrier height arising from fluctuations in the occupancy of deep traps distributed within the semiconductor layers under the gate. For higher currents a $(I_G)^\gamma$ dependence is observed, with $0 < \gamma < 2$, and is explained by the influence of the Schottky barrier's series resistance. Since we found a similar noise behaviour, our results can be explained by the modulation of the Schottky barrier height.

3.4.3 Coherence measurements

The coherence represents the statistic relation between two stochastic signals $x(t)$ and $y(t)$. For a stationary process, $\langle x(t) \rangle = 0$ and $\langle y(t) \rangle = 0$, the coherence is defined by

$$\Gamma_{x(t),\,y(t)} = \frac{\left\langle \left(x^*(t) \cdot y(t) \right)^2 \right\rangle}{\left\langle x^2(t) \right\rangle \cdot \left\langle y^2(t) \right\rangle} \tag{3.20}$$

where $x^*(t)$ is the conjugate of $x(t)$ and $0 \leq \Gamma_{x(t),\,y(t)} \leq 1$. If $x(t)$ and $y(t)$ are fully uncorrelated ($\Gamma_{x(t),\,y(t)} = 0$) the variance of the sum equals the sum of the variances, or

$$\left\langle \left(x(t) + y(t) \right)^2 \right\rangle = \left\langle x^2(t) \right\rangle + \left\langle y^2(t) \right\rangle \tag{3.21}$$

This implies that the total noise power of two fully uncorrelated noise signals can be simply obtained by adding the variances of the signals.

The coherence Γ_{I_G, I_D} between the drain and gate current noise can be obtained by simultaneously measuring the gate and drain current noise. The measurement set-up for the coherence measurements is shown in Figure 3.12a

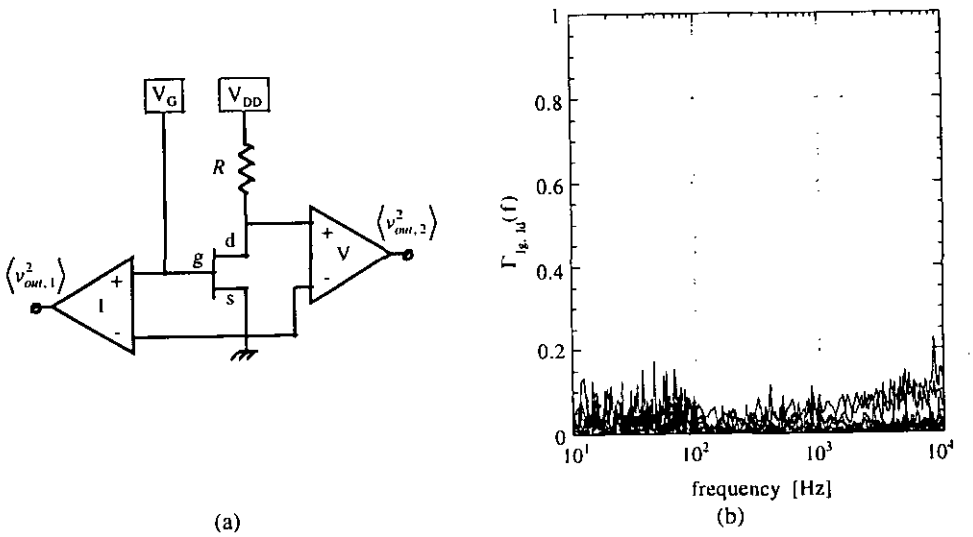

Figure 3.12. (a) Set-up for coherence measurements with the voltage amplifier EG&G Brookdeal 5003 and current amplifier 5002. The grey boxes V_{DD} and V_G are symbol for voltage supplies with built-in low-pass filters.
(b) Coherence measurements at several gate bias points in the ohmic as well as in the saturation region.

If we measure the coherence Γ_{I_G, I_D} at several gate bias points in the ohmic as well as in the saturation region between both low-frequency noise sources, i.e. gate and drain noise sources, we obtain Figure 3.12b. Although there might be no coherence between two spatially separated fluctuating conductances, the cross-correlation $\left\langle \left(x^*(t)\cdot y(t)\right)^2 \right\rangle$ can be non-negligible due to the interconnection of the Schottky barrier and channel conductances. Consequently, a low value for the coherence can be attributed to a drain-side leakage path very close to the drain or to a source-side leakage path very close to the source [20]. The low value of the coherence can physically be explained by the excellent electron confinement of the InP based HEMT which prevents the electrons in the channel from interaction with the electrons that participate to the gate current.

A significant consequence of Figure 3.12b is that due to the low coherence value the gate noise sources can be treated separately from the drain noise sources which facilitates the low-frequency noise modelling considerably.

3.5 Implementing the noise model

The results of the noise measurements can be implemented in the non-linear HEMT model present in HP MDS [21]. The graphic diagram of the bias-dependent low-frequency noise model is shown in Figure 3.13. The low-frequency noise is represented in the model by a spectral current noise source at the drain and at the gate-side parallel to the intrinsic drain current source respectively the gate and source contacts. The bias-dependent behaviour of these noise sources is achieved by considering

- the spectral power densities $S_{I_{DS}}$ and S_{I_G} at $f = 1$ Hz and

- the coefficient γ in $S_I(f) = \frac{S_I(f = 1\ \text{Hz})}{f^{\gamma}}$

as the variables which are dependent on the drain voltage V_{DS} and gate voltage V_{GS}.

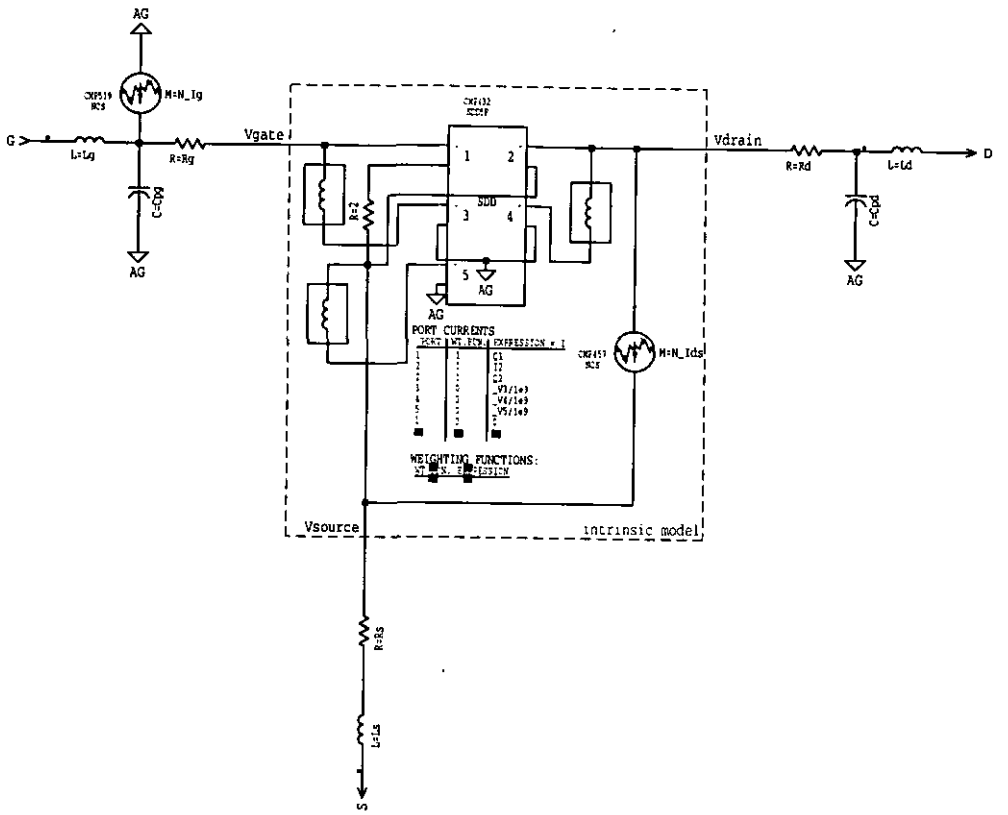

Figure 3.13. Implementation of the bias-dependent low-frequency noise model in the non-linear HEMT model present in HP MDS.

The intrinsic non-linear HEMT model is shown in Figure 3.13 within the dashed rectangle. Between the intrinsic drain and source contacts a noise current source has been added in order to provide the measured low-frequency noise behaviour at the drain-side. The value of this noise source (*N_Ids*) is calculated as described in section 3.4.1. The bias dependent behaviour is included in the model through the variables $S_{I_{DS}}(f = 1)$, γ, g_{DS} and g_m. Note that concerning the series resistances R_s and R_d we have not implemented any constant $1/f$ noise source since the measurement results (Figure 3.7) did not indicate a constant noise level at higher gate bias. Instead, a V_{DS} dependence was observed.

Next, a noise current source between the extrinsic gate and source contacts provides the measured low-frequency noise behaviour at the gate-side of the HEMT. The value of this noise source (*N_Ig*) is calculated similarly to the method described in section 3.4.2.

The noise measurements used for the model implementation have been carried out on a HEMT with a gate width of 50 μm. However, the measurement results can also be applied to devices with a different gate width if the intrinsic current noise sources, shown in Figure 3.13, are scaled to the proper magnitude. By using Hooge's relation (3.5), for stated drain and gate bias, the intrinsic noise current sources of a HEMT with gate width W can be calculated from the basic measurements by applying the following relation

$$S_I(f)\big|_W = \frac{W}{50\,\mu\text{m}} \cdot S_I(f)\big|_{50\,\mu\text{m}} \tag{3.22}$$

Since in our case the low-frequency noise measurements only produced 1/f -like spectra, the noise model has not been extended with g-r noise sources. However, the model can

easily be extended with this type of noise by adding g-r noise sources parallel to the present $1/f$ sources. The bias-dependent behaviour of the g-r noise current sources is obtained by considering

- the initial value of the noise plateau A in $S_I(f) = \frac{A}{1+(2\pi f \tau)^2}$ and
- the time constant τ

as the variables which are dependent of the drain voltage V_{DS} and gate voltage V_{GS}.

The implemented noise model is valid for spectral frequencies from 1 Hz up to, at least, 100 kHz for a drain source voltage V_{DS} between 50 mV and 1.8 V and an effective gate voltage $V_G = V_{GS} - V_T$ between -0.2 and 0.6 V.

Now that we have completed the implementation of the low-frequency noise model in HP MDS, we are able to predict, i.e. simulate the phase noise behaviour of non-linear circuits. The next step is to verify the implemented noise model by comparing measured and simulated phase noise data of a demonstrator.

In order to measure phase noise we first have to design and after that fabricate a non-linear circuit. In chapter 4 we will discuss the design and layout of a 20 GHz low phase noise oscillator. Starting from the oscillator layout the non-linear circuit can be fabricated which enables phase noise characterisation.

Chapter 4

Design and layout of a 20 GHz MMIC oscillator

4.1 Introduction

As we have accomplished the extension of the non-linear HEMT model present in HP MDS by including the low-frequency noise behaviour, we are able to optimise non-linear circuits in terms of frequency modulation or phase noise.

If the block diagram of the transceiver of Figure 1.2 is considered it is obvious that oscillators and mixers are non-linear elements in telecommunication systems. However, both elements suffer from noise up-conversion which causes phase noise. Therefore, both elements can be used for phase noise verification. Since for characterisation an oscillator does not need any extra input-signals like a mixer does, we decide the oscillator to be the verification-tool, which facilitates the phase noise characterisation significantly.

In this chapter we will discuss the properties of a microwave basic oscillator in terms of oscillation conditions, stability and phase noise based on immittances and S-parameters[1]. In section 4.5 we will explain and illustrate the design and layout of a complete oscillator with buffer amplifier and filter networks which is used for the verification of our implemented low-frequency noise model. Ultimately, from the final presented oscillator layout the optical masks can be fabricated in order to realise the coplanar MMIC with airbridges conform to the InP based HEMT technology described in chapter 2.

4.2 Oscillator topologies

There are many forms of oscillators to generate a time-varying periodic signal. In this paragraph an overview is given of transistor oscillator topologies based on immittances and S-parameters. Since there is more than one possible topology in every category we will have to select the topology that combines the most advantages in the field of design and fabrication.

4.2.1 Immittance based oscillator topologies

A stable transistor oscillator uses a resonator directly as the frequency determining circuit element. In general, a transistor oscillator can be represented as either a parallel or a series circuit as shown in Figure 4.1. The resonator can be used to realise one or more of the immittances shown in this Figure. The commonly used stable transistor oscillators can be

[1] For readers not familiar with the S-parameters and Smith charts a short introduction is included in appendix A.

divided into two types: one using the resonator as a series feedback element and the other using the resonator as a parallel feedback element.

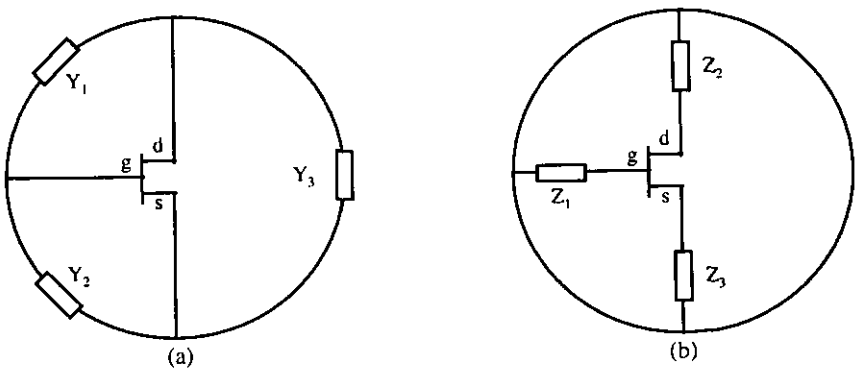

Figure 4.1 (a) Parallel transistor oscillator configuration.
(b) Series transistor oscillator configuration.

4.2.2 S-parameter based oscillator topologies

Oscillator topologies can also be distinguished based on their S-parameters. The microwave oscillator in its transmission and reflection forms, as well as the respective circuit elements are shown in Figure 4.2.

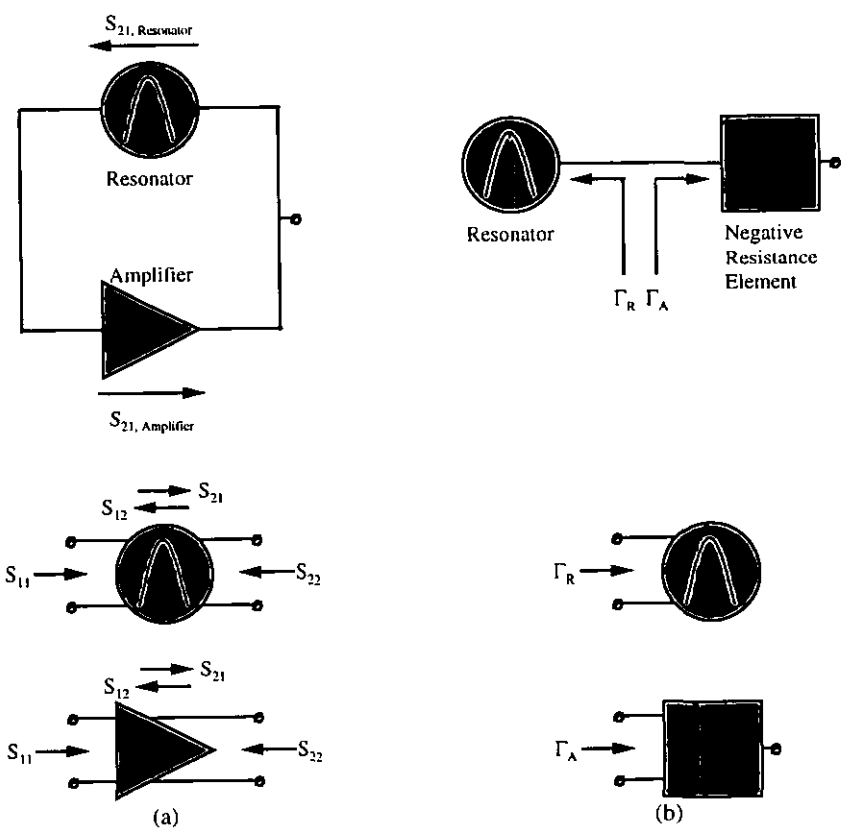

Figure 4.2 (a) Block diagram of the transmission form of oscillator.
(b) Block diagram of the reflection form of oscillator.

In both oscillator configurations a signal loop is apparent between the resonator and an amplifying element. In case of the transmission form the amplifier increases the magnitude

of the signal that comes from the resonator while the resonator chooses the oscillation frequency and decreases the magnitude of the signal due to the power dissipation of non-ideal passive circuit elements. The signal loop is visually present in the topology of the transmission form of the oscillator, which is, however, not the case in the topology of the reflection form. In case of this type of oscillator the signal is bumped up and down between the resonator and the negative resistance element ($\Gamma_A > 1$). This element consists of an active device that amplifies the incoming signal while the resonator determines the frequency and decreases the magnitude of the signal in the loop. As long as there is a unity loop gain and a zero phase loop in the signal loop a stable oscillation can be present.

If we compare the oscillator topologies it can be stated that the parallel transistor oscillator configuration shown in Figure 4.1a and the transmission form of the oscillator shown in Figure 4.2a are equivalents provided that the transistor is considered as the complete amplifying element. The same can be stated for the series transistor oscillator configuration and the reflection form of the oscillator.

Since the reflection type of oscillator does not need a separate feedback like the transmission form (Figure 4.2) it is expected that the layout of an eventual reflection type of oscillator can be realised more compact than the transmission form. Smaller circuits have also less power losses resulting in a better oscillator performance. An additional advantage of the reflection type of oscillator is the less complicated design since we only need to design one-port building-blocks. In view of these arguments we have decided to design the oscillator according to the reflection form.

The oscillator theory presented in this chapter is primarily aimed at the reflection type of oscillator or negative resistance oscillator but it is also applicable to the transmission type.

4.3 Resonator

Resonators are important components in microwave communication circuits. In oscillators they filter and select frequencies. Fields inside a resonator store energy at the resonant frequency where equal storage of electric and magnetic energies occurs.

The Q factor is an important figure of merit for a resonant circuit. The Q factor relates a resonant circuit's capacity for electromagnetic energy storage with its energy dissipation through heat. The resonator bandwidth is inversely proportional to the Q factor. Thus, high Q factor resonators have narrow bandwidths. The Q factor is defined by [22]

$$Q = 2\pi \cdot \frac{\text{Maximum energy storage during a cycle}}{\text{Average energy dissipated per cycle}} = \frac{2\pi\, W_0}{P \cdot T_{cycle}} = \frac{\omega_0 W_0}{P} \tag{4.1}$$

where W_0 is the stored energy, P the power dissipation, ω_0 the circular frequency and $T = 2\pi/\omega_0$.

When a resonant circuit is used as a load in a microwave circuit, different Q factors can be defined. The first Q factor accounts for internal losses. It is the unloaded Q factor, Q_0. Next, the external Q factor, Q_e, accounts for external losses. It is present because, in order to be useful, a resonator must be attached to some external circuit and includes both internal and external losses. The more power loss, the lower the Q. In order to relate the total loaded Q (Q_L), which is the Q for the system including power losses both internal and external to the resonator system, to the unloaded Q (Q_0) a coupling coefficient $\kappa = P_e/P_0$ can be defined where P_e and P_0 are the external and internal power dissipation, respectively. Consequently, the total loaded Q (Q_L) can be written as [22]

$$Q_L = \frac{Q_0}{1+\kappa} \tag{4.2}$$

Relationship (4.2) is useful in describing the results of measurements in terms of coupling coefficients.

If we consider the types of resonators that can be used in microwave oscillators, we can distinguish three main categories, namely

- Dielectric resonators. An important resonator circuit at microwave frequencies is the metal cylindrical hollow waveguide resonator. Very high Q factors (> 10000) and accompanying narrow bandwidths can be obtained with this component. However, this type of resonators can not be integrated in the InP based HEMT MMIC technology and therefore, if used, should be placed off-chip.
- Lumped element resonators. Discrete components like inductors and capacitors can be integrated in the InP based HEMT technology forming a lumped element resonator as demonstrated for example in Figure 4.3. A disadvantage of these resonators is the low Q factor (< 100).

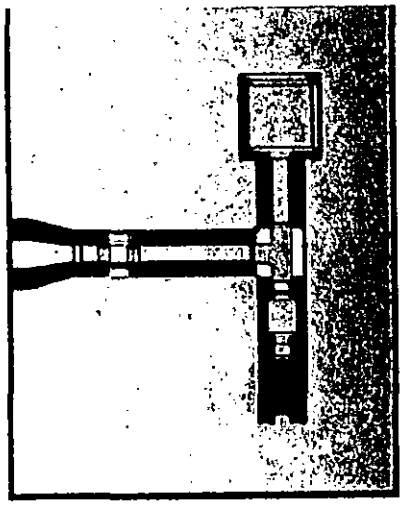

Figure 4.3 Example of a lumped element resonator. The length and width of the resonator is 600 and 800 μm, respectively.

- Transmission line resonators. To design a resonator using microstrip or coaxial lines at microwave frequencies, one has to choose the correct length such that the susceptance is zero or infinity. This corresponds to resonance or anti-resonance, respectively. The first resonance at f_0 = 20 GHz occurs when the transmission line has a length of approximately 3.8 mm.

As we intend to realise a monolithic circuit all circuit elements have to be integrated on the same substrate which means that no dielectric resonator can be used. Since the transmission line resonator's length of approximately 3.8 mm is rather large compared to common microwave oscillator dimensions, we have decided to use a lumped element resonator in our design. Although its Q is rather low, this type of resonator can be integrated on the same InP substrate.

4.4 Theory of negative resistance oscillators

In this section, we will discuss general conditions that must be satisfied by an oscillator in steady-state [2], [23]. The oscillator theory is used to describe and predict the non-linear behaviour of oscillators. First we will discuss the behaviour of an oscillator qualitatively from start-up to the final steady-state operation. Consequently, we will present oscillation conditions in terms of impedances and S-parameters.

4.4.1 Working principle of an oscillator

In contrast to conventional Si based oscillators where the principle of oscillation is to alternately charge and discharge a capacitance, the principle of high-frequency oscillators is to 'amplify noise in a very narrow band'. The oscillation starts from an initial noise level and is built up to the final steady-state with a unity loop gain and a zero phase loop.

The upper curve of Figure 4.4a, shows the oscillator's open-loop gain. The loop gain is greater than unity only over a small part of the gain curve. As long as this holds a signal will grow with centre frequency f_0. The resulting bandwidth is called the oscillator bandwidth and is indicated in Figure 4.4a by A.

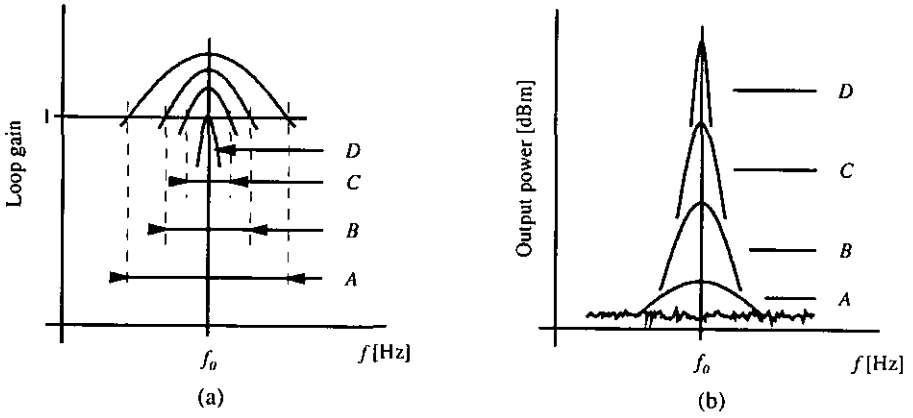

Figure 4.4 Oscillation amplitude growth (a) Loop gain.
(b) Output power.

At the loop closure, the noise at the input of the amplifying active device appears as the noise level shown in Figure 4.4b. This noise is propagated around the loop and returns to the input to appear as curve A in Figure 4.4b. It has experienced a shaping due to the feedback characteristics of the circuit: the components of noise around f_0 have suffered both phase shift and amplitude change, causing the noise in the oscillator bandwidth to peak as shown. Further propagation around the loop produces curves B, C and, subsequently, D. The oscillator signal growth is continuous and smooth.

Continuation of this amplitude growth eventually produces a signal that has reached the level that affects the non-linear amplifying device (HEMT) in the circuit. This results in amplitude limiting. Amplitude increase reduces loop gain, although still greater than unity. The loop gain moves down toward the unity gain level resulting in the initial oscillator bandwidth to narrow to the so-called closed-loop bandwidth as is indicated in Figure 4.4a by B, C and ultimately D.

The final steady-state oscillation is a signal with a very narrow bandwidth which is not a stable signal, but is fluctuating continuously, in both amplitude and frequency. This represents a carrier being simultaneously amplitude and phase modulated.

This principle of oscillation applies to a transmission as well as to a reflection type of oscillator. In the latter, the signal reflects back and forth between the negative resistance and the resonator. As it reflects from the resonator the amplitude and phase are changed. Reflection from the negative resistance increases the amplitude above that of its previous pass and also shifts its phase because of the circuit reactances. So the signal changes in each pass as in the transmission type of oscillator.

4.4.2 Derivation of the oscillator equation

The design of a negative resistance oscillator starts with the fundamental oscillator equation. Figure 4.5a shows the general schematic diagram of a negative resistance oscillator. $Z_R(\omega)$ is the impedance of the resonator circuit presented to the terminals of the device. The network between the device and the load may have multiple resonant

frequencies, which means that oscillations are possible at multiple frequencies. Our goal is to derive oscillation conditions at the fundamental frequency in terms of the device impedance and the circuit impedance. Consequently, we can reconfigure the schematic so that the device terminals separate the circuit and device parts of the oscillator as shown in Figure 4.5b. Because oscillations in a free-running oscillator are induced by DC bias transients or by noise, a source $e(t)$ which initiates the oscillations has been added to the circuit.

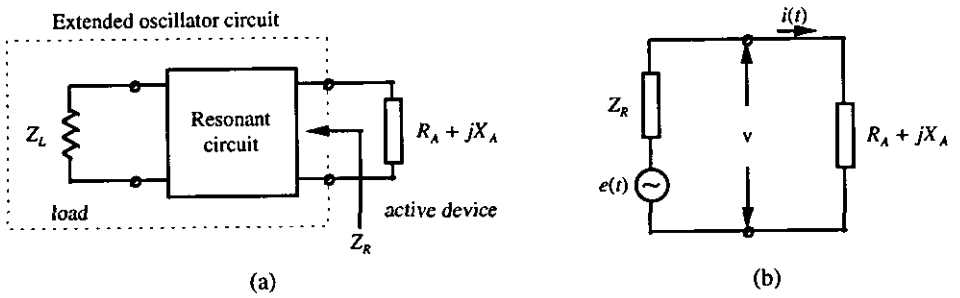

Figure 4.5 (a) Negative resistance oscillator schematic diagram.
(b) Equivalent circuit of the negative oscillator.

There are two equations that describe the oscillator. The first equation expresses the HF current flowing through the oscillator as

$$i(t) = \mathrm{Re}\{I(t)\} = A(t)\cdot\cos[\omega t + \phi(t)] \tag{4.3}$$

where

$$I(t) = A(t)\cdot\exp\left(j[\omega t + \phi(t)]\right) \tag{4.4}$$

$A(t)$ and $\phi(t)$ are unknown amplitude and phase variables and are assumed to vary slowly with time compared to the current $i(t)$. $A(t)$ is directly related to the oscillator HF power level. The device impedance is assumed to be a function of $A(t)$ only and the circuit impedance Z_R is assumed to be a function of the oscillator fundamental frequency ω only. The oscillator equation has solutions of ω at frequencies where oscillations can be sustained.

The second equation that describes the oscillator is the voltage loop relation around the circuit in Figure 4.5b

$$v(t) + \mathrm{Re}\{Z_R(\omega)\cdot I(t)\} = e(t) \tag{4.5}$$

Solving equations (4.3) and (4.5) will give expressions for $A(t)$ and $\phi(t)$ in terms of the circuit and device impedances. The detailed derivation of the oscillator equation is presented in Appendix B.2. The oscillator equation is obtained under steady-state, free-running conditions, i.e. $e(t) = 0$, $dA/dt = 0$ and $d\phi/dt = 0$. Consequently, as derived in Appendix B.2 we obtain the final result, the oscillator equation

$$\begin{aligned} R_R(\omega) + R_A(A) + j[X_R(\omega) + X_A(A)] &= 0 \\ \Rightarrow \quad Z_R + Z_A &= 0 \end{aligned} \tag{4.6}$$

The oscillation conditions have been derived in terms of the device and circuit impedances. The oscillation criteria can also be presented in terms of reflection coefficients. This can be done by rewriting (4.16) using the relation

$$Z = Z_0 \cdot \frac{1+\Gamma}{1-\Gamma} \tag{4.7}$$

where Z_0 is the characteristic impedance of the oscillator system and Γ the reflection coefficient of the impedance Z. Combining (4.6) and (4.7) results in

$$\begin{aligned} &\frac{1+\Gamma_R}{1-\Gamma_R}+\frac{1+\Gamma_A}{1-\Gamma_A}=0 \\ &\Rightarrow \quad \Gamma_R\cdot\Gamma_A=1 \end{aligned} \tag{4.8}$$

If the resonant circuit is passive then Γ_R will be between 0 and 1 in magnitude. Thus, in order to have oscillation, Γ_A will require a magnitude that is greater than unity.

4.4.3 Stability

Oscillations are possible if the device and circuit impedances satisfy (4.6). However, if the oscillator suffers from small electrical disturbances such as a change in the DC bias point, the oscillations may cease after a few cycles or they may increase in amplitude until the device fails. In case of a disturbance a stable oscillator will return to its steady-state operating-point. We can derive a stability condition by perturbing the oscillation amplitude by a small amount $\delta A(t)$ from the steady-state value A_0. Stable oscillations are generated if $d(\delta A)/dt < 0$ which implies that the perturbed oscillator returns to the steady-state operating point.

The stability condition can be defined as [23]

$$S = R_R'(\omega_0)\frac{\partial R_A}{\partial A}\left[\tan\theta_R-\tan\theta_A\right] \tag{4.9}$$

where

$$\begin{aligned} \tan\theta_R &= \frac{X_R'(\omega_0)}{R_R'(\omega_0)} \\ \tan\theta_A &= \frac{\partial X_A/\partial A}{\partial R_A/\partial A} \end{aligned} \tag{4.10}$$

with $X_R'(\omega_0)$ and $R_R'(\omega_0)$ the first derivatives to ω at ω_0. A detailed derivation of the stability condition is presented in Appendix B.3. The stability condition demonstrates that the stability of an oscillator depends on the electrical characteristics of both its resonant circuit, the resonator and the active device.

As with the oscillation conditions we can rewrite (4.9) in terms of reflection coefficients. The reflection coefficients Γ_R and Γ_A can be defined as

$$\begin{aligned} \Gamma_R(\omega) &= \gamma_R(\omega)\cdot\exp\left(j\psi_R(\omega)\right) \\ \Gamma_A(\omega) &= \gamma_A(\omega)\cdot\exp\left(j\psi_A(A)\right) \end{aligned} \tag{4.11}$$

where γ_R and γ_A are the magnitude of the reflection coefficients. If a microwave oscillator is operating in steady state and under stable conditions, its reflection coefficients must satisfy the following stability condition

$$S = \gamma_R\frac{d\gamma_A}{dA}\cdot\frac{d\psi_R}{d\omega}-\gamma_A\frac{d\psi_A}{dA}\cdot\frac{d\gamma_R}{d\omega}>0 \tag{4.12}$$

If we plot Γ_R and Γ_A^{-1} on a Smith chart, we can analyse graphically the performance of an oscillator in the complex R-X plane. Figure 4.6 shows the intersection of the two reflection coefficient loci. Employing cylindrical co-ordinates, the stability condition can be rewritten as

$$S = \left|\frac{d\Gamma_R}{d\omega}\right| \cdot \left|\frac{d\Gamma_A^{-1}}{dA}\right| \cdot \sin\theta > 0 \tag{4.13}$$

For S in this form, an oscillator is clearly stable when the angle θ is between 0° and 180°.

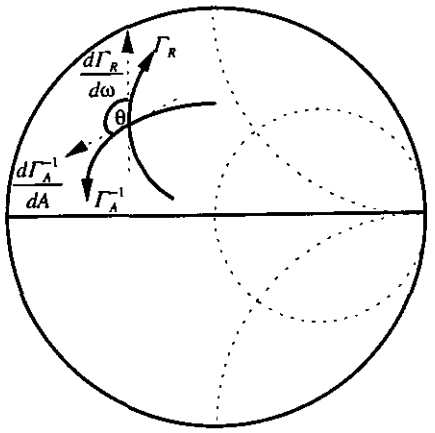

Figure 4.6 Reflection coefficients Γ_R and Γ_A^{-1} on the Smith chart.

4.4.4 Amplitude and frequency modulation

In this section we will discuss the oscillator amplitude modulation (AM) and frequency modulation (FM) or phase noise. The results of two studies [1] and [23], which describe the oscillator noise spectra, are presented. From each study, conclusions can be drawn which are of importance for the design of low phase noise microwave oscillators.

Noise spectra derived from the oscillator conditions [23]

Firstly, starting from the initial oscillator conditions presented in section 4.4.2 expressions of the amplitude and frequency modulation can be derived. The derivations of the noise spectra are summarised in Appendix B. The presented approach results in the following noise equations

$$\left|\delta A(\omega_m)\right|^2 = \frac{2\cdot\left|Z_R'(\omega_0)\right|^2\cdot|e|^2}{\omega_m^2\left|Z_R'(\omega_0)\right|^4 + A_0^2 S^2}$$

$$\left|\phi(\omega_m)\right|^2 = \frac{2\cdot|e|^2}{\omega_m^2 A_0^2}\,\frac{\omega_m^2\left|Z_R'(\omega_0)\right|^2 + A_0^2\left[\left(\frac{\partial R_A}{\partial A}\right)^2 + \left(\frac{\partial X_A}{\partial A}\right)^2\right]}{\omega_m^2\left|Z_R'(\omega_0)\right|^4 + A_0^2 S^2} \tag{4.14}$$

where $\left|\delta A(\omega_m)\right|^2$ and $\left|\phi(\omega_m)\right|^2$ describe the amplitude modulation (AM) and frequency modulation (FM) of the electromagnetic output of an oscillator in terms of the power spectral density.

Equation (4.14) can also be written in terms of reflection coefficients. Expressions for the amplitude and frequency modulation at the modulation frequency ω_m are

$$\left|\delta A(\omega_m)\right|^2 = \frac{\frac{1}{\gamma_R^2}\cdot\left|\frac{d\Gamma_R}{d\omega}\right|^2 2\cdot|b_n|^2}{|A_0|^2\frac{1}{\gamma_R^2}S^2+\frac{1}{\gamma_R^4}\left|\frac{d\Gamma_R}{d\omega}\right|^4\omega_m^2}$$

$$\left|\phi(\omega_m)\right|^2 = \frac{2\cdot|b_n|^2}{\omega_m^2|A_0|^2}\cdot\frac{\frac{1}{\gamma_R^2}\left|\frac{d\Gamma_A^{-1}}{dA}\right|^2|A_0|^2+\frac{1}{\gamma_R^2}\left|\frac{d\Gamma_R}{d\omega}\right|^2\omega_m^2}{|A_0|^2\frac{1}{\gamma_R^2}S^2+\frac{1}{\gamma_R^4}\left|\frac{d\Gamma_R}{d\omega}\right|^4\omega_m^2} \qquad (4.15)$$

where $b_n = |e|^2\cdot|1-\Gamma_A|^2/4Z_0|\Gamma_A|^2$. At low modulation frequencies, i.e. close to the carrier frequency, the phase noise expressions of equations (4.26) and (4.27) show a $1/\omega_m^2$ behaviour which is accounted for by the thermal noise in the oscillator circuit. Like thermal noise, $1/f$ noise is up-converted by non-linearities in the active device to the carrier frequency. Consequently, the loop transfer characteristic of the oscillator, including the resonator, filters the output voltage, producing a $1/\omega_m^3$ characteristic [3]. The $1/f$ noise which is responsible for the $1/\omega_m^3$ dependence, however, is not included in the derivations of equations (4.14) and (4.15).

From equation (4.15) it can be concluded that good noise performance can be achieved if

- The circuit and inverse device reflection coefficient loci intersect in an orthogonal manner. This implies a maximum stability S resulting in lower amplitude and frequency modulation.
- $\left|\frac{1}{\gamma_R}\frac{d\Gamma_R}{d\omega}\right|$ takes on its maximum value.
- $\left|\frac{1}{\gamma_R}\frac{d\Gamma_A^{-1}}{dA}\right|$ takes on its minimum value.

Noise spectra derived from the non-linear device elements [1]

Secondly, the noise analysis of a microwave oscillator can be based upon the non-linear elements present in the active device. The analysis described in this section is based on the HEMT oscillator model shown in Figure 4.7. The oscillator is divided into a linear and a non-linear two-port network. The non-linear part contains the dominant non-linear elements of the HEMT equivalent circuit, namely, the gate-source capacitance c_g, the transconductance g_m and the drain conductance g_d. The linear HEMT elements are combined with the remaining oscillator circuit and the load to form the linear two-port network. The low-frequency noise of the HEMT is modelled as a voltage source $e(t)$ in the gate circuit.

If we consider the general oscillation conditions derived in section 4.4.2, $e(t)$ is set to zero. Then, for a stationary oscillation with frequency ω_0, the voltages v_1, v_2 and currents i_1, i_2 are strictly periodic functions of time. The same holds for c_g, g_m and g_d which hence can be expanded into Fourier series

$$c_g(t) = \sum_{k=-\infty}^{\infty} c_{gk}\cdot e^{jk\omega_0 t}$$

$$g_m(t) = \sum_{k=-\infty}^{\infty} g_{mk}\cdot e^{jk\omega_0 t} \qquad (4.16)$$

$$g_d(t) = \sum_{k=-\infty}^{\infty} g_{dk}\cdot e^{jk\omega_0 t}$$

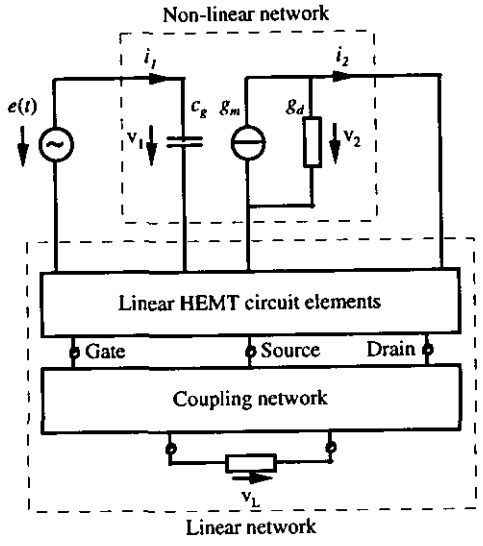

Figure 4.7 HEMT oscillator model including a linear and a non-linear part [1].

where c_{g0}, g_{m0} and g_{d0} are the time average values. Provided that a stable oscillation with frequency ω_0 and complex amplitudes V_1, V_2 and I_1, I_2 exists, the low-frequency voltage $e(t)$ shown in Figure 4.7 will cause low-frequency amplitude and phase fluctuations of the HF voltages and currents. The amplitude and phase fluctuations can be calculated based on this analysis and result in the following expressions [1]

- amplitude fluctuations

$$\begin{aligned}\frac{\Delta V_1}{|V_1|} &= -\frac{2g_{m1}}{A}\frac{E}{|V_1|}\\ \frac{\Delta V_2}{|V_2|} &= \frac{2g_{m1}T_{11u}}{A}\frac{E}{|V_1|}\end{aligned} \tag{4.17}$$

- phase fluctuations

$$\begin{aligned}\Delta\phi_1 &= 2\omega_0 c_{g2}\frac{T_{12u}(g_{d0}-g_{d2})+T_{22u}}{B}\cdot\left(\frac{2g_{m1}}{A}-\frac{c_{g1}}{c_{g2}}\right)\cdot\frac{E}{|V_1|}\\ \Delta\phi_2 &= 2\omega_0 c_{g2}\frac{T_{12u}(g_{m0}-g_{m2})-\det(T)_u}{B}\cdot\left(\frac{2g_{m1}}{A}-\frac{c_{g1}}{c_{g2}}\right)\cdot\frac{E}{|V_2|}\end{aligned} \tag{4.18}$$

where

$$\begin{aligned}A &= g_{m0}+g_{m2}+T_{11u}(g_{d0}+g_{d2})+T_{21u}\\ B &= g_{m0}-g_{m2}+T_{11u}(g_{d0}-g_{d2})+T_{21u}\\ \det(T)_u &= T_{11u}T_{22u}-T_{12u}T_{21u}\\ \begin{bmatrix}V_2\\ I_2\end{bmatrix} &= \begin{bmatrix}T_{11} & T_{12}\\ T_{21} & T_{22}\end{bmatrix}\cdot\begin{bmatrix}V_1\\ I_1\end{bmatrix}\end{aligned}$$

From equations (4.17) and (4.18) it can be concluded that amplitude modulation is caused by the non-linearity of the transconductance g_m; phase noise is primarily caused by the non-linearity of the gate-source capacitance c_g since in common microwave oscillators $c_{g1}/c_{g2} >> 2g_{m1}/A$ [1]. Further, it can be stated from equations (4.17) and (4.18) that no AM to FM or FM to AM conversion takes place.

From the presented noise analysis, it follows that in order to minimise the noise level in a microwave oscillator we can, amongst others, determine the HEMT's DC operating-point at which the gate-source capacitance C_{GS} and the intrinsic transconductance g_m are (at most) linear. To obtain this operating-point, we have plotted the first derivative of the gate-source capacitance dC_{GS}/dV_{GS} and the intrinsic transconductance dg_m/dV_{GS} in Figures 4.8a and 4.8b, respectively.

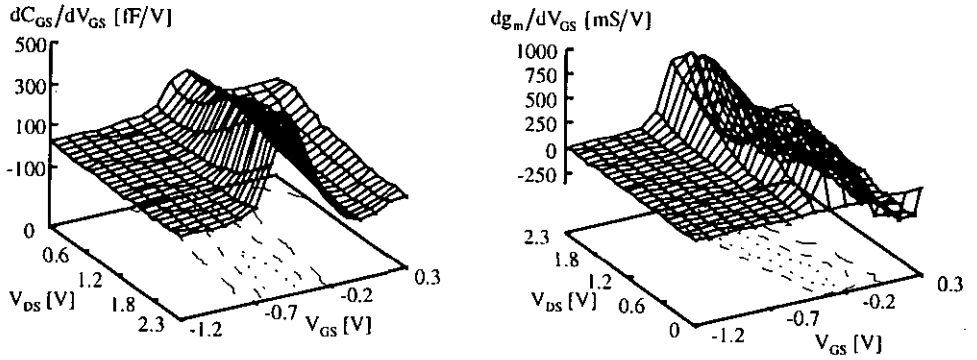

(a) (b)

Figure 4.8 First derivative of (a) the gate source capacitance dC_{GS}/dV_{GS} and (b) the intrinsic transconductance dg_m/dV_{GS} of a 150 µm InP based HEMT as function of V_{GS} and V_{DS}.

From Figure 4.8, it is clear that dC_{GS}/dV_{GS} and dg_m/dV_{GS} are primarily functions of V_{GS} rather than V_{DS}. It can be concluded that the linear regime of C_{GS} and g_m, i.e. the constant regime of dC_{GS}/dV_{GS} and dg_m/dV_{GS} shown in Figures 4.8a and 4.8b, consists of two distinguishable regions, namely for V_{GS} below approximately -0.7 V and V_{GS} above approximately -0.2 V.

In the linear regime of the transconductance g_m, the first region (V_{GS} < -0.7 V) corresponds to the sub-threshold region where only small signals will be present in the

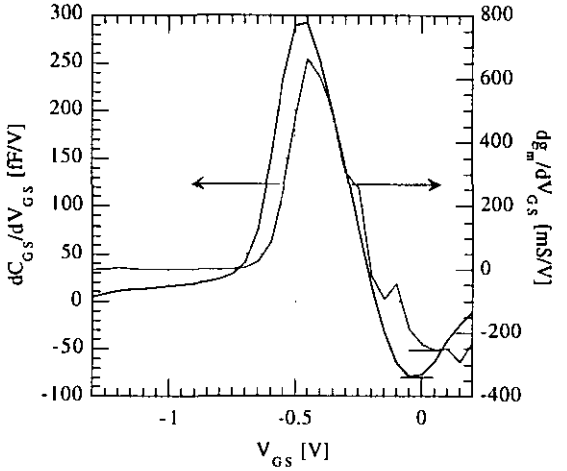

Figure 4.9 First derivative of the gate source capacitance dC_{GS}/dV_{GS} and the intrinsic transconductance dg_m/dV_{GS} of a 150 µm InP based HEMT at V_{DS} = 1.0 V.

oscillator circuit. It may be clear that this region is not of interest for the design of our oscillator. In the second region (V_{GS} > -0.2 V), both the dC_{GS}/dV_{GS} and dg_m/dV_{GS} characteristics have partially constant courses, which corresponds to partially linear courses

of C_{GS} and g_m. For the chosen drain bias of V_{DS} = 1.0 V, both characteristics are presented in Figure 4.9.

Figure 4.9 shows that both characteristics follow a constant course at $V_{GS} \approx 0.0$ V. This implies that C_{GS} as well as g_m are linear at this operating-point. Hence, we have decided to bias the HEMT at V_{GS} = 0.0 V and V_{DS} = 1.0 V for the design of our oscillator.

Note that biasing the HEMT at this DC operating point has only a limited effect on the noise performance of the oscillator. The oscillator is a non-linear circuit producing large harmonic signals which will affect the non-linear elements in the active device. However, it is assumed that biasing the HEMT in the determined operating-point will have a positive effect upon the noise performance of the oscillator circuit.

4.5 Design of the basic oscillator

In this section, we will discuss and illustrate the design of the 'basic oscillator'. The basic oscillator is formed by the circuit elements necessary to start-up an oscillation: the resonator and a negative resistance element, the HEMT. While optimising the design of the basic oscillator circuit, we can consider three design criteria which determine the overall oscillator performance, namely

- maximum output power
- minimum distortion. The distortion is a measure for the purity of the harmonic output signal of an oscillator. If we consider for example the output power spectrum shown in Figure 4.10,

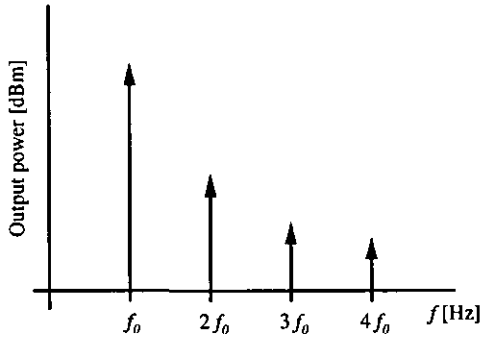

Figure 4.10 Output power spectrum of an oscillator with resonant frequency f_0.

we can define the distortion D as

$$D = \frac{\sum_{n=2}^{\infty} \sqrt{\left(P_{out,\,n^{th}\ harmonic}\right)^2}}{P_{out,\,fundamental}} \tag{4.19}$$

where $P_{out,\,fundamental}$ is the output power of the oscillator at frequency f_0.

- minimum phase noise

If the design criteria are considered, it can be stated that the output power as well as the distortion can also be improved after the design of the basic oscillator by adding microwave filters and amplifiers to the basic oscillator circuit. The oscillator's phase noise performance, however, can not be improved afterwards since the noise is located too close to the carrier. Therefore, we have decided to consider the phase noise as the most important criterion for the design of the basic oscillator.

4.5.1 Negative resistance

Transistors form a three-terminal network and there are many ways to apply feedback between any two of the terminals to cause a negative resistance at the third terminal. The negative resistance can be created by introducing reactive elements in the feedback loop of the HEMT. Besides, introducing reactive elements above resistive elements avoids signal power loss and additional noise effects.

For example, a negative input resistance at the gate-terminal of a HEMT can be obtained by introducing a feedback capacitance C_{FB} between source and ground contacts as is shown in Figure 4.11a. A simplified small-signal representation of this configuration is shown in Figure 4.11b.

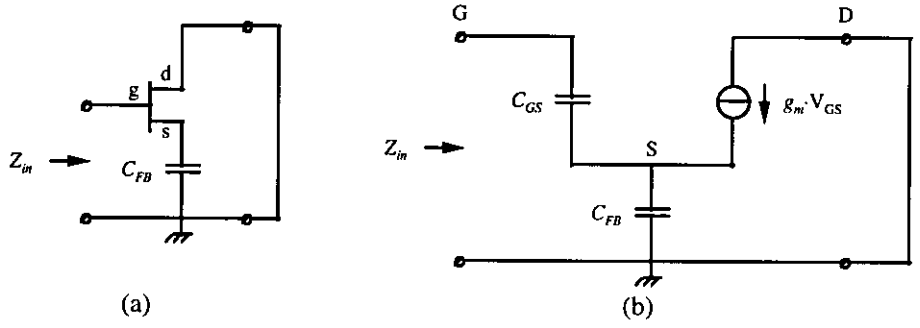

Figure 4.11 (a) Negative input resistance at the gate-terminal of a HEMT.
(b) Simplified small-signal model.

After some calculations, the input resistance of the circuit shown in Figure 4.11b is obtained and equals

$$Z_{in} = -\frac{g_m}{\omega^2 C_{FB} C_{GS}} - j \cdot \frac{C_{FB} + C_{GS}}{\omega^2 C_{FB} C_{GS}} \tag{4.20}$$

where C_{GS} is the gate-source capacitance, g_m the transconductance and ω the circular frequency. Although we used a simplified small-signal model equation (4.20) shows that a negative resistance can easily be obtained by adding a reactance. A summary of transistor configurations which can be used to obtain a negative resistance is shown in Figure 4.12.

The rectangles shown in Figure 4.12 represent either inductive or capacitive reactances. The kind of reactance depends on the applied configuration which is used to achieve the negative input resistance.

Two commonly used configurations are the common-source capacitive feedback (Figure 4.12a) and the common-gate inductive feedback (Figure 4.12f). Each configuration has its own advantages, e.g. the common-source configuration (Figure 4.12a) is more often used for amplifiers, common-drain (Figure 4.12c) for medium power oscillators and common-gate (Figure 4.12f) for wideband oscillators [22].

By simulating the S-parameters in HP MDS we can determine the value of the negative resistance of each configuration, i.e. the magnitude and phase of the reflection coefficients. A magnitude larger than unity for $|S_{11}|$ or $|S_{22}|$ points to amplification of an incoming microwave signal and corresponds with a negative resistance.

The negative resistance simulation set-up as well as the simulation results of a 150 µm HEMT using a common-source configuration with capacitive feedback is shown in Figure 4.13. The value of the feedback capacitance is 300 fF, the output is connected to ground through a 50 Ω resistance. In conformity with the phase noise analysis presented in section 4.4.4 the drain and gate bias are 1.0 V and 0.0 V, respectively.

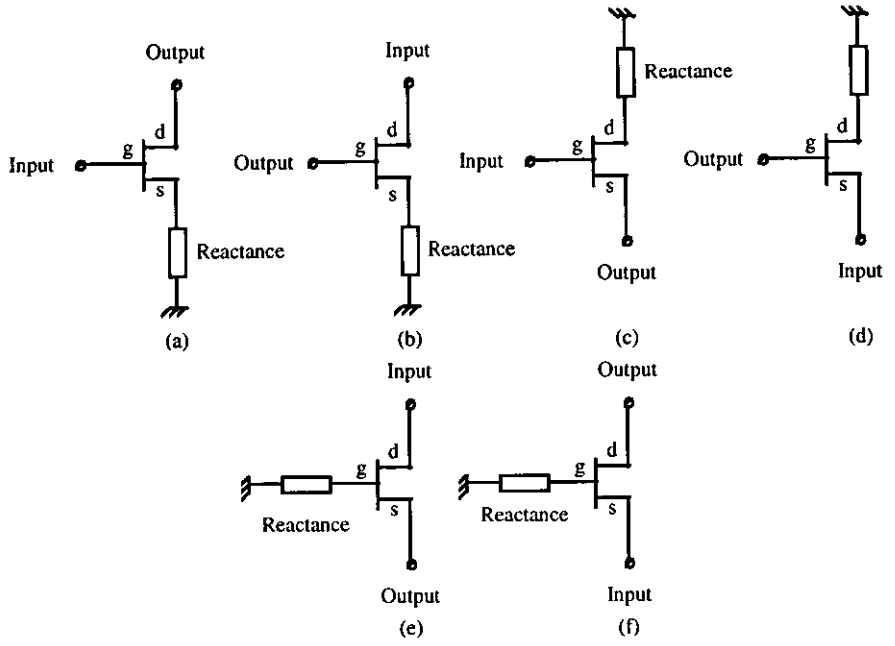

Figure 4.12 Summary of negative resistance transistor configurations.

At this point it is not clear which configuration will result in the best performing oscillator which produces the least amount of phase noise. Although we can determine the value of the reactance at which the magnitude of the reflection coefficient has its maximum, this is no guarantee for minimum phase noise performance. Therefore, we will have to optimise each basic oscillator configuration by simulating the phase noise as function of the variable circuit parameters, like the reactance, the output impedance and the gate width. Consequently, from the obtained simulation results we can acquire the optimum configuration.

Before an optimisation step can be performed we have to determine the type and value of the applicable reactance in each particular configuration. In Table 4.1 the simulation results are shown of a 150 μm HEMT.

Table 4.1 Overview of applicable reactances in order to acquire a negative resistance. Results are related to the non-linear model of a 150 μm InP based HEMT.

Configuration[1]	X_{min}	X_{opt}	$\lvert S_{11}\rvert_{max}$	$\lvert S_{21}\rvert_{max}$	X_{max}
CS gate-input	C_{min} = 0 fF	C_{opt} = 442 fF	2.0	7.0	C_{max} = 5.06 pF
CS drain-input	C_{min} = 0 fF	C_{opt} = 269 fF	1.3	0.16	C_{max} = 548 fF
CD gate-input	L_{min} = 0 nH	L_{opt} = 1.64 nH	7.8	9.9	L_{max} = 2.49 nH
CD source-input	L_{min} = 578 pH	L_{opt} = 1.64 nH	10.4	7.1	L_{max} = 2.77 nH
CG source-input	L_{min} = 509 pH	L_{opt} = 1.38 nH	3.7	4.8	L_{max} = 2.51 nH
CG drain-input	L_{min} = 7.42 pH	L_{opt} = 1.22 nH	1.5	1.6	L_{max} = 1.39 nH

[1] Notation: CS ≡ common-source configuration; gate-input ≡ resonator is connected to the gate terminal. Other abbreviations have similar meanings.

The input resistance of the specific configuration turns negative if the reactance X_{min}, either inductive or capacitive, is used as feedback. The maximum magnitude of the reflection coefficient is obtained at X_{opt}. The input resistance turns back positive at X_{max}. The range of values between X_{min} and X_{max} of each specified reactance can be applied to a configuration as shown in Figure 4.14a in order to optimise the configuration. Similar to Table 4.1, simulation results have been obtained from HEMTs with gate widths of 50, 100 and 200 μm, respectively.

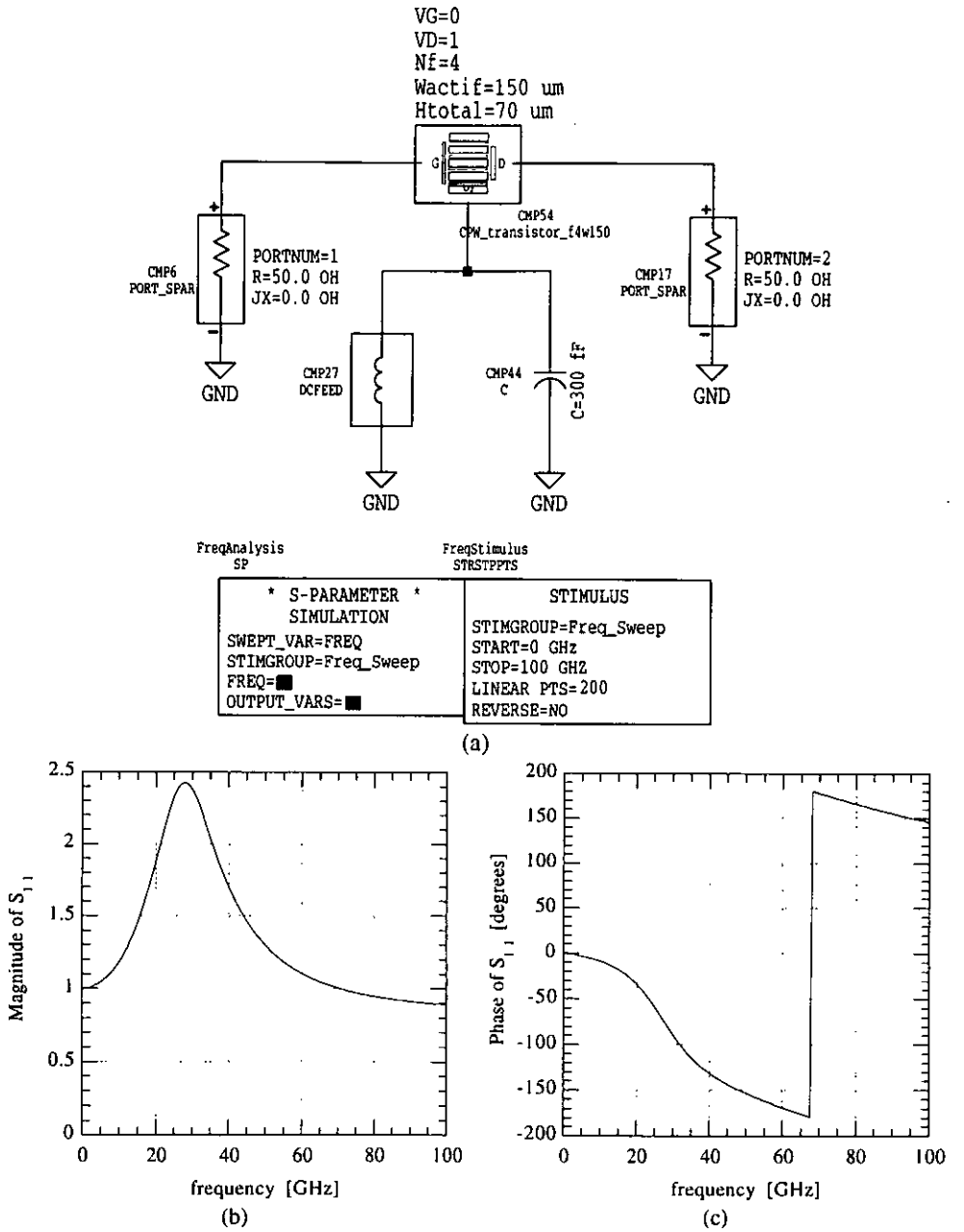

Figure 4.13 (a) Negative resistance simulation of the common-source configuration.
(b) Magnitude of reflection coefficient Γ_{in} of the common-source configuration.
(c) Phase of reflection coefficient Γ_{in} of the common-source configuration.

4.5.2 Optimising the basic oscillator

In HP MDS we are able to simulate the oscillator's phase noise performance. The basic oscillator can be optimised in terms of phase noise performance just by varying the value of the feedback reactance, the output impedance and the HEMT's gate width. Figure 4.14 shows the optimisation set-up of the common-source capacitive feedback configuration of a HEMT with a 150 µm gate width. To optimise the output impedance both inductive and capacitive loads have been applied. An overview of these loads is shown in the Smith chart of Figure 4.14b.

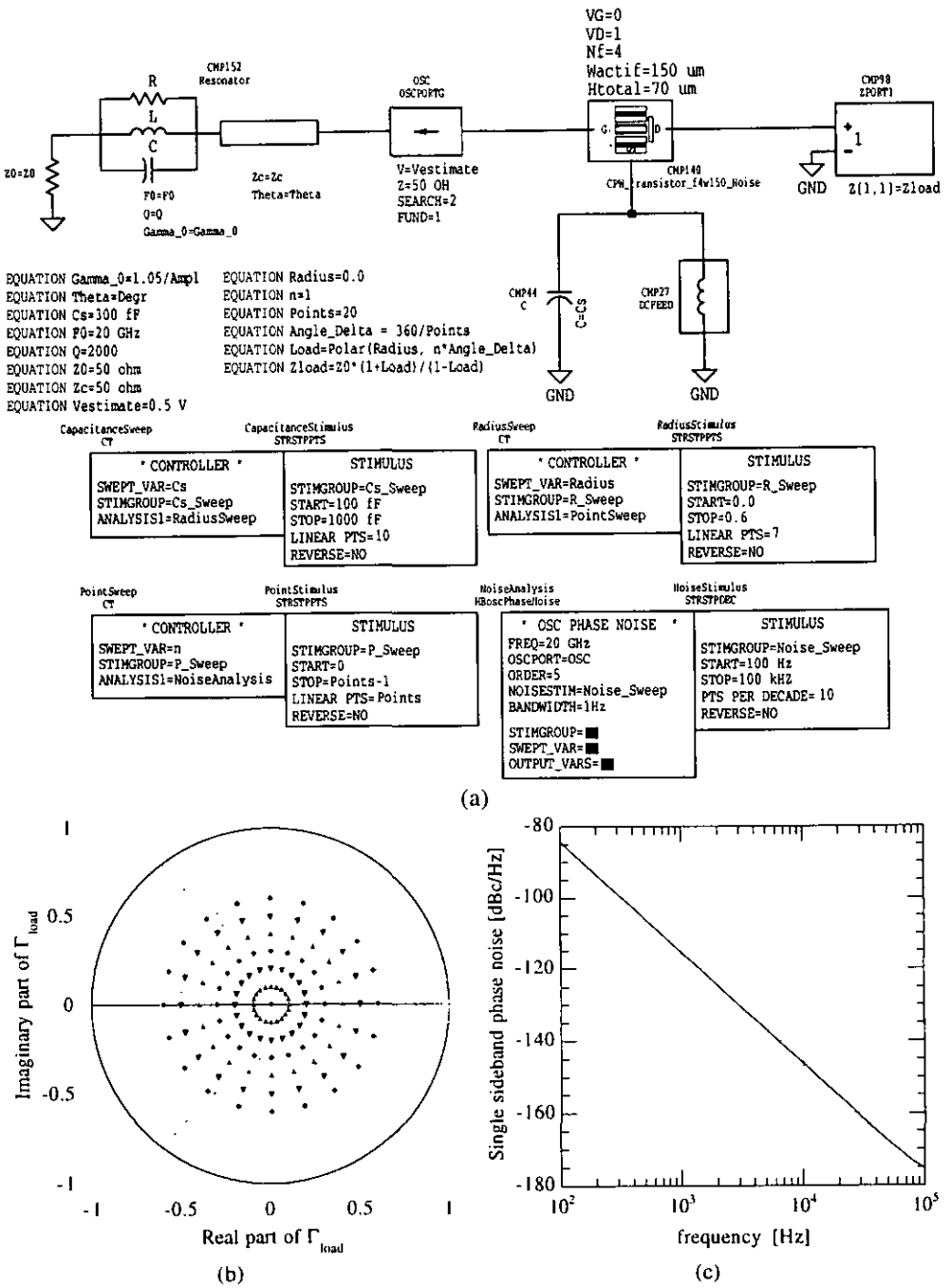

Figure 4.14 (a) Phase noise simulation of the common-source configuration (CS gate-input) as function of the value of the feedback capacitance and output impedance.
(b) Various inductive as well as capacitive loads plotted on the Smith chart.
(c) Phase noise simulation result of the optimised configuration.

In the simulations the Q factor of the resonator has been chosen high enough (Q = 2000) in order to obtain the ideal values of the reactance and the output impedance for optimum phase noise performance. For the small-signal loop gain a value of 1.05 has been chosen in all phase noise simulations. The result of the phase noise simulation of the optimised configuration is shown in Figure 4.14c. The low level of the phase noise shown in this Figure can be attributed to the use of ideal components and the high value of the resonator's Q factor.

The simulation results of the phase noise optimisation are summarised in Table 4.2. The gate width of the used HEMT amounts 150 μm.

Table 4.2 Overview of the phase noise simulation results as function of the value of the feedback reactance and the output impedance. Results are related to the non-linear model of a 150 μm InP based HEMT.

Configuration	Phase noise at f_m = 1 kHz	X_{opt}	Z_{out} [Ω]	Power [dBm]	Distortion [%]
CS gate input	-115.4 dBc/Hz	C_{opt} = 300 fF	31.5 + j16.8	7.94	32.7
CS drain input	-109.7 dBc/Hz	C_{opt} = 200 fF	50.3 + j31.5	-0.31	40.5
CD gate input	-110.1 dBc/Hz	L_{opt} = 533 pH	33	0.79	15.8
CD source input	-111.3 dBc/Hz	L_{opt} = 1.38 nH	85.0 - j66.6	-26.4	4.0
CG source input	-98.5 dBc/Hz	L_{opt} = 1.6 nH	18.2 + j14.3	-7.50	5.0
CG drain input	-103.9 dBc/Hz	L_{opt} = 900 pH	15.5 + j23.5	-14.7	24.9

From Table 4.2, it can be concluded that the lowest level of the phase noise at f_m = 1 kHz from the carrier is achieved when reactance X_{opt} is applied to the feedback of the specified configuration. The optimum output impedance is represented by Z_{out}.

All simulated phase noise spectra are proportional to $1/f_m^3$, similar to the spectrum shown in Figure 4.14c. So in order to determine the optimum configuration, we can easily compare the phase noise level of all obtained spectra at, for example, 1 kHz. From the simulation results presented in Table 4.2, it can be stated that the best phase noise performing basic oscillator is the oscillator which has a common-source configuration with the resonator connected to the gate terminal.

Further, we can optimise the basic oscillator as a function of the last free circuit parameter, the HEMT's gate width. We can simulate the phase noise of the acquired optimum oscillator configuration as function of the gate width. The simulation results of this optimisation step are summarised in Table 4.3.

Table 4.3 Overview of the phase noise simulation results as a function of the HEMT's gate width. Results are related to the common-source capacitive feedback configuration (gate-input).

Gate width [μm]	phase noise at f_m = 1 kHz	X_{opt}	Z_{out} [Ω]	Output power [dBm]	Distortion [%]
50	-109.5 dBc/Hz	C_{opt} = 156 fF	15.5 + j23.5	3.72	42.6
100	-106.6 dBc/Hz	C_{opt} = 261 fF	28.9 + j11.2	3.96	29.8
150	-115.4 dBc/Hz	C_{opt} = 300 fF	31.5 + j16.8	7.94	32.7
200	-106.3 dBc/Hz	C_{opt} = 500 fF	12.5	6.53	10.7

From Table 4.3 it can be concluded that the 150 μm HEMT yields the best phase noise performance although there is only a small difference in performance between the performance of the HEMTs. The optimum configuration has a capacitive feedback of 300 fF and an output impedance of 31.5 + j16.8 Ω at f_0 = 20 GHz.

Consequently, we can consider the performance of the other two design criteria, namely the distortion and the output power of the best phase noise performing oscillator configuration. From simulations we can acquire the values of the distortion and the output power of D = 42.6% and P_{out} = 3.72 dBm, respectively. However, in telecommunication systems such amounts of distortion in oscillators are unacceptable. Therefore, in order to improve the overall performance of the oscillator, we have decided to extend the oscillator circuit with a buffer amplifier. The design of the buffer amplifier is discussed in section 4.6.

4.5.3 Stability

In conformity with the stability analysis presented in section 4.4.3 we can compare the loci of the reflection coefficient of the resonant circuit Γ_R and the inverse reflection

coefficient Γ_A^{-1} of the HEMT on the Smith chart. The loci of the optimised basic oscillator configuration with a gate width of 50 and 150 µm are presented in Figure 4.15.

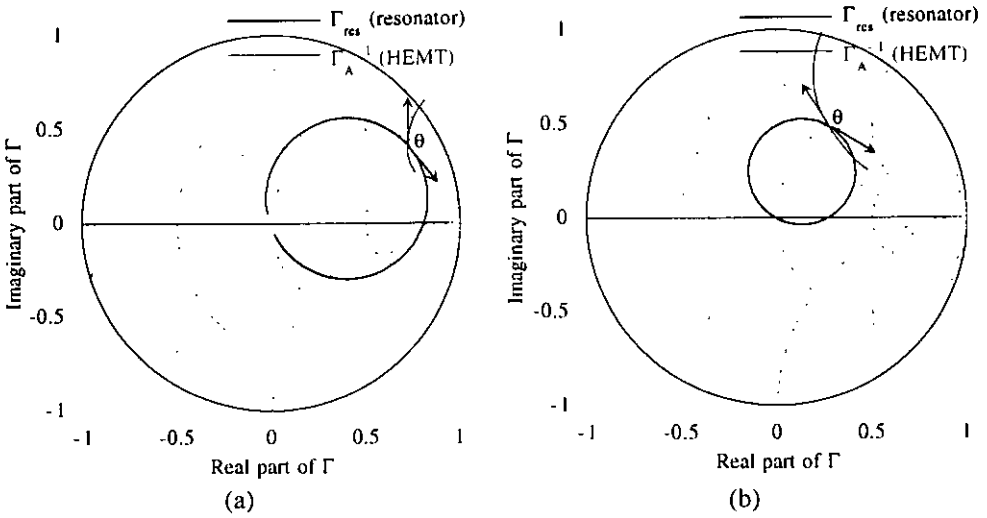

Figure 4.15 Loci of the reflection coefficients of the resonant circuit Γ_R and the HEMT Γ_A^{-1}. The loci are related to the optimised common-source HEMT configuration with a gate width of (a) 50 µm and (b) 150 µm.

As shown in Figure 4.15, the angle between both loci at the interception point is 142° for the 50 µm and 143° for the 150 µm configuration, thus both oscillator configurations are stable.

From Figure 4.15 it is clear that the circuit and inverse device reflection coefficient loci do not intersect in a perfect orthogonal manner. Consequently, from the noise analysis presented in section 4.4.4 it follows that the phase noise performance can be improved by finding another oscillator configuration that has perfect orthogonal loci. However, the presented analysis does not state that there always is a configuration that has perfect orthogonal circuit and inverse device reflection coefficient loci.

Since we elaborately optimised the oscillator configuration by structurally varying the value of the feedback capacitance, the output impedance and the HEMT's gate width, we have considered over 25000 possible configurations for the basic oscillator only. From this, we may assume that we have obtained the configuration that yields the best phase noise performing basic oscillator.

4.6 Design of the buffer amplifier

In section 4.5 we have discussed the design of the basic oscillator. Since the overall performance of the basic oscillator in terms of output power and distortion is not satisfactory we have decided to extend the oscillator circuit with a buffer amplifier. In the design of the buffer we will consider, amongst others, reactive filters in order to suppress the higher harmonics which will yield a lower distortion rate. The additional signal power loss due to the non-ideal behaviour of the circuit elements in the reactive filters can be compensated by introducing a second HEMT that amplifies the output signal in the oscillator circuit. Introducing a buffer amplifier between the basic oscillator and the load impedance Z_L has the additional advantage that fluctuations in the load impedance have less influence on the oscillating signal. The graphic diagram of the total oscillator circuit is shown in Figure 4.16.

As shown in Figure 4.16, two extra building-blocks have been added to the total oscillator circuit, namely an interstage matching network and an output matching network. The former is used to accomplish the optimised output impedance Z_{out} for the basic

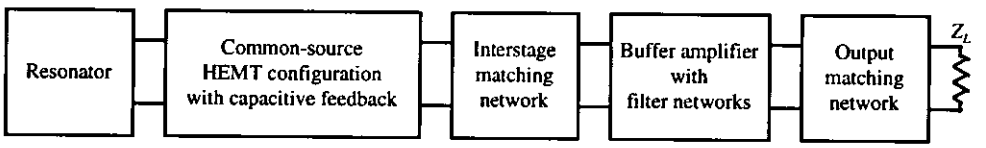

Figure 4.16 Graphic diagram of the total oscillator circuit.

oscillator; the latter is applied in order to achieve maximum output power. Impedance matching is discussed in section 4.6.5.

4.6.1 Stability considerations

To design an amplifier, it is important to avoid oscillation. The stability of an amplifier is an important design consideration. Stability depends on the S-parameters of the transistor, the matching networks and the terminations. For the amplifier shown in Figure 4.17 the circuit is said to be unconditionally stable if the real parts of the impedances Z_{in} and Z_{out} are greater than zero for all passive load and source impedances at any frequency. The circuit is potentially unstable if the real parts of Z_{in} or Z_{out} are negative for some passive load and source impedances at some frequency.

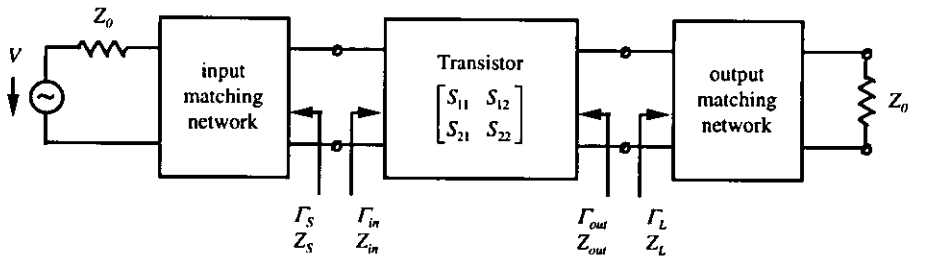

Figure 4.17 Transistor amplifier circuit.

The conditions for unconditional stability of a two-port in general can be written in terms of reflection coefficients as

$$\begin{aligned} &|S_{11}| < 1 \\ &|S_{22}| < 1 \\ &K = \frac{1 - |S_{11}|^2 - |S_{22}|^2 + |S_{11}S_{22} - S_{12}S_{21}|^2}{2 \cdot |S_{12}S_{21}|} > 1 \end{aligned} \tag{4.21}$$

where K is called the inverse of the Linville stability factor. The detailed derivation is summarised in Appendix A.4. Since the oscillator's load impedance Z_L may slightly fluctuate, it is mandatory for the design of the buffer amplifier that the circuit, all filters and matching networks included, is unconditionally stable.

4.6.2 HEMT configuration and gate width

As with the basic oscillator we begin the design of the buffer amplifier by considering the primary function of the circuit, the course of the gain $|S_{21}|$ as function of the variable circuit parameters, like the configuration type and the gate width of the HEMT. The magnitude of the gain can be obtained from simulations as for example shown in Figure 4.18 for the common-source configuration. Analogously to the design of the basic oscillator, we vary the HEMT's configuration and determine the gain $|S_{21}|$ at f = 20 GHz. Consequently, from the obtained results we can select the optimum HEMT configuration of the buffer amplifier. The simulated S-parameters and stability factor K of a HEMT with a

gate width of 150 µm are summarised in Table 4.4. These parameters are presented as a function of the applied configuration at a frequency of f = 20 GHz. The drain and gate bias are the same as for the HEMT used in the basic oscillator, namely 1.0 V and 0.0 V, respectively.

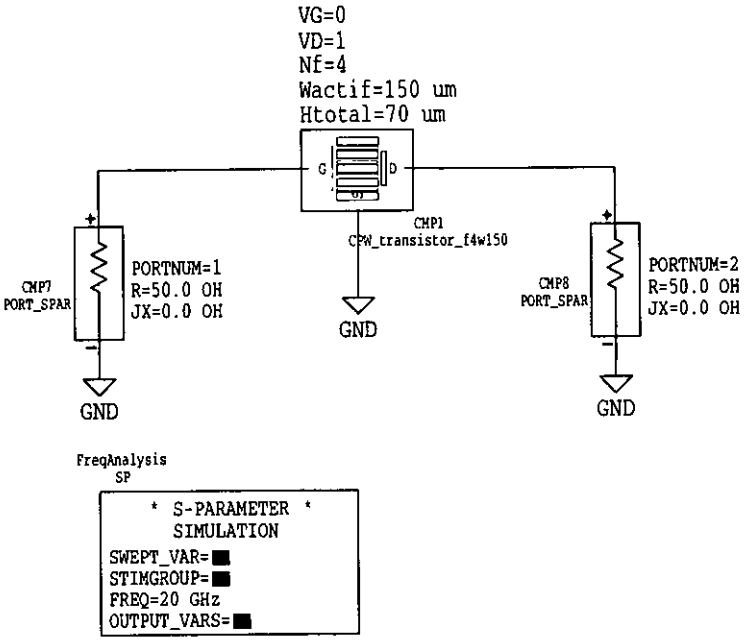

Figure 4.18 S-parameter simulation of the common-source configuration containing a 150 µm HEMT.

Table 4.4 Simulated S-parameters and K factor at a frequency of f = 20 GHz of an InP based HEMT with a gate width 150 µm.

Configuration[1]	S_{11}	S_{12}	S_{21}	S_{22}	K
CS gate-input	1.00 ∠-77.2°	0.07 ∠-176°	5.67 ∠113°	0.43 ∠-38.9°	-0.042
CG source-input	0.48 ∠-176°	0.21 ∠5.82°	1.44 ∠-22.4°	0.87 ∠-29.7°	0.884
CD gate-input	0.98 ∠-36.2°	0.27 ∠54.2°	1.36 ∠-19.8°	0.55 ∠-167°	-0.277

[1] Notation: CS ≡ common-source configuration; gate-input ≡ gate terminal is used for the incoming microwave signal. Other abbreviations have similar meanings.

From Table 4.4 it is clear that the common-source configuration, shown in Figure 4.18, yields the largest gain $|S_{21}|$ at f = 20 GHz. This may be considered as an ordinary result since in section 4.5.1 we already mentioned that common-source configurations are often used for amplifiers.

Similarly, we can determine the S-parameters and stability factor K as a function of the HEMT's gate width at f = 20 GHz. The results are summarised in Table 4.5.

Table 4.5 Simulated S-parameters and K factor at a frequency of f = 20 GHz of an InP based HEMT in a CS (gate-input) configuration with a gate width of 50, 100, 150 and 200 µm, respectively.

Gate width [µm]	S_{11}	S_{12}	S_{21}	S_{22}	K
50	0.98 ∠-41.4°	0.02 ∠-156°	3.33 ∠143°	0.67 ∠-18.6°	-0.204
100	0.95 ∠-78.6°	0.07 ∠38.6°	4.26 ∠129°	0.60 ∠-47.9°	0.026
150	1.00 ∠-77.2°	0.07 ∠-176°	5.67 ∠113°	0.43 ∠-38.9°	-0.042
200	1.02 ∠-136°	0.08 ∠22.3°	4.33 ∠112°	0.35 ∠-150°	-0.044

Since Table 4.4 has shown that the common-source configuration yields the largest gain, it can be concluded from Table 4.5 that this HEMT configuration with a gate width of 150 μm has the largest gain $|S_{21}|$ at $f = 20$ GHz. However, at this point we decide to use the 200 μm HEMT for the design of the buffer amplifier because a 200 μm HEMT has the ability to carry a larger current than a 150 μm HEMT and, consequently, can produce more output power.

From the presented K factors in Table 4.4 or Table 4.5 it is clear that none of the HEMTs are unconditionally stable at $f = 20$ GHz. To achieve this requirement we will have to add passive elements, among which passive filters.

4.6.3 Microwave filters

Theory

A microwave filter is a two-port network used to control the frequency response in a microwave system by providing transmission at frequencies within the passband and attenuation in the stopband of the filter. In the design of the buffer amplifier the filter is introduced to attenuate the higher harmonics so that the distortion of the total oscillator circuit is reduced. In the filter design we only use reactive elements to minimise the power loss of the signal in the passband.

For the design of the filter we apply the insertion loss method [24]. In the insertion loss method a filter response is defined by its insertion loss, or power loss ratio, P_{LR}

$$P_{LR} = \frac{\text{Power available from source}}{\text{Power delivered to load}} = \frac{P_{source}}{P_{load}} = \frac{1}{1-|\Gamma(\omega)|^2} \tag{4.22}$$

where $\Gamma(\omega)$ is the reflection coefficient of the filter. The function $|\Gamma(\omega)|^2$ is an even function of ω. Therefore, it can be expressed as a polynomial in ω^2, so we can write [24]

$$|\Gamma(\omega)|^2 = \frac{M(\omega^2)}{M(\omega^2)+N(\omega^2)} \tag{4.23}$$

where $M(\omega)$ and $N(\omega)$ are real polynomials in ω^2. Substituting this form in (4.22) gives the following

$$P_{LR} = 1+\frac{M(\omega^2)}{N(\omega^2)} \tag{4.24}$$

Thus, for a filter to be physically realisable its power loss ratio must be of the form in (4.24).

The filter design discussed in this section aims at the realisation of a low-pass (LP) filter with a maximally flat characteristic in the passband. This characteristic is also called the binomial or Butterworth response and is optimum in the sense that it provides the flattest possible passband response for a given filter complexity or order. For a LP filter, it is specified by

$$P_{LR} = 1+\left(\frac{\omega}{\omega_c}\right)^{2N} \tag{4.25}$$

where N is the order of the filter, i.e. the number of reactive elements, and ω_c the cut-off frequency. For a given cut-off frequency ω_c and filter network, as for example given in Figure 4.19a, we can calculate the power loss ratio by applying (4.22) and (4.25).

In principle, this procedure can be extended to find the element values for filters with an arbitrary number of elements N, but clearly this is not practical for large N. For a normalised

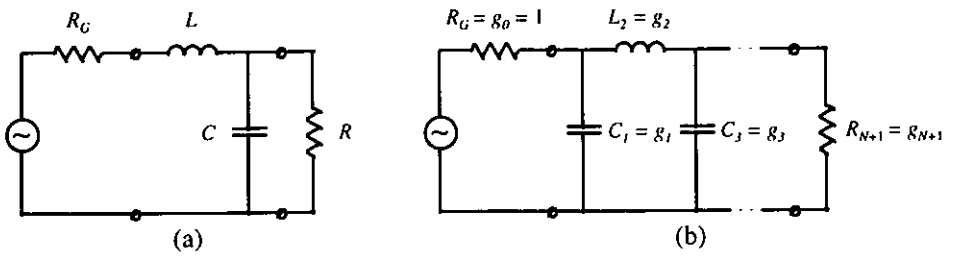

Figure 4.19 (a) Low-pass filter prototype, $N = 2$.
(b) Ladder circuits for LP filter prototypes and their element definitions.

LP filter design where the source impedance is 1 Ω and the cut-off frequency is ω_c = 1 Hz, however, the element values for the ladder-type circuits shown in Figure 4.19b can be tabulated [25]. In Figure 4.19b, the generator resistance is represented by g_0, g_k is the inductance for series inductors or capacitance for shunt capacitors for $1 < k < N$ and g_{N+1} is the load resistance if g_N is a shunt capacitor.

After the normalised filter design has been completed it can be scaled in terms of impedance and frequency. The scaling rules for these filter transformations are described in [24].

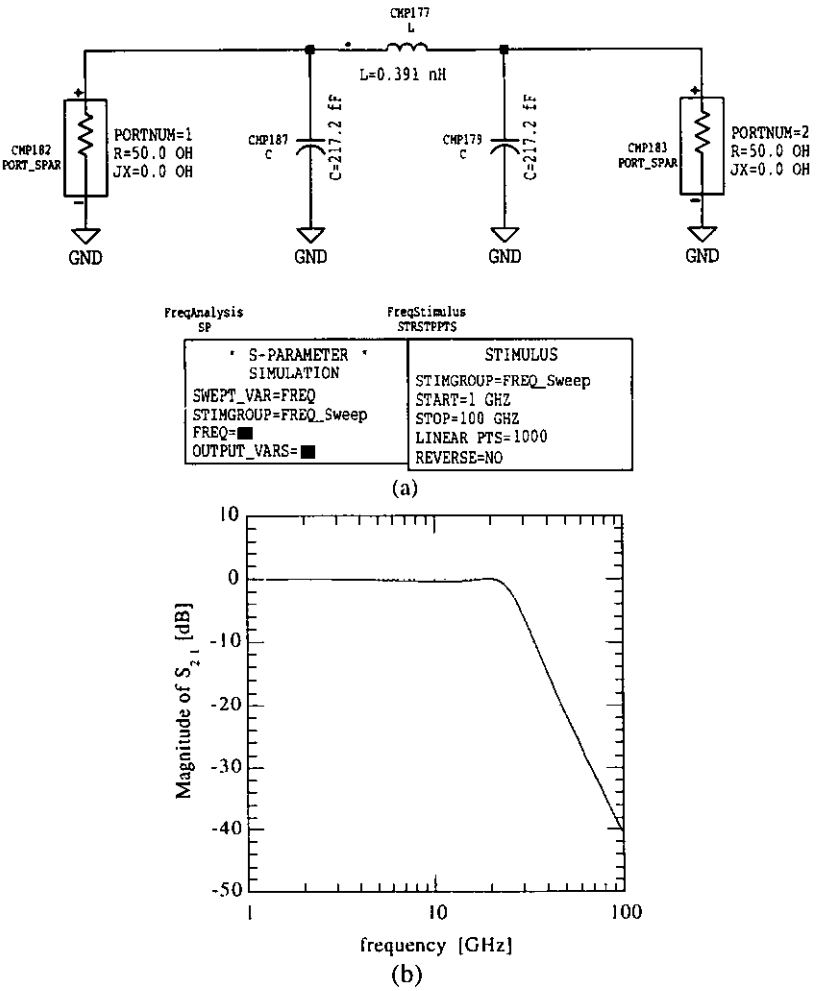

Figure 4.20 (a) Low-pass 3rd order filter design.
(b) Simulation results of the filter design.

Design

In order to minimise the power loss in the signal it is of importance to restrict the number of reactances, i.e. the order of the filter. Therefore, we decide to consider only a 3rd and a 5th order filter in the design of the buffer amplifier. In conformity with the theory described in this section we can design a 3rd order LP filter. The design as well as the gain $|S_{21}|$ (< 1) is shown in Figure 4.20.

Similarly, the design of the 5th order LP filter can be performed. Design and simulation results are shown in Figure 4.21.

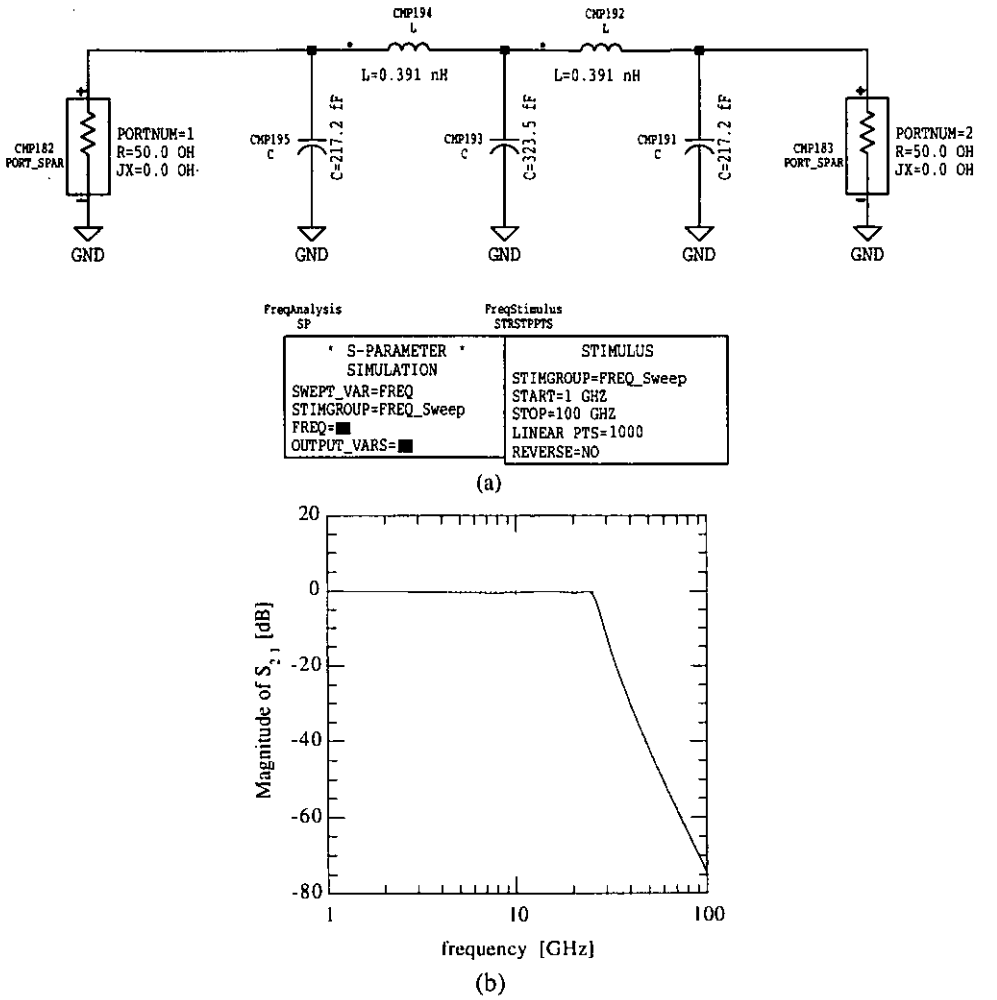

Figure 4.21 (a) Low-pass 5th order filter design.
(b) Simulation results of the filter design.

4.6.4 Buffer topologies

Using the proposed filters we can compose a number of buffer topologies which can be applied to the basic oscillator in order to improve the overall oscillator performance. The possible compositions are illustrated in Figure 4.22.

In order to optimise the total oscillator circuit we apply each of the buffer topologies shown in Figure 4.22 to the basic oscillators summarised in Table 4.3. From simulation results we can ultimately determine the best performing total oscillator in terms of output power, distortion as well as phase noise. The optimisation of the total oscillator circuit is discussed in section 4.7. Before this optimisation step can be performed we have to

complete the total oscillator circuit by adding two matching networks as discussed earlier in this section.

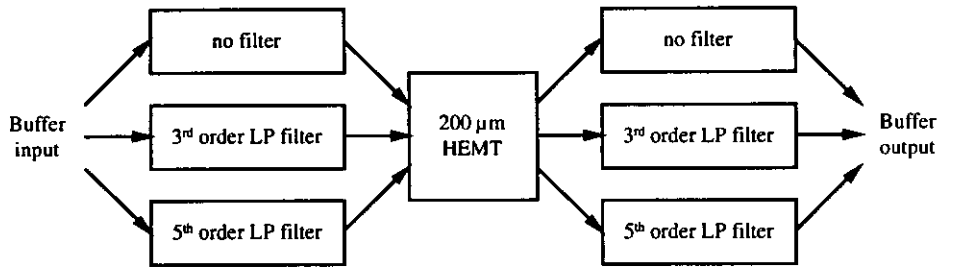

Figure 4.22 Considered buffer amplifier topologies.

4.6.5 Impedance matching

Impedance matching is important in the design of all microwave components, circuits and sub-systems. The basic idea of matching is illustrated in Figure 4.23, which shows an impedance matching network placed between an impedance Z_L and a transmission line. The matching network is ideally lossless, to avoid unnecessary loss of power. The impedance seen, looking into the matching network is the new obtained impedance Z_{in}.

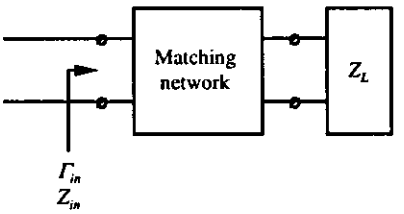

Figure 4.23 Impedance matching network.

In Figure 4.16 we have inserted a matching network between the basic oscillator and the buffer amplifier and between the buffer amplifier and the oscillator's load impedance Z_L. In spite of the topology of the buffer amplifier, it is clear that the input impedance of this circuit has to be matched to the optimised known output impedance Z_{out} of the specific basic oscillator, which has been presented in Table 4.3.

From literature [6] it can be stated that the power gain of the buffer amplifier can be maximised by optimising the input- and output-matching networks. The maximum gain occurs when (see Figure 4.17)

$$\begin{aligned} \Gamma_S &= S_{11}^* = \Gamma_{in}^* \\ \Gamma_L &= S_{22}^* = \Gamma_{out}^* \end{aligned} \tag{4.26}$$

where * denotes the conjugate. However, since the input impedance of the buffer has to be matched to the basic oscillator's optimum impedance we can only match the output impedance Z_L to (4.26).

At $f = 20$ GHz lumped elements (L, C) can be used effectively to accomplish impedance matching. Other ways to match a load impedance is to use a single-stub network or a quarter-wavelength transformer. The disadvantage, however, of these alternatives is that the dimensions of these matching networks are very large (in the order of millimetres). Therefore, in the design of matching networks we will use lumped elements.

Many combinations of LC circuits can be used to match Z_L to Z_{in}. The design of the passive matching network can be carried out by using the Smith chart. The procedure of impedance matching by using a Smith chart will be discussed briefly hereafter.

In the Z (impedance) Smith chart, adding a series reactance to a load produces motion along a constant-resistance circle. The constant-resistance circles are the dashed circles in

Figure 4.24a which are centred on the horizontal line in the Smith chart where the impedance contains only a real part. As shown in Figure 4.24a, if the series reactance is an inductance, the motion is upward since the total reactance is increased. If it is a capacitance, the motion is downward.

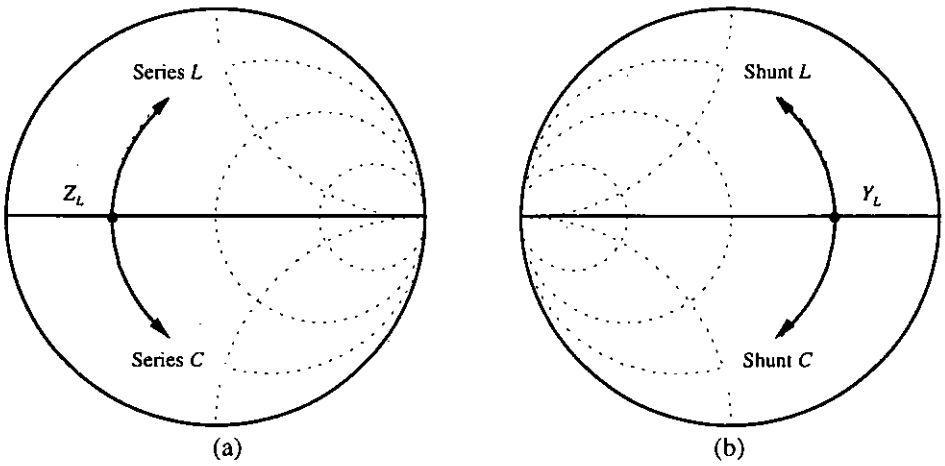

Figure 4.24 Using the Smith chart for impedance matching. (a) Motion on the Z Smith chart due to adding a series reactance to the load. (b) Motion on the rotated Y Smith chart due to adding a parallel reactance to the load.

Similarly, adding a shunt reactance to a load produces a motion along a constant-conductance circle in the rotated Y (conductance) Smith chart. The constant-conductance circles are the dashed circles in Figure 4.24b which are also centred on the horizontal line in the Smith chart. As shown in Figure 4.24b, if the shunt element is an inductor, the motion is upward. If the shunt element is a capacitor, the motion is downward. Using a combination of constant-resistance and constant-conductance circles, one can move the load impedance Z_L to any specific input impedance Z_{in}.

Example

In Figure 4.25a both the Z and Y Smith charts are shown. If we would like to match the load impedance $Z_L = 10 + j10\ \Omega$ to a 50 Ω line at 500 MHz we can accomplish this using the LC network shown in Figure 4.25b.

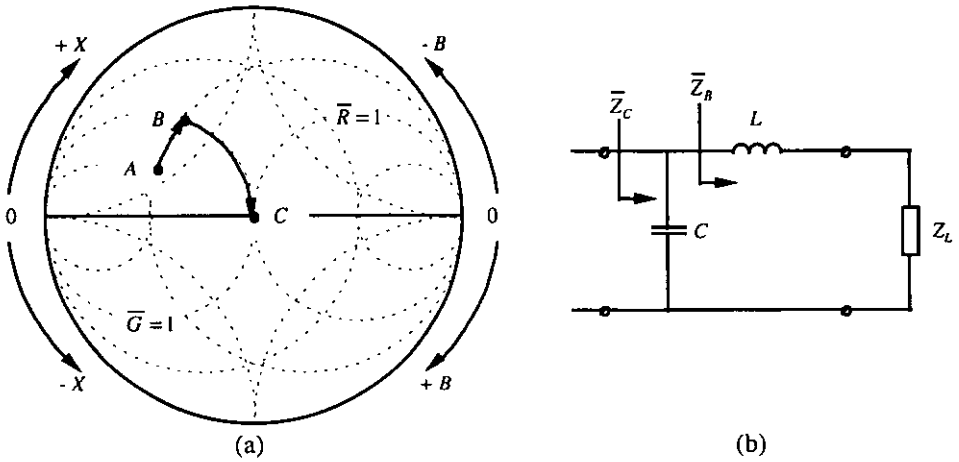

Figure 4.25 Using a series L and a shunt C to match Z_L to Z_0. (a) Combined Z-Y Smith chart. (b) LC network to accomplish the matching.

Since on the Smith chart only normalised impedances or conductances are used we normalise the load impedance Z_L and plot it on the Smith chart in Figure 4.25a yielding point A

$$\overline{Z}_L = \frac{Z_L}{Z_0} = 0.2 + j0.2$$

Next, we move A to B along the constant-resistance circle. B is located on the constant-conductance circle passing through the centre, i.e. $\overline{G} = 1$ circle. This movement can be achieved by adding a series inductance to the load impedance Z_L as shown in Figure 4.25b. The value of the inductance can be derived from the location of point B on the Z-Y Smith chart as shown in Figure 4.25a

$$\begin{aligned} j\omega L &= Z_0\left(j\overline{X}_B - j\overline{X}_L\right) \\ &= 50\cdot(j0.4 - j0.2) \\ \omega L &= 50\cdot 0.2 = 10 = 2\pi fL = 2\pi\cdot 500\ 10^6\cdot L \\ L &= 3.18\ \text{nH} \end{aligned}$$

Consequently, move from B to C along the $\overline{G} = 1$ circle. C is the centre of the chart representing a 50 Ω impedance. At point C, $\overline{Z}_C = 1$. From points B to C, we use the rotated Y Smith chart and a shunt capacitance as shown in Figures 4.25a and 4.25b, respectively. This yields

$$\begin{aligned} \overline{Y}_C &= 1 \\ \overline{Y}_B &= 1 - j2 \\ j\omega C &= Y_0\left[\text{Im}\left(\overline{Y}_C\right) - \text{Im}\left(\overline{Y}_B\right)\right] \\ &= \frac{1}{50}\cdot\left[0 - (-j2)\right] \\ C &= \frac{1}{25\omega} = \frac{1}{25\cdot 2\pi f} = 12.73\ \text{pF} \end{aligned}$$

Hence, if the calculated values of the inductance and capacitance are applied to the matching network of Figure 4.25b, the input impedance equals 50 Ω.

4.7 Total oscillator circuit

As shown in the graphic diagram of Figure 4.16, the ultimate total oscillator has a topology consisting of primarily a basic oscillator and an interstage matching network followed by a buffer amplifier and an output matching network. Directly connected to the optimised basic oscillator, an interstage matching network is applied in order to match the input impedance of the buffer amplifier to the optimised impedance Z_{out} of the basic oscillator. The output matching network is designed to achieve maximum gain from the amplifier stage. The design of these matching networks is performed according to the procedure described in section 4.6.5.

The last design step to complete the total oscillator concerns the optimisation of the overall performance, i.e. the output power, the distortion and the phase noise performance, as function of the topology of the buffer amplifier. If the basic oscillators summarised in Table 4.3 and the buffer amplifiers illustrated in Figure 4.22 are combined, it follows that we can apply 9 buffer amplifiers to 4 basic oscillators yielding 36 possible total oscillator circuits. In this section, we will present the results of these configurations in order to acquire the final circuit.

Although the microwave oscillator is merely designed to verify the appropriateness of the low-frequency noise model discussed in chapter 3, it is useful, at this point, to draft

some oscillator specifications in order to determine the ultimate oscillator circuit. It is clear that these specifications are, however, somewhat arbitrary but nevertheless necessary for the further design. In this way, we have decided to draw the following demands for the ultimate oscillator circuit

- Output power $P_{out} \geq 10$ dBm
- Distortion $D \leq 5\%$
- Phase noise (at f_m = 1 kHz) ≤ -80 dBm/Hz

After simulating the proposed total oscillator configurations in HP MDS, the results have been summarised in Table 4.6. This table shows the overall oscillator performance as function of the gate width of the HEMT which has been used in the basic oscillator. In Table 4.6 only the configurations have been presented which yield the best oscillator performance. An extensive presentation of the total oscillator performance in terms of output power, distortion and phase noise is presented in Appendix C.

Table 4.6 Simulation results of the total oscillator configurations.

Gate width [μm]	Buffer configuration[1]	Phase noise at f_m = 1 kHz	Output power [dBm]	Distortion [%]
50	× - HEMT - 5th	-89.9 dBc/Hz	8.9	0.91
100	3rd - HEMT - 3rd	-85.9 dBc/Hz	9.6	1.74
150	3rd - HEMT - 3rd	-81.2 dBc/Hz	10.8	2.47
200	5th - HEMT - 5th	-85.7 dBc/Hz	7.2	0.54

[1] Notation: × ≡ no filter; 3rd ≡ third order LP filter; 5th ≡ fifth order LP filter; HEMT ≡ InP based HEMT with a 200 μm gate width. The sequence of the abbreviations agree with the sequence of the applied devices.

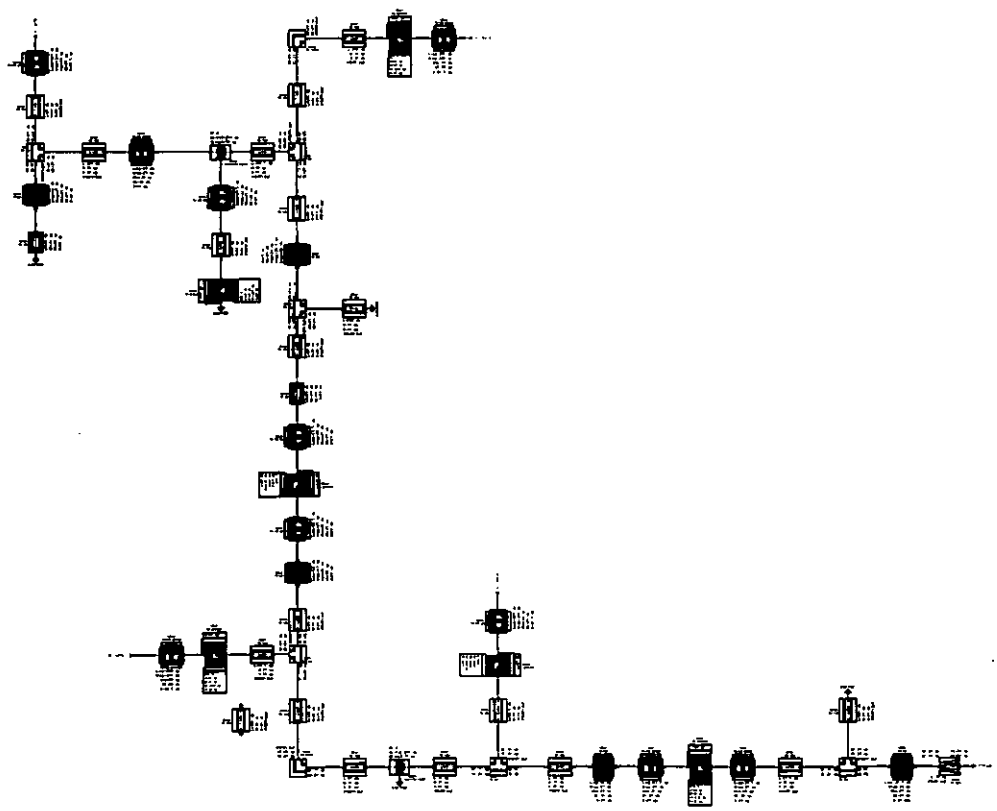

Figure 4.26 Design of the ultimate total oscillator circuit using non-ideal passive elements.

From Table 4.6 it can be concluded that only the configuration containing a 150 µm HEMT in the basic oscillator meets the drawn oscillator specifications. Hence, it can be stated that the ultimate buffer amplifier consists of two 3rd order LP filters and a HEMT with a gate width of 200 µm.

After the design of the total oscillator has been accomplished we can replace the ideal passive elements by their non-ideal equivalents. Besides a more realistic prediction of the oscillator performance, we are able to automatically generate a layout starting from these non-ideal passive elements. In this way, both the layout and microwave characteristics of all passive as well as active elements in a design are linked, which enables a comparison of simulation and measurement results afterwards.

The ultimate total oscillator design containing non-ideal passive elements is presented in Figure 4.26.

4.8 Total oscillator layout

Using the auto-layout function of HP MDS we are able to obtain the basic layout of the total oscillator circuit. The auto-layout function generates the layout of each specific passive and active element of the total design and maps the separate layouts resulting in a basic layout. Consequently, to achieve a complete coplanar layout we have to add the groundplanes to both the passive and active elements. The ultimate result of the total oscillator layout is presented in Figure 4.27.

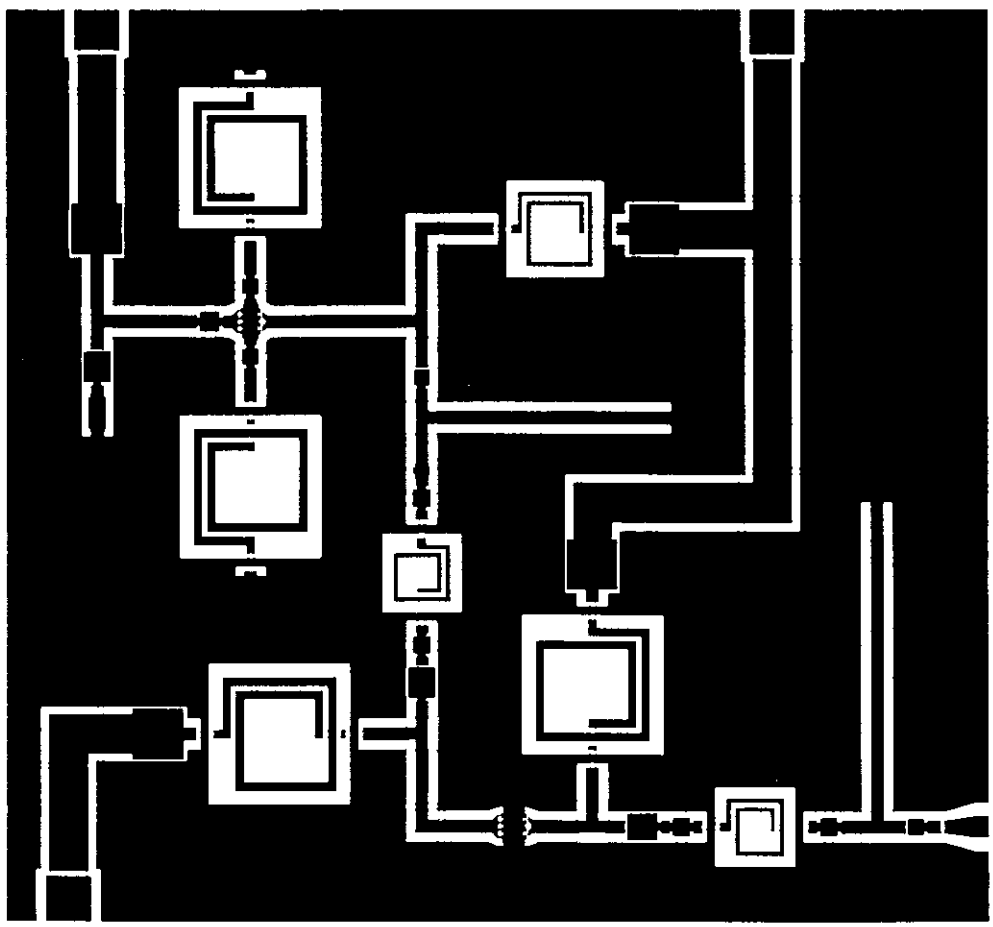

Figure 4.27 Layout of the ultimate total oscillator circuit.

If we consider the layout presented in Figure 4.27 we distinguish narrow (30 µm) and wide (70 µm) transmission lines. The former is meant to carry the HF signal while the latter

is applied in order to bias the two present HEMTs in the circuit. DC biasing is an important design consideration for proper operation of MMICs. The ideal biasing arrangement should select the proper quiescent point and hold the quiescent point constant over variations in transistor parameters and temperature. The DC and HF circuits should be isolated so that no HF signal leaks into the DC biasing circuit and the biasing circuit does not disturb HF performance.

The MMIC presented in Figure 4.27 contains two HEMTs which are biased through a series inductor and capacitor. The impedance of the series inductor and capacitor together has been designed to reach approximately infinity at $f = 20$ GHz. However, if we consider DC it can be concluded that the input impedance is very low which makes the *LC* network to be an excellent bias network.

After the layout of the total oscillator has been completed, the optical masks which form the starting-point of the circuit processing can be fabricated. Using these masks and the in-house InP based HEMT technology the designed oscillator as well as its additional sub-circuits can be realised. Consequently, phase noise measurements can be performed in order to enable comparison with simulated results. The comparison of measurement with simulation results is discussed in chapter 5.

Chapter 5

Results and conclusions

5.1 Results

5.1.1 Introduction

After the design and layout of both the total oscillator and its sub-circuits have been accomplished, the optical masks are fabricated. Consequently, using these masks and the in-house InP based HEMT technology we are able to realise the designed circuits discussed in chapter 4.

In this section we will present the final results of the circuit processing as well as the results of their high-frequency characterisation. S-parameters[1], output power and phase noise spectra[2] are measured and compared to simulation results. To begin with, we will present the results of the sub-circuits followed by, ultimately, the results of the total oscillator circuit.

5.1.2 Lumped element resonator

Since the resonator is the frequency determining element in a microwave oscillator and so an important element, single resonators have been realised. A picture of the lumped element resonator is presented in Figure 5.1a, the measured and simulated reflection coefficient loci are shown in Figure 5.1b.

The length and width of the microwave resonator depicted in Figure 5.1a is 600 and 800 μm, respectively. From Figure 5.1b it can be concluded that the designed and realised resonators have similar shaped characteristics. However, the difference in magnitude of the reflection coefficients is substantial. The magnitude of the measured and simulated reflection coefficients at f = 20 GHz amounts 0.409 and 0.613, respectively

The lower value of the measured reflection coefficient $|S_{11}|$ as shown in Figure 5.1b can be explained by the applied modelling of the T-junction present in the resonator circuit. This junction forms a parasitic capacitance to ground with $\varepsilon_r = 1$. In HP MDS, however, this junction is modelled by connecting three coplanar transmission lines neglecting this parasitic effect. Since this capacitance is connected parallel to the resonator's resistance, only a part of the HF signal reflects from the resonator, resulting in a lower reflection coefficient. As follows from the presented loci in Figure 5.1b, the simplified T-junction model loses its validity at a frequency of f_0 = 20 GHz. Consequently, a different resonator characteristic will have consequences for the oscillation frequency and amplitude of the

---

[1] The S-parameter measurements have been performed at the section 'Telecommunications and Microwaves' of the department of electrical engineering 'ESAT' of the K.U. Leuven.

[2] The output power and phase noise measurements have been performed at the 'Institut für Mobil- und Satellitenfunktechnik', Kamp-Lintfort.

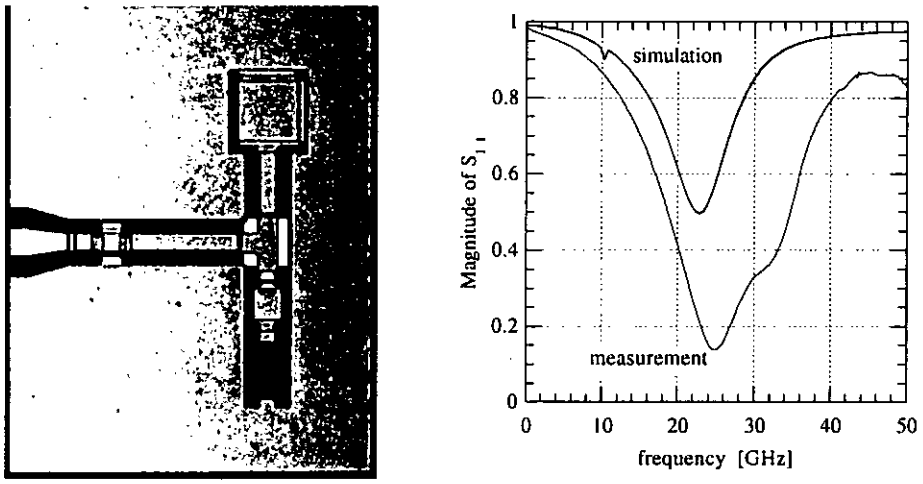

(a) (b)

Figure 5.1 (a) Picture of the lumped element resonator used in the total oscillator.
(b) Magnitude of the measured and simulated reflection coefficient.

basic oscillator as well as the total oscillator circuit.

The Q factors of the simulated and measured spectra shown in Figure 5.1b are about equal and have approximately a value of 10.

5.1.3 Microwave low-pass filter

The designed microwave low-pass (LP) filter which is applied in the buffer amplifier is supposed to provide transmission at frequencies within the passband, i.e. up to $f = 20$ GHz and attenuation in the stopband, i.e. $f > 20$ GHz. A picture of the filter section is shown in Figure 5.2a. As shown, the filter is processed separately from the oscillator circuit in order to enable its characterisation. The measured and simulated gain $|S_{21}|$ (< 1) is shown in Figure 5.2b.

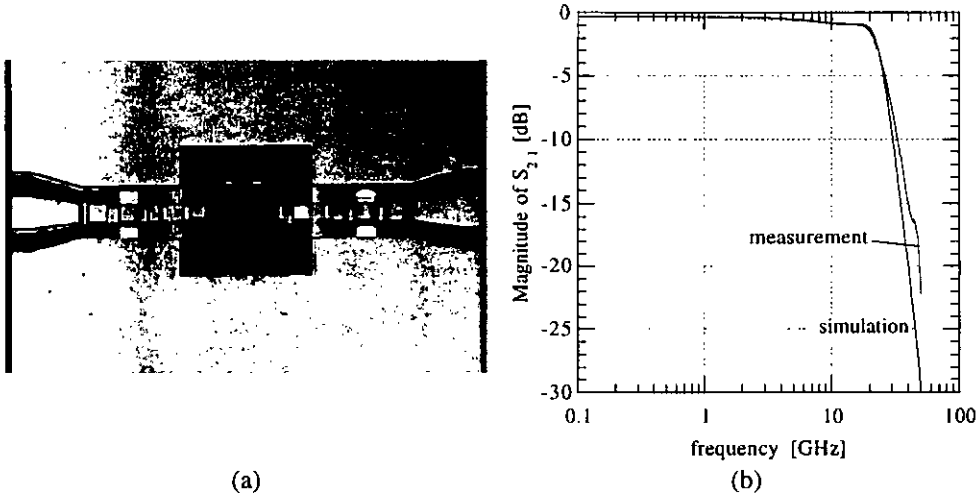

(a) (b)

Figure 5.2 (a) Picture of the microwave LP filter used in the total oscillator.
(b) Measured and simulated gain $|S_{21}|$.

The length and width of the LP filter depicted in Figure 5.2a amounts 669 and 500 µm, respectively. The measured gain $|S_{21}|$ as presented in Figure 5.2b, shows good agreement with the simulation results. At $f = 20$ GHz the measured and simulated values of $|S_{21}|$ are

−1.58 and −1.37 dB, respectively. At f = 40 GHz, i.e. at the first harmonic frequency, the values of the measured and simulated values of $|S_{21}|$ are −14.8 and −20.5 dB, respectively.

5.1.4 Basic oscillator

As discussed in chapter 4, the basic oscillator is an assembly consisting of a microwave resonator, a negative resistance element, the HEMT, and an output matching network. The presented picture of the basic resonator in Figure 5.3a is a sub-circuit of the total oscillator described in chapter 4. Figure 5.3b shows the output power spectrum of the basic oscillator.

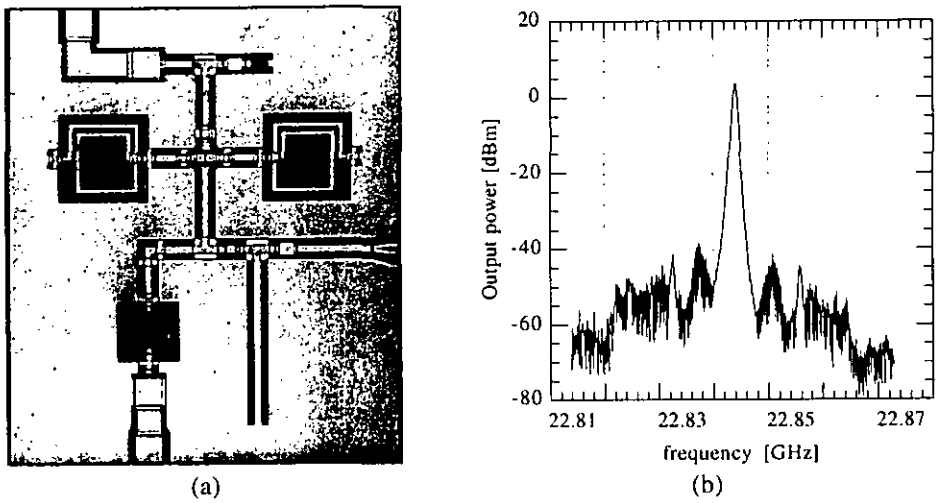

Figure 5.3 (a) Picture of the basic oscillator.
(b) Measured output power spectrum.

From Figure 5.3b it can be concluded that the basic oscillator operates at a frequency of approximately f = 22.844 GHz producing an output power of P_{out} = 3.51 dBm. The length and width of the basic oscillator depicted in Figure 5.3a amounts 1.44 and 1.69 mm, respectively.

Since the basic oscillator consists of only a few passive elements and just one single HEMT, this circuit is ideally usable for phase noise characterisation. The measurement as well as the simulation results of the phase noise are shown in Figure 5.4.

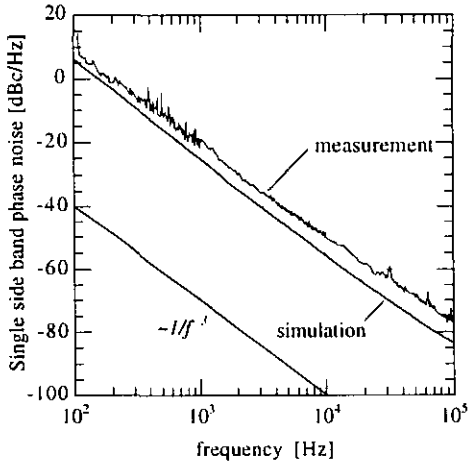

Figure 5.4 Measured and simulated phase noise spectra.

From Figure 5.4 it follows that the single side band (SSB) phase noise of the realised as well as of the designed basic oscillator is proportional to $1/f_m^3$. The magnitude of the measured and simulated phase noise spectra at f_m = 100 kHz from the carrier are –77.14 and –83.6 dBc/Hz, respectively. The simulated phase noise spectrum presented in Figure 5.4 shows that the low-frequency noise model has been implemented correctly using a measurement based approach as discussed in chapter 3.

The measurement results of the SSB phase noise of the realised basic oscillator can be compared with results reported in literature in order to obtain an impression of the oscillator's phase noise performance. A comparison of measured phase noise spectra reported in literature at f_m = 100 kHz from the carrier is presented in Figure 5.5.

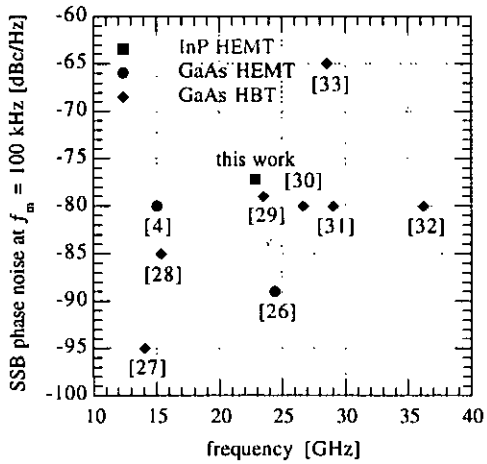

Figure 5.5 Comparison of measured single sideband (SSB) phase noise spectra at 100 kHz from the carrier in this work and reported in literature.

From Figure 5.5 it can be concluded that the phase noise performance of the realised basic oscillator is comparable to reported results on GaAs based HEMT [4], [26] and HBT oscillators [27]-[33] in the same frequency range, which underlines the important potential of InP based HEMTs in non-linear applications.

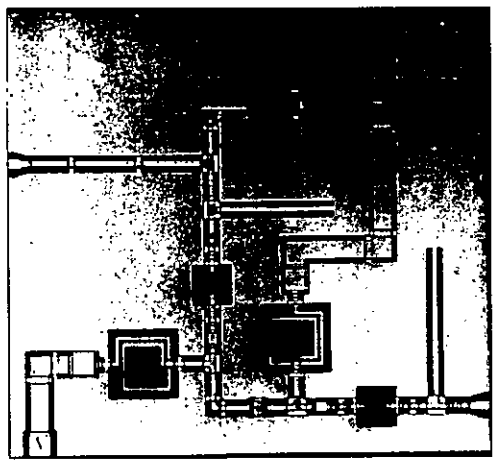

(a)

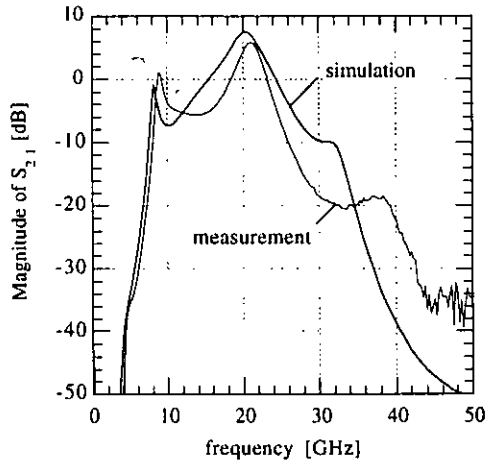

(b)

Figure 5.6 (a) Picture of the buffer amplifier.
(b) Measured and simulated gain $|S_{21}|$.

5.1.5 Buffer amplifier

The buffer amplifier increases the fundamental of the basic oscillator and suppresses the higher harmonics. A picture of the buffer amplifier as well as the measured and simulated gain $|S_{21}|$ is shown in Figure 5.6.

The length and width of the buffer amplifier depicted in Figure 5.6a amounts 2.23 and 2.08 mm, respectively. The buffer circuit amplifies around $f \approx 20$ GHz and attenuates outside this frequency band as is shown in Figure 5.6b. The measured gain $|S_{21}|$ presented in Figure 5.6b shows a maximum amplification of 5.81 dB at $f = 21.0$ GHz. The maximum simulated gain is 7.62 dB at $f = 20.2$ GHz.

5.1.6 Total oscillator

Finally, the picture of the ultimately realised circuit of the total oscillator is presented in Figure 5.7.

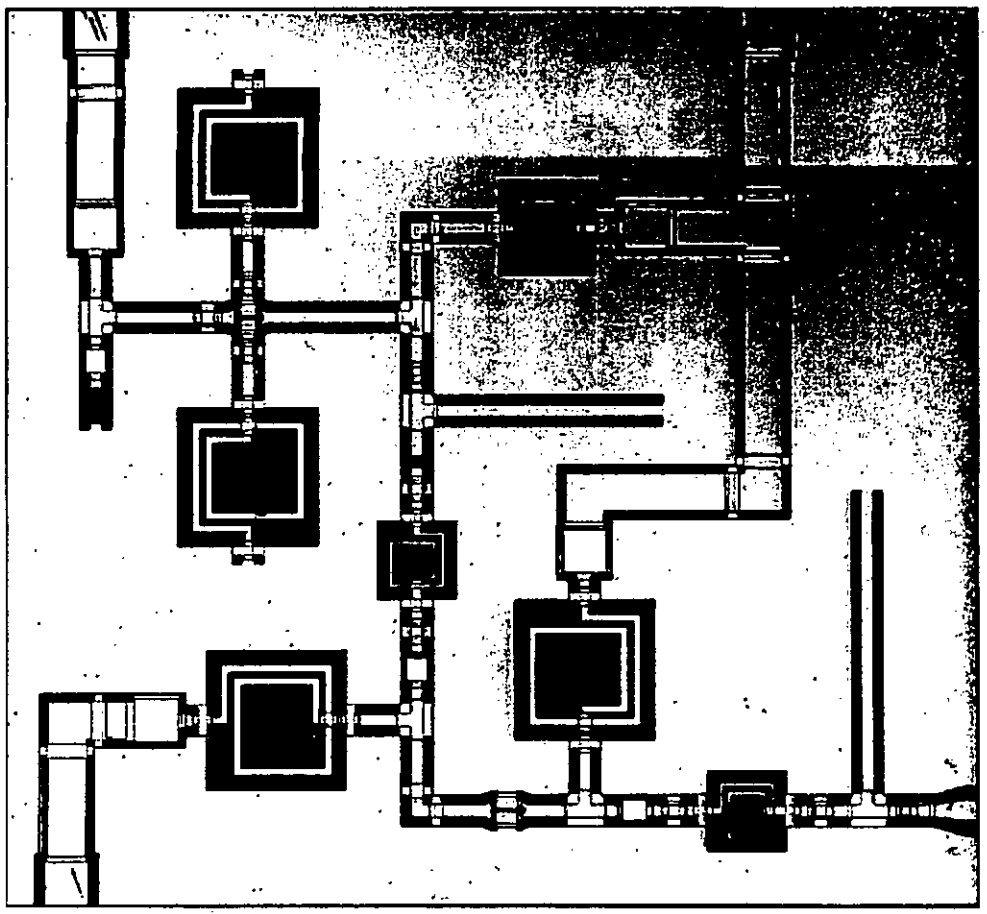

Figure 5.7 Picture of the total oscillator.

The length and width of the total oscillator circuit depicted in Figure 5.7 is 2.23 and 2.08 mm, respectively. Up to this point, all sub-circuits have shown to produce good functionality. In case of the total oscillator circuit, however, no oscillating signal was measured at the HF output of the circuit.

This non-functioning can be explained by the characteristic of the microwave resonator presented in Figure 5.1b. This characteristic deviates substantially from its designed characteristic as we noticed in section 5.1.2. In spite of this deviation the basic oscillator still functioned at a frequency of f_0 = 22.844 GHz. In case of the total oscillator, this resonator may be the reason that keeps the circuit from oscillation. Hence, it can be

concluded that the total oscillator circuit is more sensitive for deviations in its microwave resonator than the basic oscillator. Fortunately, due to the robustness of the basic circuit, oscillator phase noise has been measured resulting in a valid verification of the implemented low-frequency noise model in HP MDS as described in chapter 3.

5.2 Conclusions

5.2.1 Modelling of low-frequency noise in InP based HEMTs

In literature, the origin of the low-frequency noise in InP based HEMTs has been reported. This analysis which has been briefly presented in chapter 3 yields an expression for the drain current noise which is, however, only valid in the ohmic region. Since we intend to model the low-frequency noise in the ohmic as well as in the saturation region and for various gate voltages, this analysis has shown to be inadequate for our noise modelling. Therefore, noise measurements have been performed in order to obtain a measurement-based model which has validity in both the ohmic and saturation regions.

The acquired low-frequency noise spectra have been discussed and compared to results reported in literature. Compared to the GaAs based HEMT the InP based HEMT has demonstrated to have a better low-frequency noise performance. Although the magnitude of the gate current noise in both HEMTs is about equal, the noise in the drain current of the InP based HEMT produces almost 3 decades less noise than the GaAs based HEMT. All performed low-frequency drain and gate current noise measurements on InP based HEMTs produced merely $1/f$-like spectra, i.e. no significant g-r noise was observed.

In conventional AlGaAs/GaAs based HEMTs g-r noise has been observed due to the presence of a parallel MESFET between the surface and the channel which occurs at large gate bias. Although the Si δ-doping in the doping layer of the InP based HEMT gives rise to many trapping and de-trapping centres, no g-r noise has been measured. This can be explained due to the better electron confinement of the InP based HEMT.

Consequently, the coherence or correlation between the low-frequency drain and gate noise sources has been measured. The measured low value of the coherence shows that these noise sources can be treated separately which facilitates the noise modelling considerably. In this way, the low-frequency noise can be modelled by introducing a spectral noise current source at the drain-side parallel to the intrinsic current source and at the gate-side parallel to the gate and the source terminals. As with the g-r noise, the low value of the coherence can also be explained by the electron confinement of the InP based HEMT which prevents the electrons in the channel from interaction with the gate current.

Finally, we have implemented the measured low-frequency noise spectra in the present non-linear HEMT model in HP MDS resulting in a measurement based model that can be used, amongst others, to predict the phase noise performance of non-linear circuits.

5.2.2 Design and layout of a 20 GHz MMIC oscillator

In chapter 4 we have presented several possibilities in designing a microwave oscillator. Starting from these possibilities, a well-considered selection has to be made: a transmission or a reflection form of oscillator, the type of resonator and the ultimate topology of each sub-circuit.

Using HP MDS we have been able to optimise the basic oscillator. From over 25000 possible oscillator entries we picked the best performing oscillator in terms of phase noise performance. Since the distortion as well as the output power of the basic oscillator has shown to be unsatisfactory, we have decided to extend the basic oscillator with a buffer amplifier. Microwave low-pass filters have been applied to suppress the higher harmonics; an extra HEMT has been introduced in order to amplify the oscillating signal. Concerning the buffer amplifier, we have considered over 100 possible entries.

Consequently, combining both the basic oscillator and buffer amplifier has resulted in the total oscillator circuit. We optimised the total circuit in terms of output power, distortion

and phase noise. The simulation results of the ultimate total oscillator circuit has indicated an output power of P_{out} = 10.8 dBm, a distortion level of D = 2.47% and a phase noise level of $\pounds(f_m)$ = -81.2 dBc/Hz at f_m = 100 kHz from the carrier.

Finally, we have accomplished the layout of not only the ultimate oscillator circuit, but also its sub-circuits in order to enable verification of every single compound in the design afterwards. From these layouts, the optical masks can be fabricated which are mandatory for the start of the oscillator processing.

5.2.3 Final remarks

From the results presented in this chapter it can be concluded that all realised sub-circuits have shown characteristics which are in good agreement with the simulated characteristics. Although the total oscillator did not function, we have still been able to characterise the phase noise of the basic oscillator properly. Comparing the phase noise spectra yields a measured phase noise value of –77.1 dBc/Hz versus a simulated phase noise value of –83.6 dBc/Hz at f_m = 100 kHz from the carrier. The magnitude of the measured phase noise of the basic oscillator is comparable with reported results on GaAs based HEMT and HBT oscillators in the same frequency range. Although the InP based HEMT has demonstrated to have better low-frequency noise performance than the GaAs based HEMT, the phase noise behaviour of these compound based oscillators has shown to be of a similar extent. This indicates that the up-conversion factor of the low-frequency noise in the active device of the InP based HEMT oscillator is not equal to the GaAs based HEMT and HBT oscillator.

Finally, the acquired phase noise results demonstrate the correct modelling and implementation of the low-frequency noise model in the simulator section of HP Microwave Design System. Using this model one is able to predict the phase noise behaviour of any non-linear circuit fabricated in IMEC's MMIC technology, which has been the main objective of this research work.

Reference List

[1] Siweris, H.J. and B. Schiek,
ANALYSIS OF NOISE UPCONVERSION IN MICROWAVE FET OSCILLATORS.
IEEE Trans. Microwave Theory and Techn., Vol. MTT-33 (1985), No. 3, p. 233-241.

[2] Kurokawa, K.
SOME BASIC CHARACTERISTICS OF BROADBAND NEGATIVE RESISTANCE OSCILLATOR CIRCUITS.
Bell. Sys. Tech. J., Vol. 48 (1969), p. 1937-1955.

[3] Leeson, D.B.
A SIMPLE MODEL OF FEEDBACK OSCILLATOR NOISE SPECTRUM.
Proc. IEEE, Vol. 54 (1966), No. 2, p. 329-330.

[4] Felgentreff, T. and G.R. Olbrich,
MODELING OF LOW FREQUENCY NOISE SOURCES IN HEMTS.
IEEE MTT-S, Vol. 3 (1996), p. 1743-1746.

[5] Robertson, I.D., ed.
MMIC DESIGN.
London: IEE, 1995. Chapter 9.

[6] Chang, K.
MICROWAVE SOLID-STATE CIRCUITS AND APPLICATIONS.
Chichester: Wiley-Interscience, 1994. Chapters 2, 14 and 15.

[7] Dingle, R. and H. Stormer, A.C. Gossard, W. Wiegamann,
ELECTRON MOBILITIES IN MODULATION DOPED SEMICONDUCTOR HETEROJUNCTION SUPERLATTICES.
Appl. Phys. Lett., Vol. 33 (1978), No. 7, p. 665-667.

[8] Nguyen, L.D. and L.E. Larson, U.K. Mishra,
ULTRA-HIGH-SPEED MODULATION-DOPED FIELD-EFFECT TRANSISTORS: A TUTORIAL REVIEW.
Proc. IEEE, Vol. 80 (1992), No. 4, p. 494-518.

[9] Baeyens, Y.
MONOLITHIC MICROWAVE INTEGRATED CIRCUITS USING GAAS AND INP BASED HETEROJUNCTION FIELD-EFFECT TRANSISTORS.
Ph.D. thesis, Katholieke Universiteit Leuven (Belgium), 1997. Chapters 2 and 3.

[10] Kleinpenning, T.G.M.
SIGNAAL-RUISVERHOUDING IN BOUWSTENEN.
Eindhoven University of Technology, Faculty of Electrical Engineering, 1985.
Lecture notes No. 5642.

[11] Markus, H.
LOW-FREQUENCY NOISE IN MODERN SEMICONDUCTOR TRANSISTORS.
Ph.D. thesis, Eindhoven University of Technology, 1997. Chapter 5.

[12] Kingston, R.H. and E. Burstein, eds.
SEMICONDUCTOR SURFACE PHYSICS.
S.l.: University of Pennsylvania Press, 1957.

[13] Peransin, J.-M. and P. Vignaud, D. Rigaud, L.K.J. Vandamme,
1/F NOISE IN MODFET'S AT LOW DRAIN BIAS.
IEEE Trans. Electron Devices, Vol. 37 (1990), No. 10.

[14] Viktorovitch, P. and P. Rojo-Romeo, J.L. Leclercq, X. Letartre, Jacques Tardy, M. Oustic, M. Gendry,
LOW-FREQUENCY NOISE SOURCES IN INALAS/INGAAS MODFET'S.
IEEE Trans. Electron Devices, Vol. 43 (1996), No. 12, p. 2085-2100.

[15] Sze, S.M.
PHYSICS OF SEMICONDUCTOR DEVICES.
Chichester: Wiley-Interscience, 1981 (2nd edition). Chapter 6.

[16] Kleinpenning, T.G.M.
ON LOW-FREQUENCY NOISE IN TUNNEL DIODES.
Solid-State Electronics, Vol. 21 (1978), p. 927.

[17] Kleinpenning, T.G.M.
ON LOW-FREQUENCY NOISE IN TUNNEL DIODES.
Solid-State Electronics, Vol. 25 (1982), p. 79.

[18] Kumar, V. and W.E. Dahlke,
LOW-FREQUENCY NOISE IN CR-SiO_2-N-SI TUNNEL DIODES.
IEEE Trans. Electron Devices, Vol. 24 (1977), p. 146.

[19] Meva'a, C. and X. Letartre, P. Rojo-Romeo, P. Viktorovitch,
LOW TEMPERATURE MBE GROWN ALINAS: INVESTIGATION OF CURRENT VOLTAGE AND LOW FREQUENCY NOISE BEHAVIOUR OF SCHOTTKY DIODES.
Solid-State Electronics, Vol. 41 (1997), No. 6, p. 857-864.

[20] Vandamme, L.K.J. and D. Rigaud, J.-M. Peransin,
COHERENCE BETWEEN GATE- AND DRAIN-CURRENT FLUCTUATIONS IN MESFET'S AND MODFET'S BIASED IN THE OHMIC REGION.
IEEE Trans. Electron Devices, Vol. 39 (1992), No. 10, p. 2377-2382.

[21] Schreurs, D.
MEASUREMENT BASED MODELLING OF HETEROJUNCTION FIELD-EFFECT DEVICES FOR NON-LINEAR MICROWAVE CIRCUIT DESIGN.
Ph.D thesis, Katholieke Universiteit Leuven (Belgium), 1997.

[22] Kajfez D. and P. Guillon,
DIELECTRIC RESONATORS.
Dedham: Artech House, 1986. Chapters 2 and 10.

[23] Holzman, E. and R. Robertson,
SOLID-STATE MICROWAVE POWER OSCILLATOR DESIGN.
London: Artech House, 1992. Chapter 3.

[24] Pozar, D.M.
MICROWAVE ENGINEERING.
Amsterdam: Addison-Wesley, 1990. Chapters 6 and 9.

[25] Matthaei, G.L. and L. Young, E.M.T. Jones,
MICROWAVE FILTERS, IMPEDANCE-MATCHING NETWORKS, AND COUPLING STRUCTURES.
Dedham: Artech House, 1980.

[26] Ahdjoudj, M. and A. Boudiaf, P. Pouvil,
DESIGN OF LOW PHASE NOISE MMIC PHEMT BASED VCO.
In: Proc. Int. IEEE Workshop on Experimentally Based FET Device Modelling & Related Nonlinear Circuit Design, 1997. P. 25.1-25.5.

[27] Güngerich, V. and F. Zinkler, W. Anzill, P. Russer,
NOISE CALCULATIONS AND EXPERIMENTAL RESULTS OF VARACTOR TUNABLE OSCILLATORS WITH SIGNIFICANTLY REDUCED PHASE NOISE.
IEEE Trans. Microwave Theory Tech., Vol. 43 (1995), No. 2, p. 278-285.

[28] Yamauchi, Y. et al.,
A 15-GHZ MONOLITHIC LOW NOISE VCO USING ALGAAS/GAAS HBT.
IEEE Journal of Solid-State Circuits, Vol. 27 (1992), No. 10, p. 1444-1447.

[29] Wang, H. and K.W. Chang, D. Smith, G. Dow, S. Kin, L. Tan, A.K. Oki, B. R. Allen,
A W-BAND SOURCE MODULE USING MMIC'S.
IEEE Trans. Microwave Theory Techn., Vol. MTT-43 (1995), No. 5, p. 1010-1015.

[30] Madihian, M. and H. Takahashi,
A LOW-NOISE K-KA BAND OSCILLATOR USING ALGAAS/GAAS HBT.
IEEE Trans. on Microwave Theory Techn., Vol. 39 (1991), No. 1, p. 133-136.

[31] Kim, M.E. et al.,
12-40 GHZ LOW HARMONIC DISTORSION AND PHASE NOISE OF GAAS HETEROJUNCTION BIPOLAR TRANSISTORS.
In: Proc. IEEE GaAs IC Symposium, Nashville TN, 6-9 Nov. 1988.
New York: IEEE, 1988. 10th Annual GaAs IC Symposium technical digest 1988, p. 117-120.

[32] Güttich, U. and J.M. Dieudonné, K. Riepe, A. Marten, H. Leier,
KA BAND MONOLITHIC VCOS FOR LOW NOISE APPLICATIONS USING GAINP/GAAS HBTS.
In: Proc. 1994 IEEE MTT-S International Microwave Symposium, San Diego CA, 23-27 May 1994 (Digest). Ed. by H.J. Kuno and C.P. Wen.
New York: IEEE, 1994. Vol. 1, p. 131-134.

[33] Blanck, H. et al.,
FULLY MONOLITHIC KU AND KA-BAND GAINP/GAAS HBT WIDEBAND VCOS.
In: Proc. 1994 IEEE MTT-S International Microwave Symposium, San Diego CA, 23-27 May 1994 (Digest). Ed. by H.J. Kuno and C.P. Wen.
New York: IEEE, 1994. Vol. 1, p. 127-130.

Appendix A

S-parameters and Smith charts

A.1 Introduction

In this Appendix, S-parameters and Smith charts will be discussed. A definition of the S-parameters will be given and the stability of a two-port is explained. Furthermore, the use of Smith charts is briefly discussed. First, in section A.2 we discuss some results of the transmission line theory to understand the meaning and use of S-parameters. In section A.3 the S-parameters are introduced and defined. Using these parameters, stability of a two-port is explained in section A.4. Finally, Smith charts are discussed in section A.5.

A.2 Transmission line theory

Consider a transmission line connected to a load Z_L and a source with internal impedance Z_{in} as shown in Figure A.1.

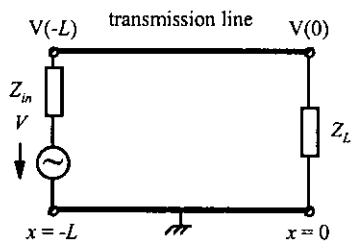

Figure A.1. Transmission line connected to a load.

The source produces an oscillating signal V. Because the voltage is related to the electric field and electromagnetic fields can not propagate with infinite velocity, a time delay exists between the voltage at $x = -L$ and the voltage at $x = 0$. This time delay, τ, can be computed from

$$\tau = \frac{L}{v_g} \tag{A.1}$$

where L is the length of the transmission line and v_g the group velocity of the electromagnetic wave inside the transmission line. If the applied frequency is very low and/or the length of the transmission line is very small, τ is negligible compared to the period of the signal so conventional circuit analysis can be applied. However, if the applied frequency is very high and/or the length of the transmission line is very large, time delay effects must be accounted for. Transmission line theory states that the complex amplitudes of the voltages and currents along a lossless transmission line can be written as

$$v(z) = V_0^+ \exp(-j\beta z) + V_0^- \exp(j\beta z)$$
$$i(z) = \frac{V_0^+ \exp(-j\beta z)}{Z_0} - \frac{V_0^- \exp(j\beta z)}{Z_0} \tag{A.2}$$

where β is the propagation constant and Z_0 the characteristic impedance. Equation (A.2) indicates that both voltage and current along the transmission line can be written as the sum of two waves travelling in opposite directions.

The characteristic impedance is related to the physical properties of the transmission line. The propagation constant equals 2π divided by the wavelength of the oscillating signal, or

$$\beta = \frac{2\pi}{\lambda} = \frac{2\pi f}{v_g} \tag{A.3}$$

where f is the frequency of the applied signal. The group velocity v_g is also determined by the physical properties of the transmission line, mainly the electric permittivity.

The expressions in equation (A.2) contain 2 variables, V_0^+ and V_0^- that depend on the way the transmission line is connected to other components. In Figure A.1, a load Z_L is connected to the right side of the transmission line; this results in the boundary condition at $z = 0$

$$\frac{v(0)}{i(0)} = \frac{V_0^+ + V_0^-}{V_0^+ - V_0^-} \cdot Z_0 = Z_L \tag{A.4}$$

where Z_L is the load impedance. Defining the reflection coefficient Γ_L as the ratio of the amplitudes of the reflected to the incident wave we find at $x = 0$

$$\Gamma_L(0) = \frac{V_0^-}{V_0^+} = \frac{Z_L - Z_0}{Z_L + Z_0} \tag{A.5}$$

The reflection coefficient indicates how much of the incident wave is reflected back into the transmission line. Note that in general the reflection coefficient is position dependent.

The other necessary and sufficient boundary condition at $x = 0$ can be found in a similar way resulting in

$$\frac{v(-L)}{i(-L)} = \frac{V_0^+ \exp(j\beta L) + V_0^- \exp(-j\beta L)}{V_0^+ \exp(j\beta L) - V_0^- \exp(-j\beta L)} Z_0 = Z_{in} \tag{A.6}$$

where Z_{in} is the internal resistance of the source. From equations (A.4) and (A.6) we can compute both V_0^+ and V_0^-.

A.3 S-parameters

Consider the two-port shown in Figure A.2. Most often, two-ports and in general n-ports are characterised using Y, Z or H-parameters. However, these parameters require open or short circuits to evaluate the coefficients. When operating at microwave

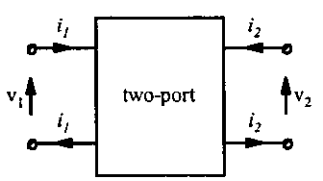

Figure A.2. Current and voltage definitions of a two-port.

frequencies these terminations are very difficult to realise.

The scattering or S-parameters have the advantage that they can be measured using any termination and that they provide us with insight in the power transfer inside the system. These parameters relate waves instead of currents and voltages. The S-parameters can be computed from

$$\begin{bmatrix} b_1 \\ \vdots \\ b_n \end{bmatrix} = \begin{pmatrix} S_{11} & S_{1n} \\ \vdots & \ddots & \vdots \\ S_{n1} & S_{nn} \end{pmatrix} \cdot \begin{bmatrix} a_1 \\ \vdots \\ a_n \end{bmatrix} \tag{A.7}$$

where

$$\begin{aligned} a_i &= \frac{V_i + Z_i I_i}{2\sqrt{\mathrm{Re}|Z_i|}} \\ b_i &= \frac{V_i - Z_i^* I_i}{2\sqrt{\mathrm{Re}|Z_i|}} \end{aligned} \tag{A.8}$$

where Z_i is the (arbitrary) reference impedance. However, most often this reference impedance is chosen equal to the characteristic impedance of the transmission line that feeds the system.

The meaning of a_i and b_i becomes clear when we combine equations (A.2) and (A.8) yielding

$$\begin{aligned} a_i &= \frac{V_i + Z_i I_i}{2\sqrt{\mathrm{Re}|Z_i|}} \\ &= \frac{V_0^+ + V_0^- + Z_0\left(V_0^+/Z_0 - V_0^-/Z_0\right)}{2\sqrt{\mathrm{Re}|Z_0|}} = \frac{V_0^+}{\sqrt{\mathrm{Re}|Z_0|}} \end{aligned} \tag{A.9}$$

$$\begin{aligned} b_i &= \frac{V_i - Z_i^* I_i}{2\sqrt{\mathrm{Re}|Z_i|}} \\ &= \frac{V_0^+ + V_0^- - Z_0^*\left(V_0^+/Z_0 - V_0^-/Z_0\right)}{2\sqrt{\mathrm{Re}|Z_0|}} = \frac{V_0^-}{\sqrt{\mathrm{Re}|Z_0|}} \end{aligned} \tag{A.10}$$

where the reference impedance is chosen as $Z_i = Z_0 = Z_0^*$. Hence, the characteristic impedance is assumed real, as is the case for most transmission lines.

We can see that both a_i and b_i have the unit of square root of power. Furthermore, a_i is determined by the incident wave, the wave travelling towards the n-port, while b_i is determined by the reflected wave, the wave travelling away from the n-port. Because of this, a_i and b_i are often referred to as power waves.

Computation of S_{ii} gives

$$S_{ii} = \frac{b_i}{a_i} = \frac{V_i - Z_i^* I_i}{V_i + Z_i I_i} = \frac{Z_{in} I_i - Z_i I_i}{Z_{in} I_i + Z_i I_i} = \frac{Z_{in} - Z_0}{Z_{in} + Z_0} \tag{A.11}$$

where Z_{in} is the impedance looking into port i.

Comparing with equation (A.5) indicates that S_{ii} can be identified as the reflection coefficient at port i when the n-port is connected to a transmission line with a real characteristic impedance.

To illustrate the power waves inside a device signal flow graphs are often used. An example of an signal flow graph is given in Figure A.3.

A two-port is connected to a load characterised by Γ_L. The factors $S_{11}...S_{22}$, $e^{j\theta}$ represent the way a wave is transformed when moving along the line associated with each

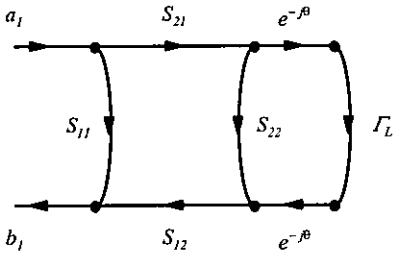

Figure A.3. Signal flow graph of a two-port connected to a load by a transmission line.

factor. The factor $e^{j\theta}$ represents the phase shift introduced by the transmission line. This phase can be computed from

$$\theta = \omega \cdot L \tag{A.12}$$

A.4 Stability of a two-port

An important parameter describing the device in Figure A.3 is the overall input reflection coefficient at port 1. This coefficient and more important the input impedance of the two-port shown in Figure A.3 is important for conjugate matching in order to obtain maximum power transfer.
The reflected wave b1 can be computed from

$$\begin{aligned} b_1 &= S_{11}a_1 + S_{12}S_{21}\Gamma_L a_1 \cdot \left[1 + \Gamma_L S_{22} + \Gamma_L^2 S_{22}^2 + \cdots\right] \\ &= S_{11}a_1 + S_{12}S_{21}\Gamma_L a_1 \cdot \sum_{n=1}^{\infty} \left(\Gamma_L S_{22}\right)^n \\ &= S_{11}a_1 + \frac{S_{12}S_{21}\Gamma_L a_1}{1 - \Gamma_L S_{22}} \end{aligned} \tag{A.13}$$

The incident and reflected waves are then related by

$$S_{11}' = \frac{b_1}{a_1} = S_{11} + \frac{S_{12}S_{21}\Gamma_L}{1 - \Gamma_L S_{22}} \tag{A.14}$$

where S_{11}' is the overall reflection coefficient of the one-port consisting of the two-port, transmission line and load. In this derivation the phase shift introduced by the transmission line is set to zero for sake of simplicity.

When $\Gamma_L S_{22} > 1$ the power inside the loop L explodes leading to an unstable and/or oscillating device. Therefore for stable operation the following condition must apply

$$\Gamma_L S_{22} < 1 \tag{A.15}$$

When we restrict ourselves to passive terminations $|\Gamma_L|$ is always smaller than one, which leads to the requirement $|S_{22}| < 1$. When a device consists of multiple n-ports unconditional stability can only be achieved when the total reflection coefficient is less than zero at every port. Therefore, we express the condition for unconditional stability as the requirement that the magnitude of the total reflection coefficient at all ports of a network is strictly less than one for any combination of passive components. For the two-port of Figure A.3 this requirement results in

$$\left|S_{11}'\right| = \left|\frac{S_{11} + S_{12}S_{21}\Gamma_L}{1 - S_{22}\Gamma_L}\right| < 1 \tag{A.16}$$

A similar equation can be found when we connect a load, characterised by Γ_S, to the other port

$$\left|S_{22}'\right| = \left|\frac{S_{22} + S_{12}S_{21}\Gamma_S}{1 - S_{11}\Gamma_S}\right| < 1 \tag{A.17}$$

This load could for instance represent the internal resistance of a source. The requirements (A.16) and (A.17) can be rewritten as the following necessary and sufficient conditions for unconditional stability for a two-port

$$\begin{aligned} K &< 1 \\ |S_{11}| &< 1 \\ |S_{22}| &< 1 \\ |S_{12}S_{21}| &< 1 - |S_{11}|^2 \\ |S_{12}S_{21}| &< 1 - |S_{22}|^2 \end{aligned} \tag{A.18}$$

where K is given by

$$K = \frac{1 - |S_{11}|^2 - |S_{22}|^2 + |S_{11}S_{22} - S_{12}S_{21}|^2}{2 \cdot |S_{12}S_{21}|} \tag{A.19}$$

A.5 Smith charts

Essentially, a Smith chart is a polar plot of a reflection coefficient. We rewrite equation (A.5)

$$\Gamma = \frac{Z_L - Z_0}{Z_L + Z_0} = \frac{Z_L/Z_0 - 1}{Z_L/Z_0 + 1} = \frac{z_L - 1}{z_L + 1} \tag{A.20}$$

The strength of the Smith charts is that these charts contain circles with which z_L can be found. There are two types of circles present in a Smith chart; Γ circles through (1, 0) that all have their origin on the real axis and Γ circles through (1, 0) that all have their origin on the vertical at Γ = 1. These circles are called constant resistance circles and constant reactance circles, respectively. These circles are given by

$$\begin{aligned} &\text{constant resistance circles:} \quad \left(\Gamma_r - \frac{r_l}{1 + r_l}\right)^2 + \Gamma_i^2 = \left(\frac{1}{1 + r_l}\right)^2 \\ &\text{constant reactance circles:} \quad (\Gamma_r - 1)^2 + \left(\Gamma_i - \frac{1}{x_L}\right)^2 = \left(\frac{1}{x_L}\right)^2 \end{aligned} \tag{A.21}$$

where r_L and z_L are the real and imaginary parts of z_L and Γ_r and Γ_i are the real and imaginary parts of Γ. To determine z_L we just have to read the appropriate values from the constant resistance and constant reactance circles on which the reflection coefficient lies. A picture of the complete Smith chart is shown on the next page.

The Complete Smith Chart

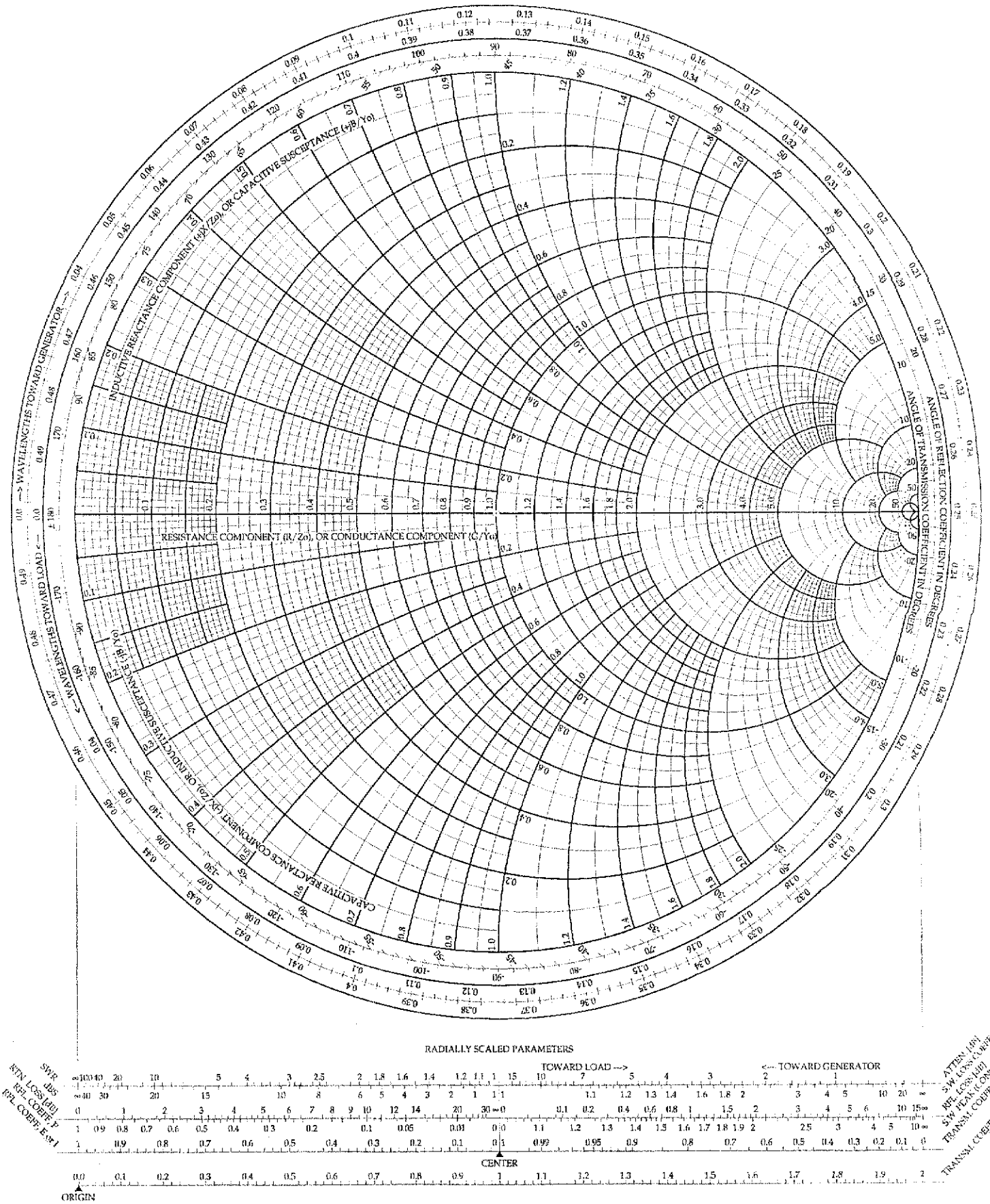

Appendix B

Derivation of the oscillator, stability and noise equations

B.1 Introduction

In this appendix, we will derive expressions for the oscillator equation, stability, amplitude modulation (AM) and frequency modulation (FM) of a negative resistance oscillator [23]. The detailed derivation of the oscillator equation is presented in section B.2. Consequently, in section B.3 the conditions for stable oscillations are derived. Finally, the derivations of the noise spectra are given in section B.4.

B.2 Derivation of the oscillator equation

For the derivation of the oscillator equation we use the schematic diagrams of Figure 4.5. For the sake of convenience, this Figure is represented in Figure B.1.

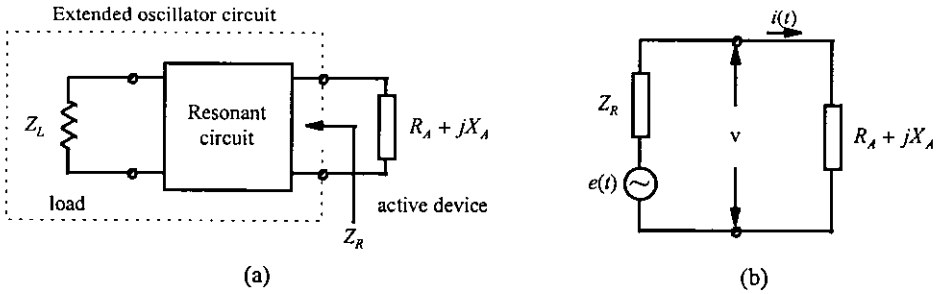

Figure B.1. (a) Negative resistance oscillator schematic diagram.
(b) Equivalent circuit of the negative oscillator.

There are two equations that describe the oscillator. The first equation expresses the HF current flowing through the oscillator as

$$i(t) = \mathrm{Re}\{I(t)\} = A(t)\cdot\cos[\omega t + \phi(t)] \tag{B.1}$$

where

$$I(t) = A(t)\cdot\exp\left(j[\omega t + \phi(t)]\right) \tag{B.2}$$

$A(t)$ and $\phi(t)$ are unknown amplitude and phase variables and are assumed to vary slowly with time compared to the current $i(t)$. $A(t)$ is directly related to the oscillator HF power level. The device impedance is assumed to be a function of $A(t)$ only and the circuit

impedance Z_R is assumed to be a function of the oscillator fundamental frequency ω only. The oscillator equation has solutions of ω at frequencies where oscillations can be sustained. This model would be more complete if higher order harmonics were included in equation (B.1). However, we only desire oscillation conditions for the fundamental frequency. If higher order terms were included, they would be eliminated in an integration step, which will be applied later.

The second equation that describes the oscillator is the voltage loop relation around the circuit in Figure 4.1b

$$v(t) + \mathrm{Re}\{Z_R(\omega) \cdot I(t)\} = e(t) \tag{B.3}$$

Solving equations (B.1) and (B.3) will give expressions for $A(t)$ and $\phi(t)$ in terms of the circuit and device impedances. Applying some simplifications to the expressions will yield the oscillator equation.

We begin the derivation by evaluating the terms in equation (B.3). Ohm's law gives us the voltage drop across the device

$$\begin{aligned} v(t) &= i(t) \cdot (R_A + jX_A) \\ &= R_A A \cdot \cos(\omega t + \phi) - X_A A \cdot \sin(\omega t + \phi) \end{aligned} \tag{B.4}$$

where $R_A < 0$. The magnitude of the part of X_A that is a function of $A(t)$ is assumed to be small compared to R_A; the constant part of the device reactance can be included in $Z_R(\omega)$.

We obtain a first-order approximation for the frequency dependence of the circuit by employing perturbation theory to analyse the voltage drop across $Z_R(\omega)$. The frequency perturbation of $\delta\omega$ to ω can be used to obtain

$$\omega' = \omega + \delta\omega \tag{B.5}$$

An expression for $\delta\omega$ is obtained by examining the derivative of the current

$$\frac{dI(t)}{dt} = j\omega' I(t) = \left[j\left(\omega + \frac{d\phi}{dt}\right) + \frac{1}{A}\frac{dA}{dt} \right] \cdot I(t) \tag{B.6}$$

If we ignore all second and higher order derivatives of $A(t)$ and $\phi(t)$ with respect to t, a first order approximation for the m^{th} derivative is

$$\frac{d^m I(t)}{dt^m} \approx (j\omega')^m \cdot I(t) \tag{B.7}$$

These results are consistent with Laplace transform circuit theory, so that

$$\omega' = \omega + \delta\omega = \omega + \frac{d\phi}{dt} - j\frac{1}{A}\frac{dA}{dt} \tag{B.8}$$

If we assume that $|\delta\omega| << \omega$, then, expanding $Z_R(\omega)$ in a Taylor series around $\omega' = \omega$ gives

$$\begin{aligned} Z_R(\omega') &\approx Z_R(\omega) + \frac{dZ_R(\omega)}{d\omega} \cdot \delta\omega = \\ &= R_R(\omega) + jX_R(\omega) + \left[R_R'(\omega) + jX_R'(\omega) \right] \cdot \left(\frac{d\phi}{dt} - j\frac{1}{A}\frac{dA}{dt} \right) \end{aligned} \tag{B.9}$$

where the primes denote derivatives with respect to ω. Now we can write the perturbed voltage drop across $Z_R(\omega)$ as

$$\begin{aligned} \mathrm{Re}\{Z_R \cdot I(t)\} = &\left[R_R(\omega) + R_R'(\omega)\frac{d\phi}{dt} + X_R'(\omega)\frac{1}{A}\frac{dA}{dt} \right] \cdot A \cdot \cos(\omega t + \phi) \\ &- \left[X_R(\omega) + X_R'(\omega)\frac{d\phi}{dt} - R_R'(\omega)\frac{1}{A}\frac{dA}{dt} \right] \cdot A \cdot \sin(\omega t + \phi) \end{aligned} \tag{B.10}$$

If we substitute equations (B.4) and (B.9) into the loop equation (B.3), we obtain

$$\begin{aligned}&\left[R_R(\omega)+R_A(A)+R_R'(\omega)\frac{d\phi}{dt}+X_R'(\omega)\frac{1}{A}\frac{dA}{dt}\right]\cdot A\cdot\cos(\omega t+\phi)\\&-\left[X_R(\omega)+X_A(A)+X_R'(\omega)\frac{d\phi}{dt}-R_R'(\omega)\frac{1}{A}\frac{dA}{dt}\right]\cdot A\cdot\sin(\omega t+\phi)=e(t)\end{aligned}\tag{B.11}$$

This equation can be multiplied first by $\cos(\omega t+\phi)$ and then $\sin(\omega t+\phi)$ and in each case, integrated over one period of oscillation T_0 to give

$$\begin{aligned}&R_R(\omega)+R_A(A)+R_R'(\omega)\frac{d\phi}{dt}+X_R'(\omega)\frac{1}{A}\frac{dA}{dt}=\frac{1}{A}e_c(t)\\&-X_R(\omega)-X_A(A)-X_R'(\omega)\frac{d\phi}{dt}+R_R'(\omega)\frac{1}{A}\frac{dA}{dt}=\frac{1}{A}e_s(t)\end{aligned}\tag{B.12}$$

where

$$\begin{aligned}e_c(t)&=\frac{2}{T_0}\int_{t-T_0}^{t}e(t)\cdot\cos(\omega t+\phi)\,dt\\e_s(t)&=\frac{2}{T_0}\int_{t-T_0}^{t}e(t)\cdot\sin(\omega t+\phi)\,dt\end{aligned}\tag{B.13}$$

These equations can be manipulated readily into two equations, one containing only dA/dt and one with only $d\phi/dt$

$$\begin{aligned}&\left[R_R(\omega)+R_A(A)\right]\cdot X_c'(\omega)-\left[X_R(\omega)+X_A(A)\right]\cdot R_R'(\omega)\\&\qquad+\left|Z_R'(\omega)\right|^2\frac{1}{A}\frac{dA}{dt}=\frac{1}{A}\left[X_R'(\omega)\cdot e_c(t)+R_R'(\omega)\cdot e_s(t)\right]\end{aligned}\tag{B.14}$$

$$\begin{aligned}&\left[R_R(\omega)+R_A(A)\right]\cdot R_c'(\omega)+\left[X_R(\omega)+X_A(A)\right]\cdot X_R'(\omega)\\&\qquad+\left|Z_R'(\omega)\right|^2\frac{d\phi}{dt}=\frac{1}{A}\left[R_R'(\omega)\cdot e_c(t)+X_R'(\omega)\cdot e_s(t)\right]\end{aligned}\tag{B.15}$$

Equations (B.14) and (B.15) are general oscillation conditions that determine the fundamental harmonic oscillating current's amplitude and phase. The oscillator equation is a special case of these equations obtained under steady-state, free-running conditions. For this case $e(t)=0$, $dA/dt=0$ and $d\phi/dt=0$ and we obtain the final result, the oscillator equation

$$\begin{aligned}&R_R(\omega)+R_A(A)+j\left[X_R(\omega)+X_A(A)\right]=0\\&\qquad\Rightarrow\quad Z_R+Z_A=0\end{aligned}\tag{B.16}$$

The oscillation conditions have been derived in terms of the device and circuit impedances. The oscillation criteria can also be presented in terms of reflection coefficients. This can be done by rewriting (B.16) using the relation

$$Z=Z_0\cdot\frac{1+\Gamma}{1-\Gamma}\tag{B.17}$$

where Z_0 is the characteristic impedance of the oscillator system and Γ the reflection coefficient of the impedance Z. Combining (B.16) and (B.17) results in

$$\frac{1+\Gamma_R}{1-\Gamma_R}+\frac{1+\Gamma_A}{1-\Gamma_A}=0 \quad \Rightarrow \quad \Gamma_R\cdot\Gamma_A=1 \tag{B.18}$$

If the resonant circuit is passive then Γ_R will be between 0 and 1 in magnitude. Thus, in order to have oscillation, Γ_A will require a magnitude that is greater than 1.

B.3 Derivation of the stability condition

We can derive the stability condition by perturbing the oscillation amplitude by a small amount $\delta A(t)$ from the steady-state value A_0. Stable oscillations are generated if $d(\delta A)/dt < 0$ which implies that the perturbed oscillator returns to the steady-state operating point. If we consider the oscillator equation of a perturbed oscillator we can write

$$\begin{aligned} R_R(\omega_0)+R_A(A)&=\frac{\delta A}{A_0}A_0\frac{\partial R_A}{\partial A}\\ X_R(\omega_0)+X_A(A)&=\frac{\delta A}{A_0}A_0\frac{\partial X_A}{\partial A}\end{aligned} \tag{B.19}$$

When we substitute these equations into (B.14) and assume that $e(t) = 0$, we obtain

$$\delta A\frac{\partial R_A}{\partial A}X_R'(\omega_0)-\delta A\frac{\partial X_A}{\partial A}R_R'(\omega_0)+\left|Z_R'(\omega_0)\right|^2\frac{1}{A_0}\frac{d(\delta A)}{dt}=0 \tag{B.20}$$

Stability results if $\delta A(t)$ is a decreasing function of time, or

$$S=\frac{\partial R_A}{\partial A}X_R'(\omega_0)-\frac{\partial X_A}{\partial A}R_R'(\omega_0)>0 \tag{B.21}$$

So the perturbation $\delta A(t)$ will decrease to zero if $S > 0$ and steady-state oscillations will be stable. Equation (B.21) can be rewritten as

$$S=R_R'(\omega_0)\frac{\partial R_A}{\partial A}\left[\frac{X_R'(\omega_0)}{R_R'(\omega_0)}-\frac{\partial X_A/\partial A}{\partial R_A/\partial A}\right] \tag{B.22}$$

If we define

$$\begin{aligned}\tan\theta_R&=\frac{X_R'(\omega_0)}{R_R'(\omega_0)}\\ \tan\theta_A&=\frac{\partial X_A/\partial A}{\partial R_A/\partial A}\end{aligned} \tag{B.23}$$

S becomes

$$S=R_R'(\omega_0)\frac{\partial R_A}{\partial A}\left[\tan\theta_R-\tan\theta_A\right] \tag{B.24}$$

The stability condition demonstrates that the stability of an oscillator depends on the electrical characteristics of both its circuit and device. This stability condition is approximate because we assumed that the device impedance was a function of the fundamental HF current amplitude only.

As with the oscillation conditions we can rewrite (B.24) in terms of reflection coefficients. The reflection coefficients Γ_R and Γ_A can be defined as

$$\begin{aligned}\Gamma_R(\omega)&=\gamma_R(\omega)\cdot\exp\left(j\psi_R(\omega)\right)\\ \Gamma_A(\omega)&=\gamma_A(\omega)\cdot\exp\left(j\psi_A(A)\right)\end{aligned} \tag{B.25}$$

where γ_R and γ_A are the magnitude of the reflection coefficients. If a microwave oscillator is operating in steady state under stable conditions, its reflection coefficients must satisfy the stability condition

$$S = \gamma_R \frac{d\gamma_A}{dA} \cdot \frac{d\psi_R}{d\omega} - \gamma_A \frac{d\psi_A}{dA} \cdot \frac{d\gamma_R}{d\omega} > 0 \tag{B.26}$$

Employing cylindrical co-ordinates, the stability condition can be rewritten as

$$S = \left|\frac{d\Gamma_R}{d\omega}\right| \cdot \left|\frac{d\Gamma_A^{-1}}{dA}\right| \cdot \sin\theta > 0 \tag{B.27}$$

With S in this form, an oscillator is clearly stable when the angle θ is between 0° and 180°.

B.4 Derivation of the AM and FM equations

In this section, we derive expressions for the amplitude modulation (AM) and the frequency modulation (FM) or phase noise of an oscillator. In the schematic model of an oscillator shown in Figure B.1b, the function $e(t)$ can be used to represent a noise voltage; $e(t)$ contains a large number of delta function pulses in the form

$$e(t) = \sum_{n=0}^{m} \varepsilon_n \cdot \delta(t - t_n) \tag{B.28}$$

where the pulses occur at time t_n with amplitude ε_n. The amplitude and time of occurrence of each pulse is independent and random. The delta function is defined according to

$$\int_{-\infty}^{\infty} \delta(x - x') \cdot y(x)\, dx = y(x') \tag{B.29}$$

with $\delta(x - x') = 0$ when $x \neq x'$.

Because noise is a random process, noise analysis deals with average values of quantities. As such, we will review some definitions of generalised function theory that will be needed in our noise analysis. First, postulate the function $g(t)$ defined on the interval $t \in [-T, T]$, but equal to zero for all $t \geq T$.

- The *autocorrelation function* of $g(t)$ is

$$R_g(\tau) = \lim_{t\to\infty} \frac{1}{2T} \int_{-\infty}^{\infty} g(t) g(t+\tau)\, dt \tag{B.30}$$

- The *power spectral density* of $g(t)$ is

$$|g(\omega)|^2 = \int_{-\infty}^{\infty} R_g(\tau) \cdot e^{-j\omega\tau}\, d\tau \tag{B.31}$$

where t and ω are variables which can assume arbitrary meanings; they represent time and circular frequency for our purposes. The power spectral density, a measure of power versus frequency of a signal, is displayed by spectrum analysers. We seek expressions for the power spectral density of the HF current amplitude A and phase ϕ as functions of the noise voltage $e(t)$.

We begin by finding the spectral density of the noise voltage. Equation (B.30) gives the autocorrelation of $e(t)$

$$R_e(\tau) = m\langle \varepsilon^2 \rangle \cdot \delta(\tau) \tag{B.32}$$

where m is the average number of pulses in a unit of time and $\langle \varepsilon^2 \rangle$ is the average of the square of the pulse strength for all the noise pulses. If we substitute this result into equation (B.31), we obtain the spectral density of $e(t)$

$$|e(\omega)|^2 = \int_{-\infty}^{\infty} m\langle \varepsilon^2 \rangle \cdot \delta(\tau) e^{-j\omega\tau}\, d\tau = m\langle \varepsilon^2 \rangle = |e|^2 \tag{B.33}$$

where $|e(\omega)|^2$ is the spectral density of white noise. White noise is constant in the power level over frequency. Because of this characteristic, white noise makes an ideal test signal for analysing the noise behaviour of a circuit.

The general oscillation conditions (B.14) and (B.15) will give us the noise expressions we desire. This requires us to evaluate the integrals of (B.13) first. We can write them as

$$n_c(t) = \frac{1}{T_0} \int_{t-T_0}^{t} \sum_{n=0}^{m} \varepsilon_n \delta(t - t_n) \cdot \cos(\omega t + \phi)\, dt \tag{B.34}$$

$$n_s(t) = \frac{1}{T_0} \int_{t-T_0}^{t} \sum_{n=0}^{m} \varepsilon_n \delta(t - t_n) \cdot \sin(\omega t + \phi)\, dt \tag{B.35}$$

For a single noise pulse, $\varepsilon_0 \delta(t - t_0)$, we have

$$e_c(t) = \frac{2 \cdot \varepsilon_0}{T_0} \cos(\omega t_0 + \phi) \tag{B.36}$$

Because we have assumed that the current magnitude A is a slowly varying function of time and the noise fluctuations are comparatively rapid, the period T_0 of average noise fluctuation is short. Thus, we can consider $e_c(t)$ as a δ-function also with magnitude $2\varepsilon \cos(\omega t_0 + \phi)$. It occurs in time half way between $t = t_0$ and $t = t_0 + T_0$, at $t = t_0 + T_0/2$, but we will use $t = t_0$ for simplicity.

Superposition applies so that the contribution of each noise pulse to the integrals (B.34) and (B.35) can be obtained as we have done for the single pulse and the results summed together. When we take the autocorrelation of $n_c(t)$ and $n_s(t)$, we get the following equation

$$n_c(\tau) = n_s(\tau) = 2m\langle \varepsilon^2 \rangle \delta(\tau) \tag{B.37}$$

Comparing this result with the autocorrelation of $e(t)$ in equation (B.32) leads to

$$|n_c(\tau)|^2 = |n_s(\tau)|^2 = 2|e|^2 \tag{B.38}$$

As in the stability analysis of section B.3, we let A deviate from its steady-state value A_0 by $\delta A(t)$. The deviation in the sum of the device impedance and oscillator circuit impedance can be written again as

$$R_R(\omega_0) + R_A(A) = \frac{\delta A}{A_0} A_0 \frac{\partial R_A}{\partial A} \tag{B.39}$$

for the resistance, and

$$X_R(\omega_0) + X_A(A) = \frac{\delta A}{A_0} A_0 \frac{\partial X_A}{\partial A} \tag{B.40}$$

for the reactance. If we substitute these equations into the general oscillation equations (B.14) and (B.15), we obtain

$$A_0 \frac{\partial R_A}{\partial A} X_R'(\omega_0)\delta A - A_0 \frac{\partial X_A}{\partial A} R'(\omega_0)\delta A + \left|Z_R'(\omega_0)\right|^2 \frac{d(\delta A)}{dt} = X_R'(\omega_0)\cdot n_c(t) + R_R'(\omega_0)\cdot n_s(t) \tag{B.41}$$

$$A_0 \frac{\partial R_A}{\partial A} R_R'(\omega_0)\delta A - A_0 \frac{\partial X_A}{\partial A} X'(\omega_0)\delta A + \left|Z_R'(\omega_0)\right|^2 \frac{d\phi}{dt} = R_R'(\omega_0)\cdot n_c(t) - X_R'(\omega_0)\cdot n_s(t) \tag{B.42}$$

When we evaluate the autocorrelation and power spectral density of each term of equation (B.41) and solve for $\left|\delta A(\omega)\right|^2$, we arrive at the result

$$\left|\delta A(\omega_m)\right|^2 = \frac{2\cdot\left|Z_R'(\omega_0)\right|^2\cdot|e|^2}{\omega_m^2\left|Z_R'(\omega_0)\right|^4 + A_0^2 S^2} \tag{B.43}$$

Similarly, the power spectral density of ϕ can be obtained

$$\left|\phi(\omega_m)\right|^2 = \frac{2\cdot|e|^2}{\omega_m^2 A_0^2}\,\frac{\omega_m^2\left|Z_R'(\omega_0)\right|^2 + A_0^2\left[\left(\frac{\partial R_A}{\partial A}\right)^2 + \left(\frac{\partial X_A}{\partial A}\right)^2\right]}{\omega_m^2\left|Z_R'(\omega_0)\right|^4 + A_0^2 S^2} \tag{B.44}$$

Appendix C

Optimising the total oscillator circuit

In this appendix, we present the simulation results of the total oscillator's optimisation step. Table A.1 shows the buffer configuration and the oscillator performance as function of the gate width of the HEMT applied in the basic oscillator.

Table C.1 Simulation results of the total oscillator configurations.

Gate width [μm]	Buffer configuration[1]	Phase noise at f_m = 1 kHz [dBc/Hz]	Output power [dBm]	Distortion [%]
50	5th - HEMT - ×	-102.5	9.8	16.44
	5th - HEMT - 5th	-64.6	3.0	0.12
	× - HEMT - 5th	-89.9	8.9	0.91
	3rd - HEMT - 3rd	-76.9	9.3	1.56
	3rd - HEMT - 5th	-77.5	7.5	0.54
100	5th - HEMT - ×	-89.5	10.7	20.33
	5th - HEMT - 5th	-80.9	7.4	0.60
	× - HEMT - 5th	-69.2	9.0	0.96
	3rd - HEMT - 3rd	-85.9	9.6	1.74
	3rd - HEMT - 5th	-82.6	7.5	0.55
150	5th - HEMT - ×	-84.7	12.7	29.35
	5th - HEMT - 5th	-81.7	8.7	0.85
	× - HEMT - 5th	-72.4	9.7	0.28
	3rd - HEMT - 3rd	-81.2	10.8	2.47
	3rd - HEMT - 5th	-79.6	8.8	0.82
200	5th - HEMT - ×	-93.3	11.2	22.6
	5th - HEMT - 5th	-85.7	7.2	0.54
	× - HEMT - 5th	-74.1	10.4	1.12
	3rd - HEMT - 3rd	-77.8	10.4	2.15
	3rd - HEMT - 5th	-74.6	8.7	0.72

[1] Notation: × ≡ no filter; 3rd ≡ third order LP filter; 5th ≡ fifth order LP filter; HEMT ≡ InP based HEMT with a 200 μm gate width. The sequence of the abbreviations agree with the sequence of the applied devices.

Eindhoven University of Technology Research Reports ISSN 0929-8533
(ISSN 0167-9708)

Faculty of Electrical Engineering

(281) Di, Chennian and Jochen A.G. Jess
ON THE DEVELOPMENT OF A FAST AND ACCURATE BRIDGING FAULT SIMULATOR.
EUT Report 94-E-281. 1994. ISBN 90-6144-281-8

(282) Falkus, H.M. and A.A.H. Damen
MULTIVARIABLE H-INFINITY CONTROL DESIGN TOOLBOX: User manual.
EUT Report 94-E-282. 1994. ISBN 90-6144-282-6

(283) Meng, X.Z. and J.G.J. Sloot
THERMAL BUCKLING BEHAVIOUR OF FUSE WIRES.
EUT Report 94-E-283. 1994. ISBN 90-6144-283-4

(284) Rangelrooij, A. van and J.P.M. Voeten
CCSTOOL2: An expansion, minimization, and verification tool for finite state CCS descriptions.
EUT Report 94-E-284. 1994. ISBN 90-6144-284-2

(285) Roer, Th.G. van de
MODELING OF DOUBLE BARRIER RESONANT TUNNELING DIODES: D.C. and noise model.
EUT Report 95-E-285. 1995. ISBN 90-6144-285-0

(286) Dolmans, G.
ELECTROMAGNETIC FIELDS INSIDE A LARGE ROOM WITH PERFECTLY CONDUCTING WALLS.
EUT Report 95-E-286. 1995. ISBN 90-6144-286-9

(287) Liao, Boshu and P. Massee
RELIABILITY ANALYSIS OF AUXILIARY ELECTRICAL SYSTEMS AND GENERATING UNITS.
EUT Report 95-E-287. 1995. ISBN 90-6144-287-7

(288) Weiland, Siep and Anton A. Stoorvogel
OPTIMAL HANKEL NORM IDENTIFICATION OF DYNAMICAL SYSTEMS.
EUT Report 95-E-288. 1995. ISBN 90-6144-288-5

(289) Konieczny, Pawel A. and Lech Józwiak
MINIMAL INPUT SUPPORT PROBLEM AND ALGORITHMS TO SOLVE IT.
EUT Report 95-E-289. 1995. ISBN 90-6144-289-3

(290) Voeten, J.P.M.
POOSL: An object-oriented specification language for the analysis and design of hardware/software systems.
EUT Report 95-E-290. 1995. ISBN 90-6144-290-7

(291) Smeets, B.H.T. and M.H.J. Bollen
STOCHASTIC MODELLING OF PROTECTION SYSTEMS: Comparison of four mathematical techniques.
EUT Report 95-E-291. 1995. ISBN 90-6144-291-5

(292) Voeten, J.P.M. and A. van Rangelrooij
CCS AND TIME: A practical and comprehensible approach to a performance evaluation of finite state CCS descriptions.
EUT Report 95-E-292. 1995. ISBN 90-6144-292-3

(293) Voeten, J.P.M.
SEMANTICS OF POOSL: An object-oriented specification language for the analysis and design of hardware/software systems.
EUT Report 95-E-293. 1995. ISBN 90-6144-293-1

(294) Osch, A.W.H. van
MODELLING OF PRASEODYMIUM-DOPED FLUORIDE AND SULFIDE FIBRE AMPLIFIERS FOR THE 1.3 μM WAVELENGTH REGION.
EUT Report 95-E-294. 1995. ISBN 90-6144-294-X

(295) Bastiaans, Martin J.
GABOR'S EXPANSION AND THE ZAK TRANSFORM FOR CONTINUOUS-TIME AND DISCRETE-TIME SIGNALS: Critical sampling and rational oversampling.
EUT Report 95-E-295. 1995. ISBN 90-6144-295-8

(296) Blaschke, F. and A.J.A. Vandenput
REGELTECHNIEKEN VOOR DRAAIVELDMACHINES. (Control of AC machines, in Dutch)
2 Volumes. Vol. 1: TEKST (Text). Vol. 2: FIGUREN (Figures).
EUT Report 96-E-296. 1996. ISBN 90-6144-296-6

(297) Dolmans, G.
DIVERSITY SYSTEMS FOR MOBILE COMMUNICATION IN A LARGE ROOM.
EUT Report 96-E-297. 1996. ISBN 90-6144-297-4

(298) Mazák, J. and J.L.F. Balseiro
MODELING OF A FLUIDIZED BED REACTOR FOR ETHYLENE POLYMERIZATION.
EUT Report 96-E-298. 1996. ISBN 90-6144-298-2

(299) Butterweck, H.J.
ITERATIVE ANALYSIS OF THE STEADY-STATE WEIGHT FLUCTUATIONS IN LMS-TYPE ADAPTIVE FILTERS.
EUT Report 96-E-299. 1996. ISBN 90-6144-299-0

Eindhoven University of Technology Research Reports ISSN 0929-8533
(ISSN 0167-9708)

Faculty of Electrical Engineering

(300) Horck, F.B.M. van and A.P.J. van Deursen, P.C.T. van der Laan
COUPLING ON A MULTILAYER PRINTED CIRCUIT BOARD AND THE CURRENT DISTRIBUTION IN THE GROUND PLANE.
EUT Report 96-E-300. 1996. ISBN 90-6144-300-8

(301) Veen, J.L.F. van der and L.J.J. Offringa
ROTOR LOSSES IN A HIGH SPEED SYNCHRONOUS GENERATOR WITH PERMANENT MAGNET EXCITATION AND RECTIFIER LOAD.
EUT Report 96-E-301. 1996. ISBN 90-6144-301-6

(302) Zhou, L.M. and E.M. van Veldhuizen
MEDIUM-SCALE EXPERIMENTS ON DeNO/DeSO2 FROM FLUE GAS BY PULSED CORONA DISCHARGE.
EUT Report 96-E-302. 1996. ISBN 90-6144-302-4

(303) Duarte, J.L.
SAMPLED-DATA MODELLING AND SIMULATION OF CYCLICALLY SWITCHED CONVERTERS.
EUT Report 96-E-303. 1996. ISBN 90-6144-303-2

(304) Wouters, P.A.A.F. and J.M. Wetzer
HIGH-VOLTAGE ASPECTS OF THE FREE ELECTRON MASER.
EUT Report 97-E-304. 1997. ISBN 90-6144-304-0

(305) Horck, F.B.M. van and A.P.J. van Deursen
PREDICTION OF COMMON-MODE CURRENTS ON CABLES CONNECTED TO A MULTILAYER PRINTED CIRCUIT BOARD AND COUPLINGS ON THE BOARD.
EUT Report 97-E-305. 1997. ISBN 90-6144-305-9

(306) Leyra Fontaíña, L.
RELATIONS BETWEEN MOMENTS IN THE TIME AND TRANSFORM DOMAIN.
EUT Report 97-E-306. 1997. ISBN 90-6144-306-7

(307) Lago Fernández, J.M.
SUBBAND CODER IMPLEMENTING THE SLIDING-WINDOW KAUTZ TRANSFORMATION.
EUT Report 97-E-307. 1997. ISBN 90-6144-307-5

(308) Kleinpenning, T.G.M.
RELATION BETWEEN 1/F NOISE AND FREQUENCY INDEPENDENT LOSS TANGENT.
EUT Report 98-E-308. 1998. ISBN 90-6144-308-3

(309) Madani, S.M.
A NEW GRAPH-THEORETICAL SCHEME FOR COORDINATION OF PROTECTION SYSTEMS: DETERMINATION OF BREAK POINT SET.
EUT Report 98-E-309. 1998. ISBN 90-6144-309-1

(310) Meer, J.M.C.P. van and W. De Raedt, L.M.F. Kaufmann
DESIGN, FABRICATION AND CHARACTERISATION OF A 20 GHZ LOW PHASE NOISE OSCILLATOR.
EUT Report 98-E-310. 1998. ISBN 90-6144-310-5